8-2011

Computational analysis of the dynamic forces in drive train components of an offshore wind turbines

Artem Korobenko
Clemson University, artem.korobenko@gmail.com

COMPUTATIONAL ANALYSIS OF THE DYNAMIC FORCES IN DRIVE TRAIN COMPONENTS OF AN OFFSHORE WIND TURBINES

A Thesis
Presented to
the Graduate School of
Clemson University

In Partial Fulfillment
of the Requirements for the Degree
Master of Science
Mechanical Engineering

---

by
Artem Korobenko
August 2011

Accepted by:
Dr. David Zumbrunnen, Committee Chair
Mr. Robert Leitner, Co-adviser
Dr. John Wagner
Dr. Firat Testik

ABSTRACT

Wind has good potential for contributing to the national energy supply. Offshore sites and deep sea locations can be especially attractive as the wind turbine market grows. In such places larger wind resources are available with reduced turbulence intensity and wind shear. In addition, visual impact along with noise aspects are reduced. Offshore siting requires greater attention to structural stability and endurance. Forces on drive train components, such as the bearing system, are not well understood.

This work presents the development a model that calculates dynamical forces in drive train components of off-shore wind turbines. The model of a 5MW off-shore wind turbine was developed based on site conditions for the nearby South Carolina coast. The model accounts for elastic deformation of the tower and distributed loads due to gravity, wind, and waves on the wind turbine elements and tower. A finite element computational model was implemented with external forces estimated from analytical models. The main elements of the turbine were based on actual 5MW wind turbine specifications. The tower was represented as a hollow, tapered steel cylinder with a foundation fixed rigidly to the sea floor. A mono-pile supporting structure was specifically represented, due to its applicability to the relatively shallow coastal waters of South Carolina.

The results from time-domain analysis were shown to agree with results generated from other studies. The dynamic response of mean values of loads on drive train components were found to be very similar to those for land-based wind turbines. It was also concluded that magnitude of axial force R_{bx} in the drive train components depend mostly on thrust force produced on the rotor by the three turbine blades. Its maximum value is determined by peak in thrust force and its periodicity is a result of changing thrust force, when blades rotate. To show the influence of thrust force and ocean wave force on force R_{bx}, results were presented also in

frequency domain. It was shown that force R_{bx} has the dominant frequency of 0.2 Hz, which is the frequency of the thrust force. Additionally, eigenfrequency analysis was performed to show the lowest natural frequency of the system. It was found to be 1Hz, which corresponds to the fore-aft oscillation of the tower. This value is higher than frequencies of externally applied force that may guarantee that resonance will not occur in the system. Unlike axial forces, vertical forces in drive train components R_{bz} only determined by weight of components and any change in wind speed, ocean wave height and ocean wave period do not affect the tower deflection in vertical direction.

ACKNOWLEDGEMENTS

I would like to gratefully acknowledge support from the Fulbright Program for making it possible to do a graduate study in the United States and particularly at Clemson University. I am also very grateful for the guidance, support and understanding of Dr. Zumbrunnen, Mr. Leitner from South Carolina Institute of Energy Studies, Dr. Wagner and Dr. Firat Testik during this project. I would especially like to acknowledge my advisor, Dr. Zumbrunnen and my co-adviser, Mr. Leitner for their knowledge and wisdom, and their willingness to help. They were an invaluable resource to me during this project.

The work presented here would not have been possible without the love and support of my family. I am grateful to my fiancée Elina Karimullina for her love and encouragement during this project.

TABLE OF CONTENTS

Page

TITLE PAGE i
ABSTRACT ii
ACKNOWLEDGEMENTS iv
LIST OF TABLES vii
LIST OF FIGURES viii
NOMENCLATURE xiii

Chapter

1. INTRODUCTION 1

Overview of wind turbine history 1
Rationale 3
Literature review 6
Aerodynamics of wind turbine and wind modeling 6
Rotor and drive train design 13
Ocean wave modeling 16
Support structures 19
Related works 21
Objective 23

2. ENGINEERING MODEL 24

Model description and assumptions 24
Modeling of wind turbine components 28
Wind turbine site selection 28
Blade characteristic 35
Hub, nacelle and main bearing configuration 39
Tower design 41
Applied loads 42
Computational method 50
Verification of time step size and mesh size 53
Validation of simulation tool 58
Validation of calculated forces 61

3. RESULTS AND DISCUSSION 63

4. CONCLUSIONS AND RECOMMENDATIONS 91

Conclusions 91
Recommendations 92

APPENDIX 94
REFERENCES 99

LIST OF TABLES

Table Page

1.1 Loads on the off-shore wind turbine 4

2.1 Properties chosen for the modeled offshore wind turbine 26

2.2 Assumptions invoked in model development 26

2.3 Characteristics of wind turbine blade elements 35

2.3 Characteristics of wind turbine blade elements (continued) 36

2.4 A position of main bearing and material properties of bed plate 40

2.5 Mechanical steel properties of the tower 42

2.6 Different meshes used in assessing sensitivity of R_{bx} and R_{bz}, to mesh size 55

2.7 Force balance in the main bearing between externally applied thrust force F_N and reaction force in axial direction R_{bx} 61

3.1 Investigating parameters of the wind and ocean 63

3.1 Investigating parameters of the wind and ocean (continued) 63

3.2 Maximum and mean value of reaction force in main bearing in axial direction calculated from Krogh (2004) study and from current work 81

LIST OF FIGURES

Figure Page

1.1 Growth in size and power production of wind turbines (EWEA, 2009).....2

1.2 Off-shore wind turbine with main structural components 3

1.3 Principal nacelle components of a wind turbine 5

1.4 Airfoil cross-section of blade element with velocities and forces acting on it (Emrah and Nadir, 2009).....8

1.5 Shaft torque measured and calculated by different techniques (Lindenburg, 2004).....10

1.6 Wind speed profile above a surface (Eecen, 2003).....12

1.7 Power coefficient for different rotor designs (Hau, 2006).....14

1.8 Motion of water particle described by linear wave theory.....17

1.9 System of small-amplitude waves 18

1.10 Support structure design for different water depths (Jonkman, 2007.....20

2.1 Rotational speed of the rotor versus wind speed at hub height (Jonkman, 2007).....25

2.2 South Carolina wind speed at 50 m elevation above the ground (Jeffery et al., 2006).....28

2.3 South Carolina bathymetries in meters (Jeffery et al., 2006) 29

2.4 South Carolina distance to the shoreline (Jeffery et al., 2006) 30

2.5 South Carolina distance to major motorways (Jeffery et al., 2006).....30

2.6 Suitable area for placing offshore wind farm (Jeffery et al., 2006 31

2.7 Wind speed time history at 10 m height above the surface (National Data Buoy Center Platform 41004).....32

2.8 Ocean wave height time histories (National Data Buoy Center Platform 41004) 33

2.9 Ocean wave period time histories (National Data Buoy Center Platform 41004).....34

2.10 Corrected lift and drag coefficients of DU21 airfoil 36

2.11 Corrected lift and drag coefficients of DU25 airfoil 37

List of Figures (Continued)

Figure Page

2.12 Corrected lift and drag coefficients of DU30 airfoil 37

2.13 Corrected lift and drag coefficients of DU35 airfoil 38

2.14 Corrected lift and drag coefficients of DU40 airfoil 38

2.15 Corrected lift and drag coefficients of NACA64 airfoil 39

2.16 Loads on wind turbine 43

2.17 Free-body diagram of wind turbine 44

2.18 Computational domain and force boundary conditions 50

2.19 Mesh for wind turbine physical model 52

2.20 Force in main bearing base, R_{bx}, under operational conditions of U=12 m/s, Hs=1 m, Ts=5 s, for different meshes 54

2.21 Force in main bearing base R_{bz} under operational conditions of U=12 m/s, Hs=1 m, Ts=5 s, for different meshes 55

2.22 Force in main bearing base, R_{bx}, under operational conditions of U=12 m/s, Hs=1 m, Ts=5 s, for different time step sizes 56

2.23 Force in main bearing base, R_{bz}, under operational conditions of U=12 m/s, Hs=1 m, Ts=5 s, for different time step sizes 57

2.24 Return map for last 10 cycles of the force in main bearing base, R_{bx}, under operational conditions of U=12 m/s, Hs=1 m, Ts=5 s with normal mesh and time step size of 0.1 s 58

2.25 Rotor power as a function of wind speed calculated by MATLAB simulation tool and in the NREL project 59

2.26 Rotor torque as a function of wind speed calculated by MATLAB simulation tool and in the NREL project 60

2.27 Rotor thrust as a function of wind speed calculated by MATLAB simulation tool and in the NREL project 60

List of Figures (Continued)

Figure Page

3.1 Thrust force, F_N, for wind speed of U=7 m/s in time domain 64

3.2 Thrust force, F_N, for wind speed of U=7 m/s in frequency domain with f_s = 10 Hz.....65

3.3 Ocean wave force, F_M, for H_s = 1 m and T_s = 5 s, in time domain 66

3.4 Ocean wave force, F_M, for H_s = 1 m and T_s = 5 s, in frequency domain 66

3.5 Force in the main bearing base, R_{bx} in axial direction, under operational conditions of U=7 m/s, H_s = 1 m, T_s= 5 s, in time domain 67

3.6 Force in the main bearing base, R_{bx} in axial direction, under operational conditions of U=7 m/s, H_s = 1 m, T_s= 5 s in time domain 68

3.7 Force in the main bearing base, R_{bx} in axial direction, under operational conditions of U=7 m/s, H_s = 1 m, T_s= 5 s in frequency domain 69

3.8 Return map for last 10 cycles of the force in main bearing base, R_{bx}, under operational conditions of U= 7 m/s, Hs=1 m, Ts=5 s.....70

3.9 Force in main bearing base R_{bz} , under operational conditions of U=7 m/s, Hs=1 m, Ts=5 s 71

3.10 Force due to tower deflection in vertical direction under operational conditions of U=7 m/s, H_s = 1 m, T_s= 5 s in time domain 72

3.11 Force due to tower deflection in vertical direction under operational conditions of U=7 m/s, H_s = 1 m, T_s= 5 s in frequency domain 73

3.12 Thrust force, F_N, for wind speed of U=4 m/s in time domain 74

3.13 Thrust force, F_N, for wind speed of U=12 m/s in time domain 74

3.14 Thrust force, F_N, for different wind speed, in frequency domain domain.....75

3.15 Force in the main bearing base, R_{bx} in axial direction, under operational conditions of U=4 m/s, H_s = 1 m, T_s= 5 s in frequency domain 76

3.16 Force in the main bearing base, R_{bx} in axial direction, under operational conditions of U=12 m/s, H_s = 1 m, T_s= 5 s in frequency domain 76

List of Figures (Continued)

Figure Page

3.17 Non dimensional maximum force N_{bx} in the main bearing in axial direction for operational conditions of H_s = 1 m, T_s= 5 s.....78

3.18 Non dimensional maximum force N_{bx} in the main bearing in axial direction for operational conditions of Hs = 1 m and Ts = 5 s.....78

3.19 Non dimensional force amplitude A_{bx} in the main bearing in axial direction for operational conditions of Hs = 1 m and Ts = 5 s.....79

3.20 Non dimensional force amplitude A_{bx} in the main bearing in axial direction for operational conditions of H_s = 1 m, T_s= 5 s.....79

3.21 Force in the main bearing base, R_{bz} in vertical direction, under operational conditions of U= 4 m/s, H_s = 1 m, T_s= 5 s in frequency domain 80

3.22 Force in the main bearing base, R_{bz} in vertical direction, under operational conditions of U=12 m/s, H_s = 1 m, T_s= 5 s in frequency domain. 81

3.23 Ocean wave force, F_M, for H_s = 5 m and T_s = 5 s, in time domain.....82

3.24 Ocean wave force, F_M, for H_s = 5 m and T_s = 5 s, in frequency domain. 83

3.25 Force in the main bearing base R_{bx} for ocean wave heights of Hs= 0 m, Hs = 1 m and H_s = 5 m with U = 7 m/s, T_s =5 s.....84

3.26 Force in the main bearing base R_{bx} for ocean wave heights of H_s= 0 m, H_s = 1 m and H_s = 5 m with U = 7 m/s, T_s =5 s.....84

3.27 Force in the main bearing base, R_{bx} in axial direction, under operational conditions of U=7 m/s, H_s = 0 m, T_s= 5 s in frequency domain 85

3.28 Force in the main bearing base, R_{bx} in axial direction, under operational conditions of U=7 m/s, H_s = 5 m, T_s= 5 s in frequency domain. 86

3.29 Ocean wave force, F_M, for ocean wave periods of T_s = 2 s, T_s = 5 s and T_s = 10 s with H_s =1 m, in frequency domain 87

3.30 Force in the main bearing base R_{bx} for ocean wave periods of T_s = 2 s, T_s = 5 s and T_s = 10 s with H_s =1 m, U= 7 m/s 88

List of Figures (Continued)

Figure Page

3.31 Force in the main bearing base R_{bx} for ocean wave periods of T_s = 2 s, T_s = 5 s and T_s = 10 s with H_s =1 m, U= 7 m/s 88

3.32 Force in the main bearing base, R_{bx} in axial direction, under operational conditions of U=7 m/s, H_s = 1 m, T_s= 2 s in frequency domain 89

3.33 Force in the main bearing base, R_{bx} in axial direction, under operational conditions of U=7 m/s, H_s = 1 m, T_s= 2 s in frequency domain 89

NOMENCLATURE

A	projected area of the member normal to the wind	$[m^2]$
A_R	area of the rotor	$[m^2]$
a	axial induction factor	$[-]$
a'	tangential induction factor	$[-]$
C	shape coefficient	$[-]$
C_D	airfoil drag coefficient	$[-]$
C_L	airfoil lift coefficient	$[-]$
C_n	airfoil normal coefficient	$[-]$
C_t	airfoil tangential coefficient	$[-]$
c	airfoil chord	$[m]$
D	tower diameter	$[m]$
d	water depth	$[m]$
dF_D	drag force on a differential blade element	$[N]$
dF_L	lift force on a differential blade element	$[N]$
dF_N	normal force on a differential blade element	$[N]$
dF_T	tangential force on a differential blade element	$[N]$
F_M	ocean wave force on submerged portion of tower	$[N]$
F_W	wind drag force on tower	$[N]$
f	wave frequency	$[Hz]$
g	gravitational constant, equal to 9.8	$[\mathrm{m}/s^2]$

H_s	significant wave height	[m]
h_t	tower height	[m]
k	wave number	[m^{-1}]
P	power production	[W]
R	radius of the rotor	[m]
R_{bx}	reaction force in axial direction in main bearing	[N]
R_{bz}	reaction force in vertical direction in main bearing	[N]
r	radial position of blade element	[m]
r_{CM}	center of mass position	[m]
T_s	wave period	[s]
t	simulation time	[s]
U	undisturbed wind velocity	[m/s]
U_{ref}	wind velocity at reference height	[m/s]
U_{rel}	relative wind velocity	[m/s]
u	horizontal water particle velocity	[m/s]
w	vertical water particle velocity	[m/s]
x, y, z	set of orthogonal axes	[m]
z_0	surface roughness length	[m]
z_{ref}	reference height	[m]
α	angle of attack	[deg]
α_{shear}	power law coefficient for wind shear	[−]

α'	gust factor	[deg]
χ	angle between the wind direction and the axis of the member	[deg]
$\frac{\partial u}{\partial t}$	horizontal water particle acceleration	[m/s^2]
$\frac{\partial w}{\partial t}$	vertical water particle acceleration	[m/s^2]
λ	wave length	[m]
λ_Ω	tip speed ration	[$-$]
η	water elevation	[m]
θ_p	section pitch angle	[deg]
$\theta_{p,0}$	blade pitch angle	[deg]
θ_T	section twist angle	[deg]
ϑ	phase position of the blade	[deg]
ρ_a	air density	[kg/m^3]
φ	angle of relative wind	[deg]
ψ	phase position	[rad]
Ω	rotor speed	[rpm]

CHAPTER ONE

INTRODUCTION

Overview of wind turbine history

Attempts to produce energy from the wind were first made in 1891 by Poul La Cour in Denmark (Hau, 2006). He first built an experimental wind turbine to utilize wind power for the generation of electricity. In 1908 Lykkegard Company started the industrial utilization of his developments and built various sized wind turbines with power outputs ranging between 10 to 30 kW. This was a departing point in commercializing wind turbines.

Since the beginning of the nineteenth century engineers and scientists have been working on developing wind turbines that could be competitive with other energy sources in power generation. Modern wind turbines generate power efficiently and reliably in a range between 10kW (small land base wind turbines) to 6 MW (large scale off-shore wind turbines) using innovative drive and control technology.

To get more power output, year after year wind turbines tend to grow in size. Such a tendency is shown in Figure 1.1. As can be seen, for the past decade the power production of wind turbines has increased by two-fold and rotor diameter has increased by about 50%. The reason for increasing single wind turbine rotor diameter rather than increasing the number of units in wind farm is related to expenses associated with installation, electrical interconnection, maintenance and access per installed kW of wind farm capacity. These expenses are lowered by increasing unit capacity in a wind farm. Additionally, the power production from single wind turbine, which depends on rotor diameter, will increase.

Wind power is the fastest growing energy resource with an annual growth rate of approximately 20% for the past decades. According to World Wind Energy Association a total

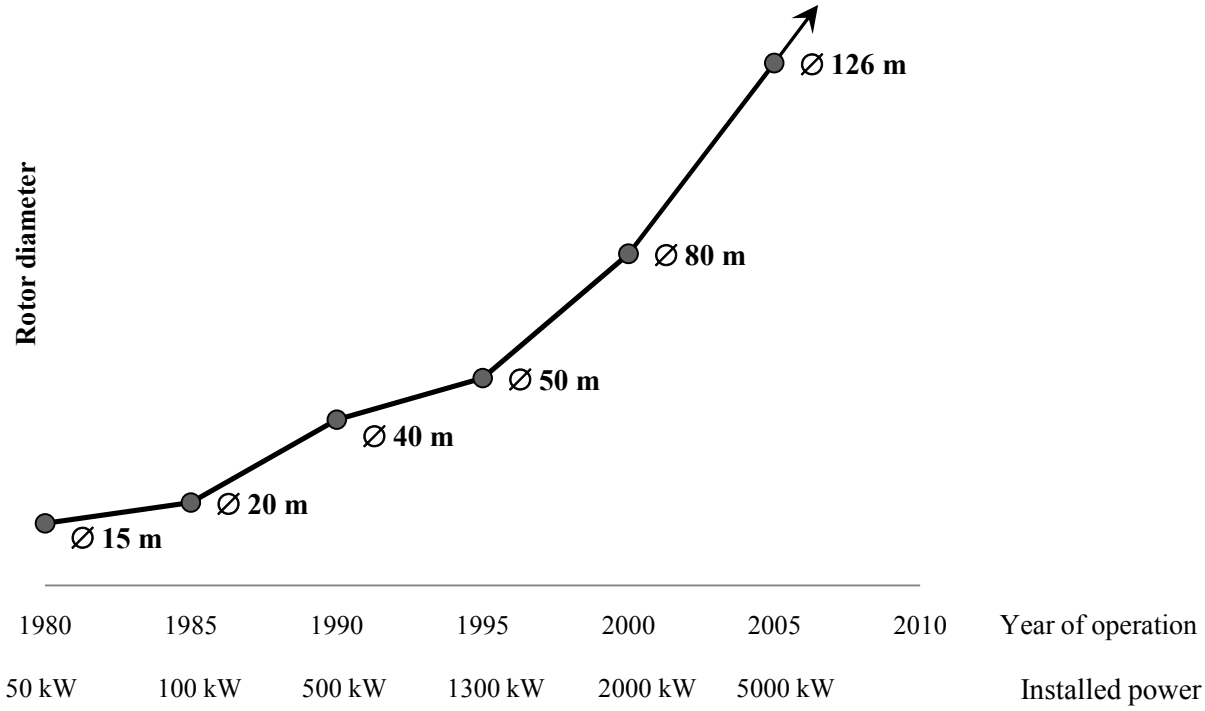

Figure 1.1 Growth in size and power production of wind turbines (EWEA, 2009)

capacity of 121,188 MW was installed worldwide by the end of 2008 (EWEA, 2009; U.S. DOE, 2011), which is about 1.5% of global electricity consumption.

In order to harvest more energy from the wind, places such as coastal regions and deep sea become attractive. In such places larger wind resources are available with reduced turbulence intensity and wind shear. In addition, visual impact along with noise aspects is reduced, especially for sitting far off-shore. Despite the several disadvantages associated with installations and maintenance of wind turbines which require more capital investment, off-shore wind power is a high-priority research area in wind strategy development in Europe and USA for next decades (EWEA, 2009; Fichaux and Wilkes, 2009; U.S. DOE, 2011).

Rationale

A main challenge when designing reliable and efficient wind turbine systems is to estimate forces acting on wind turbines and their various mechanical components. An off-shore wind turbine model together with primary structural components is presented in Figure 1.2. This figure shows the most common turbine configuration. The wind turbine

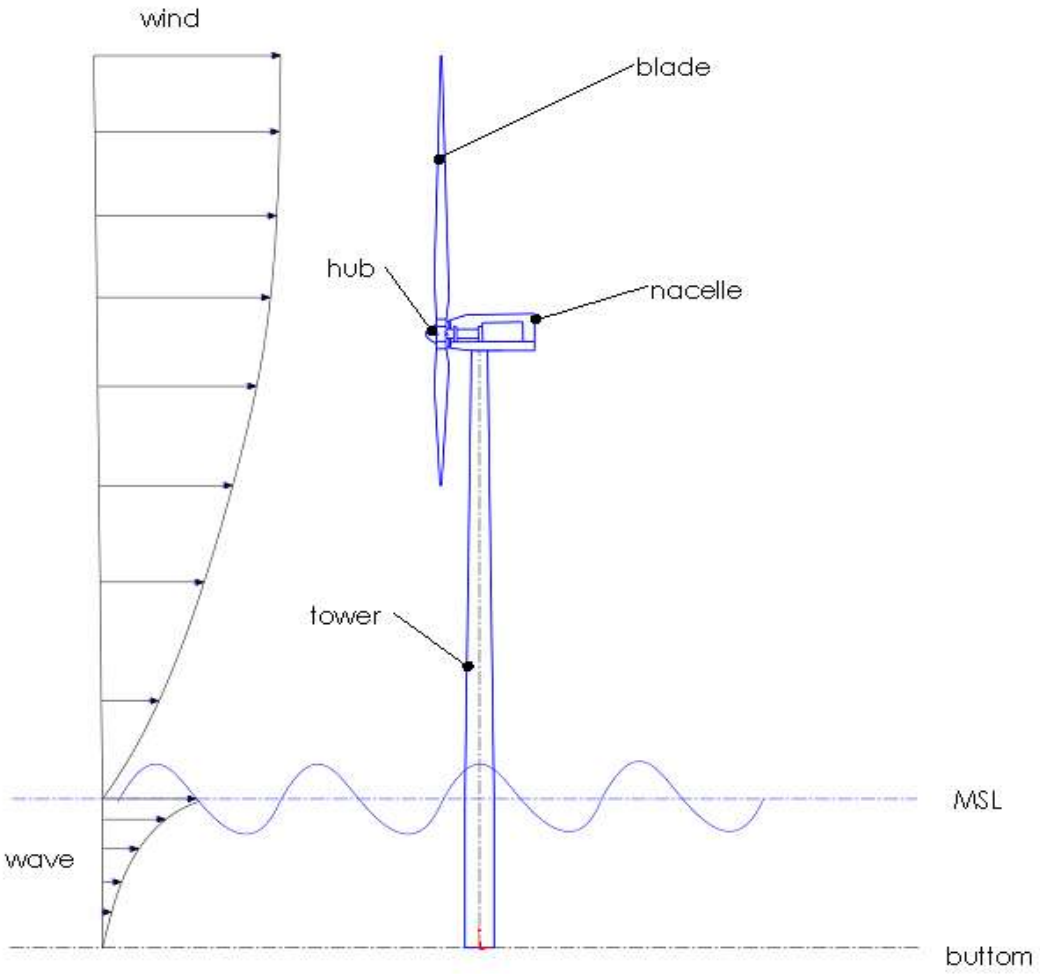

Figure 1.2 Off-shore wind turbine with main structural components

rotor with three blades is the most used in large turbine installations. Turbine shaft components include primarily thrust and journal bearings. These and an electrical generator are housed in the nacelle.

The turbine blades are attached to the shaft via a hub. Commonly, the tower is manufactured as a hollow steel cylinder of constant diameter and thickness for its submerged portion and a tapered tube for the portion extending from the ocean surface to the nacelle.

Wind is a main source of the forces that should be taken into account. When wind interacts with a machine, aero-elastic loads are produced. These types of loads together with other loads acting on the wind turbine system are summarized in Table 1.1.

Table 1.1 Loads on the off-shore wind turbine

Load	Load Behavior	Affected Structural Components
Aerodynamic forces	Periodic, vary in time	Rotor blades and hub
Wind drag	Unsteady, vary with height	Tower
Ocean wave drag	Periodic	Submerged portion of tower
Gravitational forces	Steady	All components

Aerodynamic forces are produced when a rotor rotates. It has normal and tangential components and is not constant in time. Forces are cyclic with magnitudes dependent on blade position. When blades rotate the distance of each blade element above the ocean surface will change. As a result, the value of inflow wind speed for each blade element and consequently the

magnitude of aerodynamic forces changes in time as a consequence of decreasing wind speed nearer to the ocean surface.

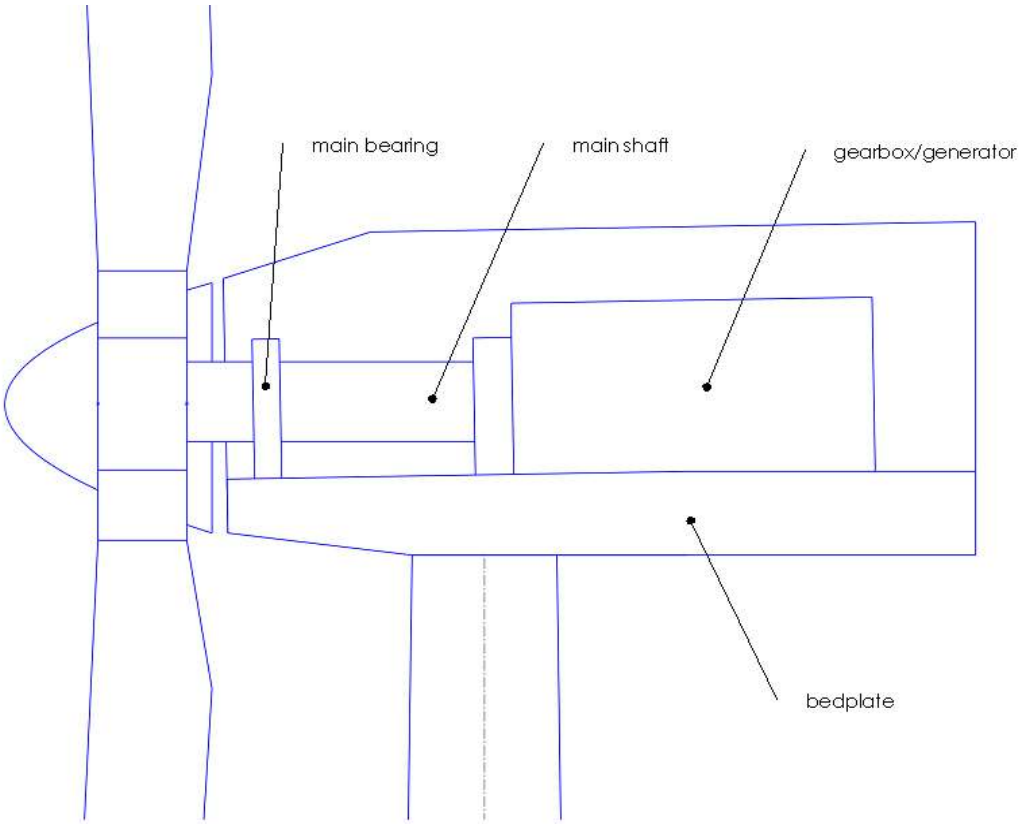

Figure 1.3 Principal nacelle components of a wind turbine

Apart from aerodynamic forces produced by the rotor, wind drag on the tower is constant in time and varies only along tower height. All of the loads mentioned above lead to deflection of the blades and tower oscillation, which in-turn generate forces on the primary nacelle components, such as main shaft and bearings system, which are shown in Figure 1.3.

Off-shore citing of wind turbines brings more complexity, because loads not only originate from wind, but hydrodynamic loads from waves act on the tower. Water waves are a result of external forces, such as wind shear, acting on the water surface and influences of gravity

and surface tension, which act to keep a water surface level. Once a water surface is deformed, gravitational and surface tension forces are activated that cause a wave to propagate (Dean and Dalrymple, 2006). As a result the tower oscillation due to the wind forces can interplay with dynamic wave action. Resulting oscillations are transmitted through the bedplate to cause loads in nacelle components. Additionally, the electric generator produces counter-torque which, through the gearbox, balances the aerodynamic torque produced by rotor. To compute these dynamic loads accurately is necessary, because they will be responsible for fatigue, stresses in structural components, and must be known to design drive train components. Attention to the drive train components is needed in order to ensure their durability. Loads concentration in these parts affects overall system performance increasing failure risks. For instance, replacement of a failed bearing system of a 5MW wind turbine may cost about 20% of initial wind turbine cost so it is very important to ensure long life and reliable performance of these critical components (EWEA, 2009).

In consideration of the foregoing, the effective implementation of off-shore wind turbines requires improved understanding of how various forces affect drive train components.

Literature review

Aerodynamics of wind turbine and wind modeling

One of the main aspects in wind turbine design and analysis is correct prediction of lift and drag forces. Therefore, understanding and application of aerodynamic principles is an essential part of wind turbine development. Aerodynamic theories developed for aircraft and helicopters were successfully applied for defining the performance of wind turbines.

The basic principles of energy conversion for wind turbine rotors were first formulated by Albert Betz (1966). He considered a frictionless free flow with uniform velocity passing through the propeller-like wind turbine. Pressure along the turbine blades was assumed to be distributed uniformly. The air flow was impeded by rotor area and mechanical energy was extracted from the air stream. Using momentum conservation for a control volume and Bernoulli's equation for the fluid flow upstream and downstream of the turbine, Betz obtained an efficiency limit of 59.3 %, where the efficiency was defined as the ratio of turbine power output to the power of uniform free flow passing through an unobstructed area corresponding to the turbine diameter. The efficiency of 59.3% corresponds to reducing the wind speed on the rotor plane to two-thirds of the undisturbed wind velocity and by one-third beyond the rotor. However, the simple momentum theory used by Betz was based on ideal conditions. Actual turbines operate with less efficiency. However, despite the ideal conditions, common physical principles provided by Betz give a good understanding of operation of wind energy converters.

Later, to account for the wake generated by rotor, an extended momentum theory was developed (Hau, 2006; Hansen, 2008). The spin of a wake is opposite to the torque of the rotor, so that power coefficient is smaller than the value established by Betz. For a turbine having a rotational speed Ω and radius R, the power coefficient now becomes dependent on the ratio of the velocity of the rotor tip to undisturbed inflow velocity U. This ratio is commonly called tip speed ratio and is denoted by Equation 1.1.

$$\lambda_{\Omega} = \frac{R\,\Omega}{U} \tag{1.1}$$

To account for rotor blade geometry, blade element (BEM) or strip theory was developed (Wilson and Lissaman, 1974). In this approach the blades consist of strips arranged in the direction along the air foil span and it is assumed that there is no radial dependency between them. The airfoil cross-section with forces and velocities acting on it is shown in Figure 1.4.

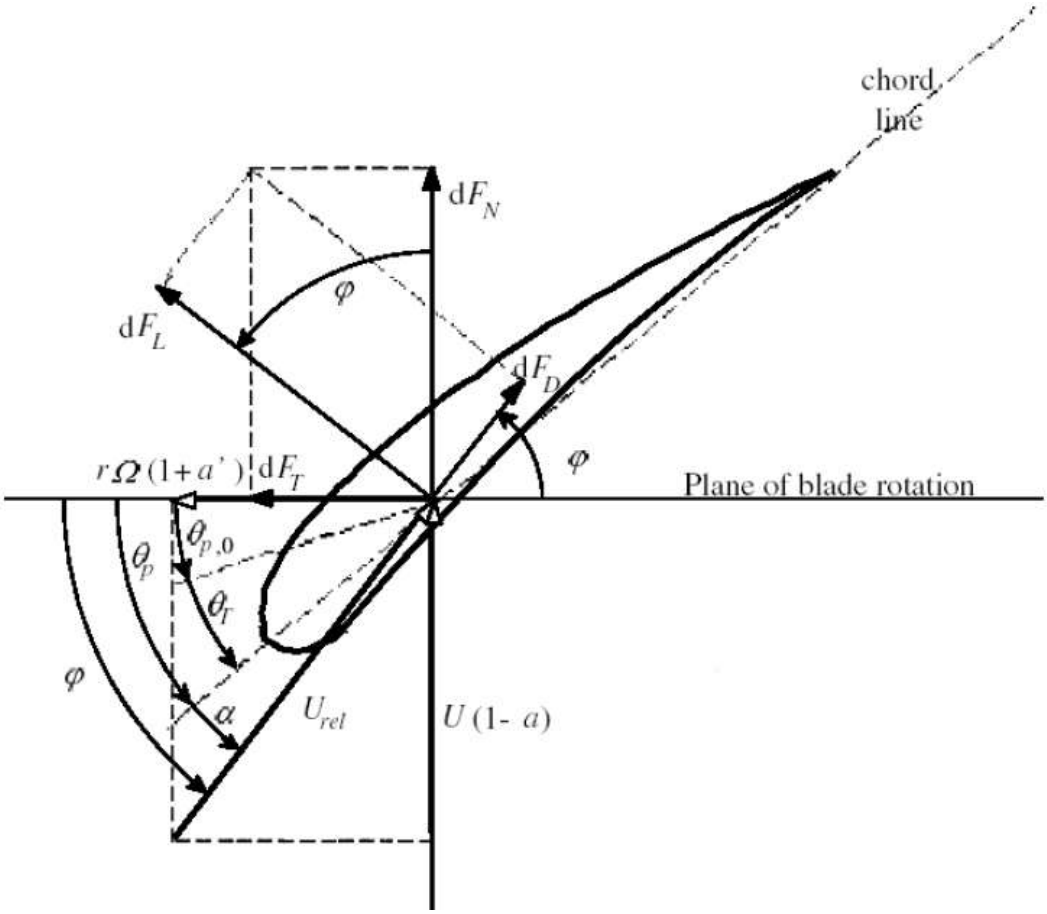

Figure 1.4 Airfoil cross-section of blade element with velocities and forces acting on it (Emrah and Nadir, 2009)

By using momentum conservation, BEM together with axial momentum theory allows the computation of aerodynamic forces acting on blade elements. Following this approach, the

elemental lift and drag forces acting on the blade element are estimated first by Equation 1.2 and Equation 1.3.

$$dF_L = 0.5\rho\, c\, U_{rel}^2\, C_L\, dr \tag{1.2}$$

$$dF_D = 0.5\,\rho\, c\, U_{rel}^2\, C_D\, dr \tag{1.3}$$

Then, the elemental thrust force and rotor torque acting on the blade element are calculated by Equation 1.4 and Equation 1.5.

$$dF_n = dF_L \cos\varphi + dF_D \sin\varphi \tag{1.4}$$

$$dM = r\left(dF_L \sin\varphi - dF_D \cos\varphi\right) \tag{1.5}$$

This is further integrating along span wise direction and multiplied by blades number to obtain the total rotor torque, thrust and power output. More precisely, the main steps of such iterative algorithm are described in Chapter 2.

A variety of studies has been done to implement BEM numerically (Simms et al., 2001; Krogh, 2004; Jonkman, 2007; Emrah and Nadir, 2009; Savenije and Peering, 2009). Modern numerical codes based on BEM are iterative algorithms and include corrections associated with axial induction factor. Such corrections are Prandtl tip-loss factor and Glauret correction (Glauret, 1935). Prandtl tip-los factor corrects the assumption of an infinite number of blades in BEM theory. The Glauret correction, from the other hand, is an empirical relation between the thrust coefficient and axial induction factor. This relation should replace that derived from the one-dimensional momentum theory, which is no longer valid when the axial induction factor becomes greater than 0.2.

The sectional airfoil-data for BEM should be corrected in order to account for three-dimensional and rotational behavior. Numerous studies have been performed to define the most appropriate correction. Different models were developed. Corrigan and Schillings (1994) used a stall delay model. Hansen and Chaviaropoulos (2000) investigated three-dimensional and rotational effects on wind turbine blades using a quasi three-dimensional Navier-Stokes equations solver. Lindenburg (2004) conducted comparative research on rotational augmentation effect using the program PHATAS, which has BEM model for rotor aerodynamics. He showed the influence of such corrections on computed shaft torque in Figure 1.5, especially for high wind speed.

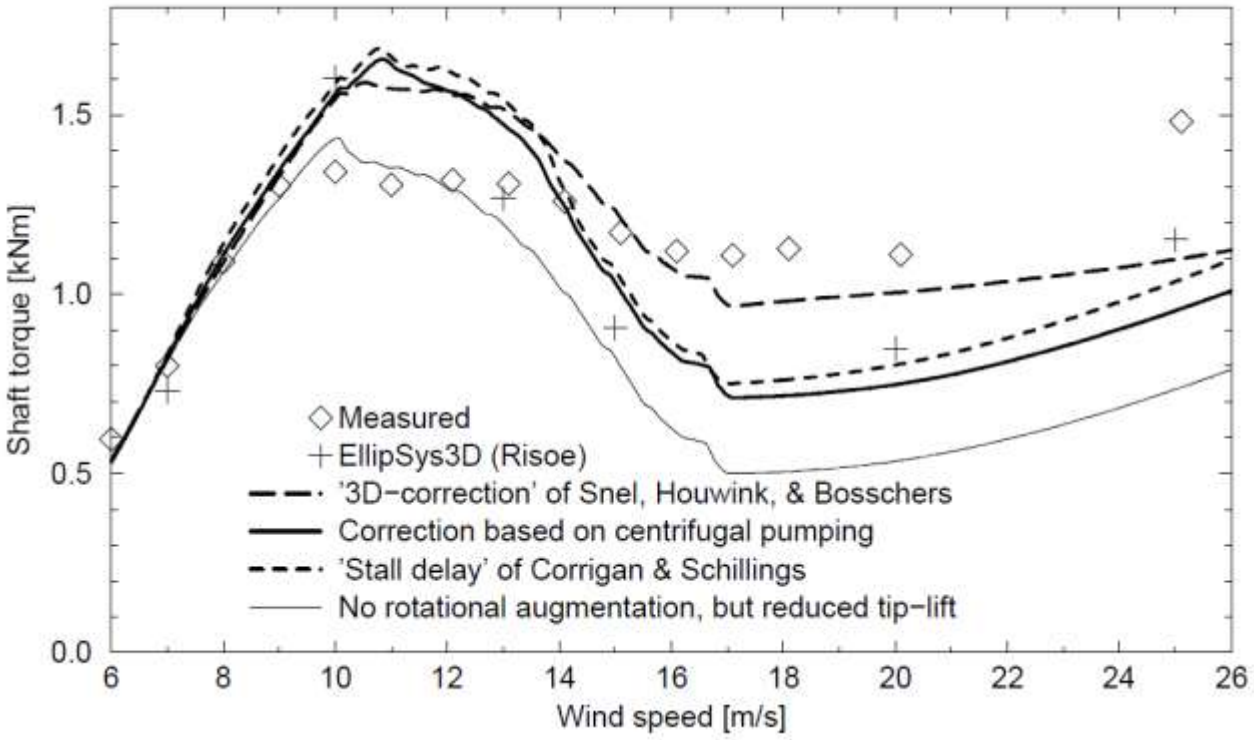

Figure 1.5 Shaft torque measured and calculated by different techniques (Lindenburg, 2004)

In above figure, for wind speeds up to 8 m/s measured and predicted shaft torque showed a good agreement because the rotor was not in stall. Starting from wind speed of approximately 10 m/s to 15 m/s each of the correction models predict higher torques than measured values. This may raise some doubts about accuracy of measurements by relatively good agreement of different correction models. This may be concluded despite the relatively good prediction using 2D aerodynamic coefficients for this wind speed range. However, for high wind speed, better fitting of the measurements was shown by stall delay correction model, developed by Corrigan and Shilling (1994), which is used often in wind turbine aerodynamics.

Power output from a wind turbine depends most strongly on wind speed U. A cubic dependence for a rotor having area A_R is given by Equation 1.6

$$P = \frac{1}{2} \rho_a \, A_R \, U^3 \tag{1.6}$$

Due to this relation even small reductions in wind speed will affect the amount of power output. Hence, site selection is an important consideration. Above equation also shows why rotor diameter increases the power production of wind turbine.

Wind speed varies with distance above a surface. It can also be affected by the surface characteristics and the vicinity of obstructions such as buildings or trees. In Figure 1.4, the wind speed profile is given.

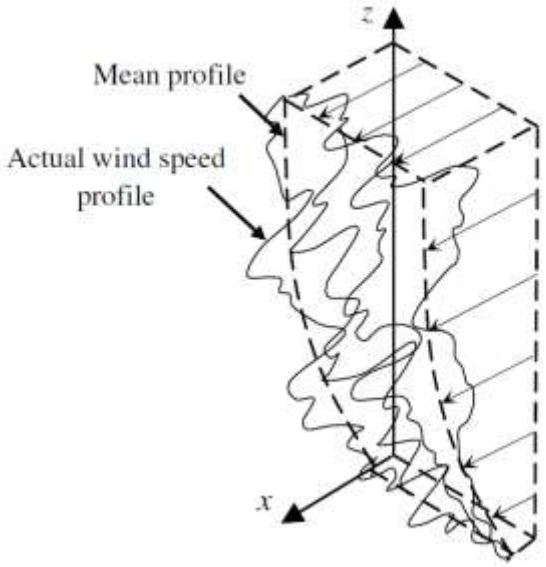

Figure 1.6 Wind speed profile above a surface (Eecen, 2003)

Due to the turbulence in the air flow, instantaneous air speed is stochastic. However, a profile can be used of the time-averaged wind speed which is subsequently referred to as the mean wind speed. The effect of changing mean wind speed with height is known as wind shear. There are two models used to describe the shear effect on the mean wind speed at some height: power law profile and the logarithmic law profile which are given by Equations 1.7a and 1.7b (Myers, 1969).

$$U(z) = U_{ref}\left(\frac{z}{z_{ref}}\right)^{\alpha_{shear}} \qquad U(z) = U_{ref}\frac{\ln\left(\frac{z}{z_0}\right)}{\ln\left(\frac{z_{ref}}{z_0}\right)} \qquad (1.7a, b)$$

For off-shore conditions the shear exponent is set to be 1/7 and the reference wind velocity U_{ref} in Equations 1.7 usually refers to the wind speed at the hub position (Myers, 1969).

In addition to mean wind speed, the wind speed distribution is important. It gives information about the number of hours for which wind speed is within a specific range

(Sathyajith, 2006). A variety of different probability functions were fitted with field data to obtain the most suitable statistical distribution for wind speed regimes. To date, the Weibull distribution is a preferred solution (Sathyajith, 2006). In this case, the probability density function and the cumulative distribution function of wind speed are characterized by shape and scale parameters. These parameters are estimated using various methods, such as the standard deviation method, the moment method, or the graphical method (Sathyajith, 2006). In some cases, a simplified form of the Weibull model is used. This simplified form is referred to as the Rayleigh distribution.

Rotor and drive train design

Two of the most important components in the wind turbine system are the rotor and drive train. Components of a wind turbine rotor, which have been presented in Figure 1.2, are blades, hub and other internals components such as bearings. The rotor captures power from the wind and transforms it to the mechanical power on the shaft. For this purpose different rotor designs were developed. Rotors can be drag-type or rotors can make use of aerodynamic lift (Hau, 2006); however, a more common classification is based on constructional design position of the axis of rotation and number of the blades.

The horizontal axis wind turbine (HAWT) is perhaps the most common constructional design. It is a "propeller-like" concept and is the preferred design of large modern wind turbines. The vertical axis wind turbine (VAWT) also has been considered as a promising concept. Different variation of VAWT, such as Darreius VAWT design with its variation, called H-rotor (Hau, 2006; Sathyajith, 2006) and concept proposed by Savonius, who developed a pure drag-type rotor (Hau, 2006), were investigated. However because of the low tip-speed ratio and low power coefficient these concepts have become less used than HAWT designs. Different rotor designs are compared in Figure 1.7 with respect to power coefficient, which depends on the tip

speed ratio. Figure clearly shows that a HAWT with three blades will generate more power in comparison to other rotor concepts hawing the same rotational speed and operating under the same condition.

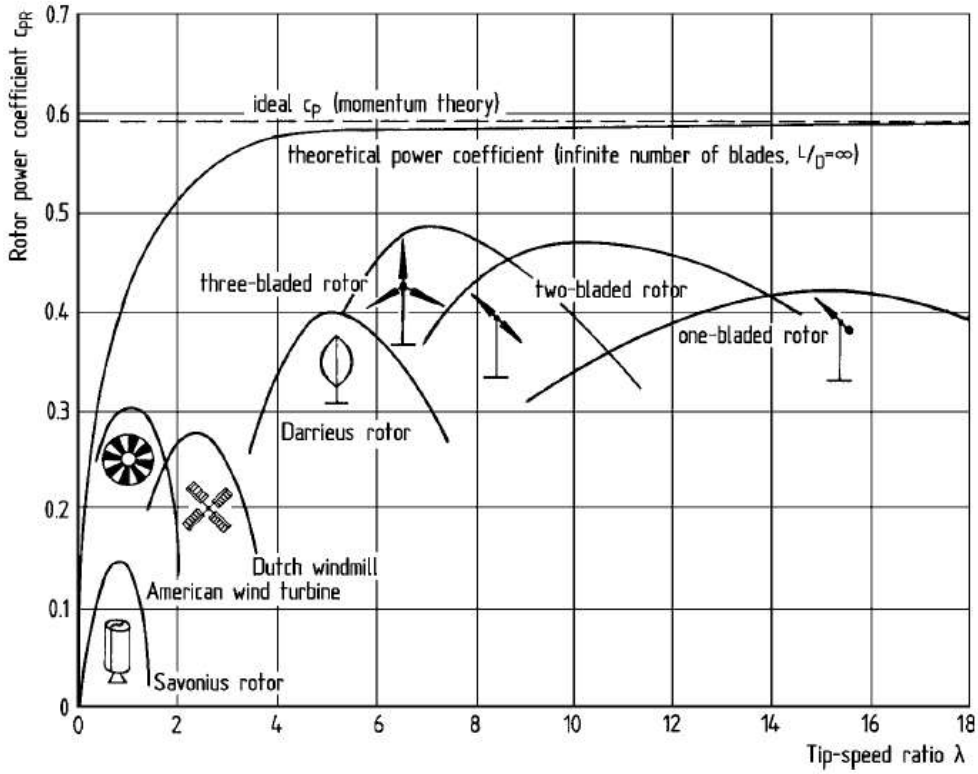

Figure 1.7 Power coefficient for different rotor designs (Hau, 2006).

Moreover, application of "propeller-like" concepts allows control of rotor speed and position of the blades. In modern HAWT, a blade pitch mechanism and stall regulation mechanisms are used to regulate the position of the blades in high wind speeds so power output will not exceed the rated value while also keeping power coefficient as high as possible.

The number of the blades also plays an important role in power production. Even though some attempts were made to use one- and two-bladed designs, they are not used often because of several disadvantages (EWEA, 2009). They have less aerodynamic efficiency than three-bladed

turbines and are sometimes regarded as visually less desirable. Less desirable appearance pertains especially to the single-bladed wind turbine. Multi-bladed turbines are only used for small-scale turbines for water pumping and are not considered for large-scale turbines.

Another high-priority wind turbine component is the drive train, which converts mechanical energy from rotor rotation into electricity. Primary components of the drive train are the main shaft, high speed shaft, gearbox and bearings shown in Figure 1.3. These and the generator are housed in the nacelle. The main shaft, a so-called low-speed shaft is fixed into the bearing system. It translates the aerodynamic torque generated by the rotor into gearbox. Further, through the high-speed shaft the aerodynamic torque is translated to generator.

The main goal when design a drive train is to increase the reliability of drive train components and reduce cost associated with manufacturing and maintenance .To reduce the weight of the drive train, direct-drive technology has been applied. Avoiding the gearbox the direct drive generator is directly coupled to the rotor and operates at the same rotational speed. Since early 1990s lots of companies in Europe have been trying to use direct-drive mechanism. The most successful was Enercon GmbH, one of the world's biggest wind energy companies, which committed a big part of its research and investments to direct-drive technologies. However, to date direct-drive system yield to conventional drive trains in terms of cost. Another way to reduce power train cost through the gears modification is to utilize hybrid single stage of gears and multi-pole generators. These concepts are not well analyzed yet and have been used only by Aerodyn and WinWinD companies.

In addition to the gearbox concepts, another power train component that could reduce the total cost of the wind turbine systems is the main shaft together with bearing system. Slender and tapered main shaft designs are implemented in modern wind turbines. Different bearing configurations are proposed and analyzed to achieve higher and more reliable performance

(Ionescu and Pontius, 2009). To date, the most common main shaft bearing system design is a combination of fixed bearing (so-called main bearing), which carries the axial and radial loads from the rotor, and floating bearing , which carries only radial loads. Both bearings are mounted in bearings housings and bolted to the bedplate. Earlier configuration of bearing system consists of single double-row radial spherical roller bearings (SRB), but recent studies have shown that this configuration should be avoided. The permissible ratio of axial-to-radial loading for two-row SRB is between 0.15 and 0.2 (Ionescu and Pontius, 2009). However, since this ratio at a position of fixed bearing for large wind turbine is often in vicinity of 0.6 (Ionescu and Pontius, 2009) the bearing cannot operate as it was originally designed. The Timken Company suggested another solution for main shaft support bearings. They applied a combination of double-row tapered roller bearings (TDI) and cylindrical roller bearings (CRB), for fixed and floating bearing respectively (Ionescu and Pontius, 2009). Such a combination reduced axial main shaft movement and maximized global stiffness of the system.

Occasionally, the cast iron low-speed shaft is hollow, in order to meet weight, cost and performance requirements, all of which are very important to the design process.

Ocean wave modeling

As was mentioned earlier, the off-shore environment gives additional dynamic behavior originated from wave-induced kinematics. To capture this behavior the appropriate ocean wave model has to be applied.

For most cases, when the wave height is small compared to water depth and wave length, the linear wave theory or so-called airy theory can be used (Myers, 1969; Stewart 2008). The water particles move in circle in deep water in accordance with harmonic waves as shown in

Figure 1.8. When the water depth gets smaller with respect to wave length, so-called intermediate water depth, the seabed response transforms circular motion of particles into elliptic.

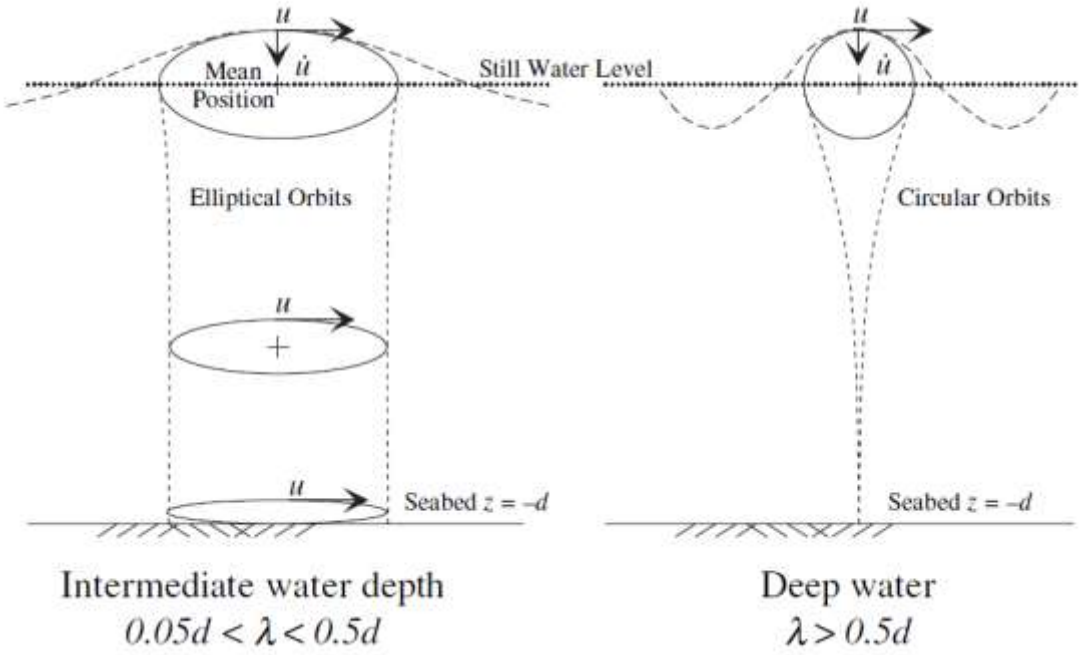

Figure 1.8 Motion of water particle described by linear wave theory.

Measuring time series of the wave height H_s and wave period T_z ,the water particle velocity and acceleration can be computed from Equations 1.8 – 1.12 using the coordinate system defined in Figure 1.9 period.

$$u = \frac{\pi H_s}{T_z} \frac{\cosh k(d+z)}{\sinh kd} \cos\psi \tag{1.8}$$

$$w = \frac{\pi H_s}{T_z} \frac{\sinh k(d+z)}{\sinh kd} \sin\psi \tag{1.9}$$

$$\frac{\partial u}{\partial t} = \frac{2\pi^2 H_s}{T_z^2} \frac{\cosh k(d+z)}{\sinh kd} \sin\psi \tag{1.10}$$

$$\frac{\partial w}{\partial t} = -\frac{2\pi^2 H_s}{T_z^2} \frac{\sin k(d+z)}{\sinh kd} \cos\psi \tag{1.11}$$

$$\eta = \frac{H_s}{2} \cos\psi \tag{1.12}$$

In Equations 1.9 - 1.11, the wave number $k = \frac{2\pi}{\lambda}$ the phase angle $\psi = kx - ft$, and the wave frequency $f = \frac{2\pi}{T_z}$.

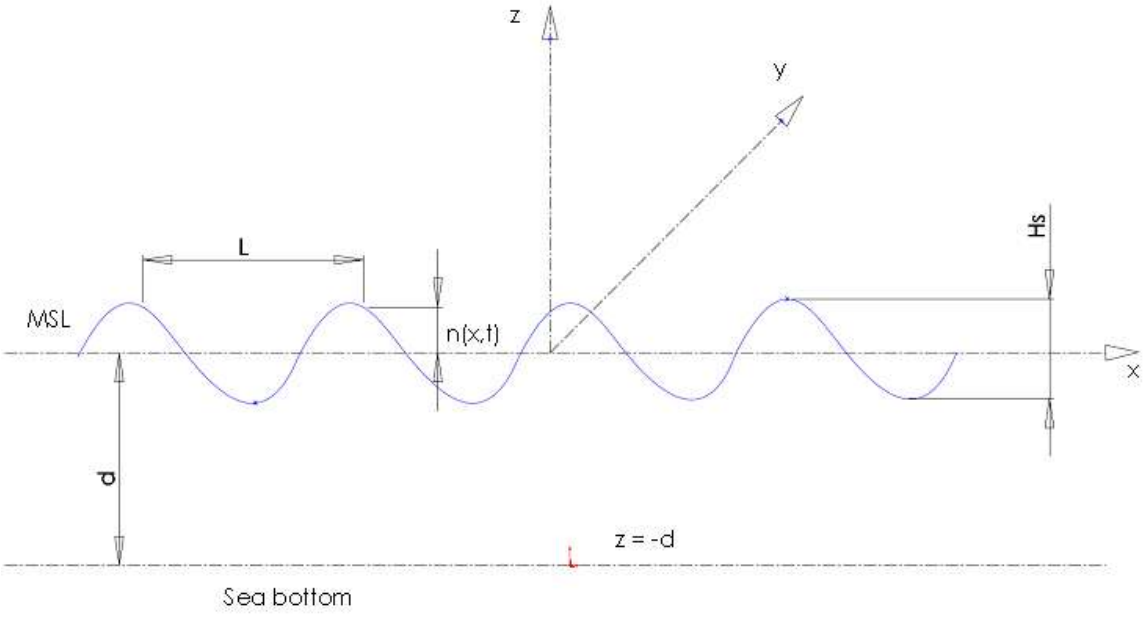

Figure 1.9 System of small-amplitude waves.

Apart from linear wave theory, nonlinear wave theory is used in occasions when physically observed wave phenomena cannot be explained by airy theory. Instead of use a linearized boundary condition, the nonlinear wave theory involves application of perturbation approach with nonlinear boundary condition to solve basic equations governing ocean wave motion (Myers, 1969; Dean and Dalrymple, 2006; Stewart 2008). Application of such theory is more complicated but still implemented in variety of projects (Eecen, 2003; Tempel, 2006).

Support structures

As was mentioned previously, the off-shore environment brings complexity to wind turbine analysis due to ocean wave effects. This complexity is amplified due to more complicated support structures for off-shore wind turbines. The tower represents around 20% of investment cost for land based wind turbine and 25% (5 MW turbines) to 34% (2 MW turbines) of the total system cost in 25 m depth for off-shore wind turbines (EWEA, 2009; Sathyajith, 2006). Therefore, much attention should be given to design the most appropriate foundation which will benefit in cost reduction and ability to handle more severe sea conditions.

Efforts to move wind turbines off-shore benefitted from techniques of the oil and gas industry. To develop cost effective foundations, modifications to manufacturing and design processes were also made. As a result, depending on site conditions and project economics, different types of substructures would be more preferable (Fichaux and Wilkes, 2009). The progression of using different support structures are illustrated in Figure 1.10.

To date the most favored solution is gravity-based structures and mono-pile substructures due to its simplicity in design, fabrication, and installation. However, some disadvantages still might be presented, which are associated with pre-drilling and removal procedure. This type of foundations is suitable in water depth up to 20 m - 30 m. However, with wind turbine growing in size and migrating to deep-water, where more wind resources are available this technology becomes not feasible.

In this case, different variations of space-frame substructures are used. Tripod, quadropod and “jacket” foundations become more economically feasible (Fichaux and Wilkes, 2009). These types of structures are installed in depths up to 50 m and are better suited to heavy large-scale turbines. However, at depths more than 60 m, floating support platforms, such as spar buoy and semi-submersible platforms, are more beneficial solutions.

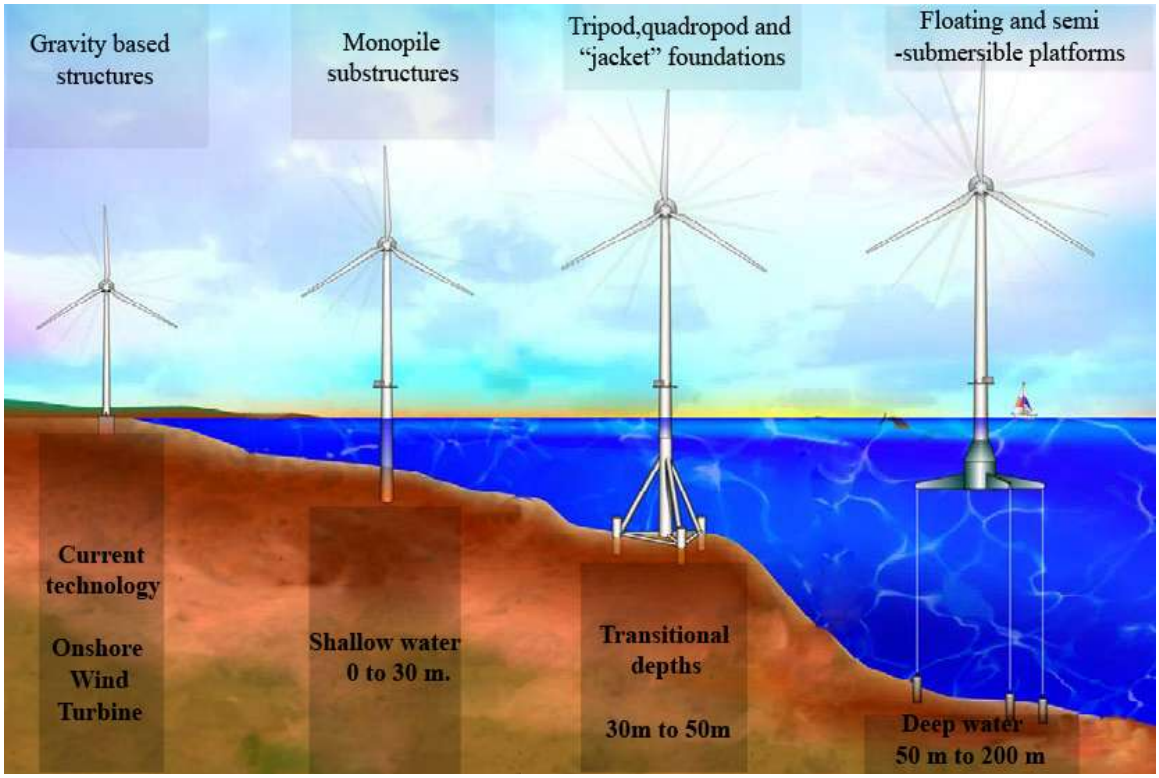

Figure 1.10 Support structure design for different water depths (Jonkman, 2007).

To date, some projects have been done to determine dynamic responses of such structures. Jonkman (2007) presented a sophisticated loads analysis and dynamic modeling for off-shore floating wind turbines. Another study of floating wind farm was done by Shim (2007). He performed a dynamic analysis and investigated the rotor-floater coupling effects on wind turbine dynamics. Jonkman (2007) and Shim (2007) showed that mean values of loads and deflections in the floating turbine were very similar to those that existed on land. However, the excursion of the loads and deflections exceeded those found on the land mostly due to the floating barges motion.

However, despite a variety of projects to investigate floating concepts, the wind production cost for such wind turbine concepts is higher than for bottom-fixed types (Fichaux and Wilkes, 2009).

Related works

In earlier section, simulation tools that have been expanded to capture dynamic response of wind turbine structural components were reviewed. A variety of research was conducted to account for hydrodynamic loading on support structures of off-shore wind turbines (Eecen, 2003; Eicher, 2003; Krogh, 2004; Van der Tempel, 2006; Jonkman, 2007). Most projects focused on dynamic responses of wind turbines with fixed-bottom mono-pile foundations which is the core design for modern off-shore wind turbine systems. To represent hydrodynamic effects, all of these codes use Morrison's equation. This representation is most appropriate for slender cylinders, which is usually used for the submerged portion of the off-shore wind turbine tower. For incident-wave kinematics these codes use linear ocean wave theory and occasionally more complicated nonlinear ocean waves.

Eecen (2003) performed a calculation of ocean wave forces on the off-shore wind turbine using the PHATAS code. He developed two ocean wave simulation tools to describe linear and non-linear ocean waves and then modeled extreme loads on offshore wind turbines to calculate mainly fatigue loads. Eicher (2003) performed a parametric study and defined stresses and deformations of off-shore piles under wave and structural loading. Both of the projects considered just single support structure with no rotational excitation from wind turbine rotor. Van der Tempel (2006) used the frequency-domain analysis to design a support structure for 2MW Vestas V66 off-shore wind turbine. His approach separated the support structure from the wind turbine. Coupling between the two was modeled with a frequency transfer function. This is practically used in off-shore engineering method to analyze dynamic response of structure under different loads. Additionally, this technique was used by Savenije and Peeringa (2009) to performed aero-elastic simulation on 6MW DOWEC (Dutch off-shore wind energy converter)

off-shore wind turbine. For this purpose they used linearized frequency domain tool called TURBU.

An extended research for a floating 5MW NREL wind turbine was conducted by Jonkman (2007). He developed aero-hydro-servo-elastic model in both frequency and time domain. FAST with AeroDyn and ADAMS with AeroDyn were used as a design codes. These are wind turbine simulation tools for land-based turbines which were upgraded by Jonkman to include additional hydrodynamic loading and motion representative of off-shore turbines. For the calculation of aerodynamic forces, these codes use the combined blade element and momentum theory. The hydrodynamic loading was calculated by use of linearized Morison's equation. Based on this research, Agarwal (2008) presented work on structural reliability of off-shore wind turbines. Considering fixed-bottom wind turbine model he investigated reaction forces at the tower base. In his study he used nonlinear wave theory to model ocean waves. A utility scale 5MW wind turbine sited at 20 m waters was similar to those used by Jonkman (2007) to compare land-based wind turbine loading with floating systems. One limitation could be addressed to work done by Agarwal (2008). The wind model he used is based on onshore condition which may not be adequate for off-shore site.

Another study for loads simulation of generic 5MW off-shore wind turbine was conducted by Krogh (2004) and sponsored by Risø National Laboratory for Sustainable Energy in Technical University of Denmark (DTU). He considered upwind oriented wind turbine with fixed-bottom mono-pile foundation. The simulations were carried out using the horizontal axis wind turbine aero elastic code version T2B which is based on aero elastic model formulated in time domain. The calculation of aerodynamic loads was based on combined blade element and momentum theory. The mean wind field over the rotor included wind shear and tower interference by use a potential flow model. The nacelle and the rotor were both represented as

rotating substructures, coupled to each other and to the tower. Finite element model developed by Krogh (2004) were based on two nodes prismatic beams element. This implied an approximation in representation of the blades, which are both tapered and twisted in actual wind turbine. Flexible elements were modeled with mass, stiffness and structural damping. Last one was modeled as a proportional damping by a linear combination of the stiffness and mass matrixes. Distributed aerodynamic and gravitational loads on the elements were consistently transformed to the nodes. This guaranteed a coupled dynamic model for the response of the wind turbine. Time-domain simulations were run for both conditions, when blades are parked and when rotor rotates. Varying a sea-state condition and wind speeds, Krogh (2004) showed dynamic motion of wind turbine structural components. Calculated tower top thrust and lateral forces, tower base normal and lateral forces and tower forces in normal direction at sea level were presented in form of minimum, maximum and mean value of these variables.

Objective

Based on the literature review, the main objective of this study was to model the dynamic forces that are present on drive train components for an off-shore wind turbine. Due to combined wind and ocean wave action, generated forces in drive train components may differ from those for land-based wind turbines. To decrease risk of failure, influences of different wind speeds, ocean wave heights and ocean wave periods on force levels and dynamical variations in forces were investigated.

CHAPTER TWO

ENGINEERING MODEL

Model description and assumptions

This section documents the specifications of the developed wind turbine model. As mentioned in Chapter 1, increasing single wind turbine capacity reduces the expenses associated with maintenance and installation by lowering the number of units in the wind farm. To date, wind turbines of 5MW capacity and above are the preferred solution for offshore wind farms. However, wind turbines rated above 7.5 MW have not yet been installed. The highest power for a modern wind turbine was achieved by Enercon GmbH, the fourth-largest wind turbine manufacturer in the world which is based in Germany. This company has installed the world's most powerful wind energy converter, the E-126/7.5MW wind turbine. Hence, for the current project, the wind turbine power rating has been chosen to be 5 MW. This power is based on the U.S. D.O.E. NREL Offshore 5 MW Baseline Wind Turbine and Denmark RisØ DTU National Laboratory Generic 5 MW Offshore Wind Turbine. Technical specifications from these projects were utilized to develop a realistic representation of an off-shore wind turbine system. The main characteristics of wind turbine structural components such as blades, nacelle, tower and bearings are given in following sections of this chapter.

The main components of an offshore wind turbine have been shown in Figures 1-2 and 1-3 of Chapter 1. The wind turbine for this project has three blades each with a radius R of 63 m. The rotational speed of the rotor Ω depends on wind speed U so that optimal wind-power conversion efficiency is kept. Figure 2.1 shows this relation between Ω and U.

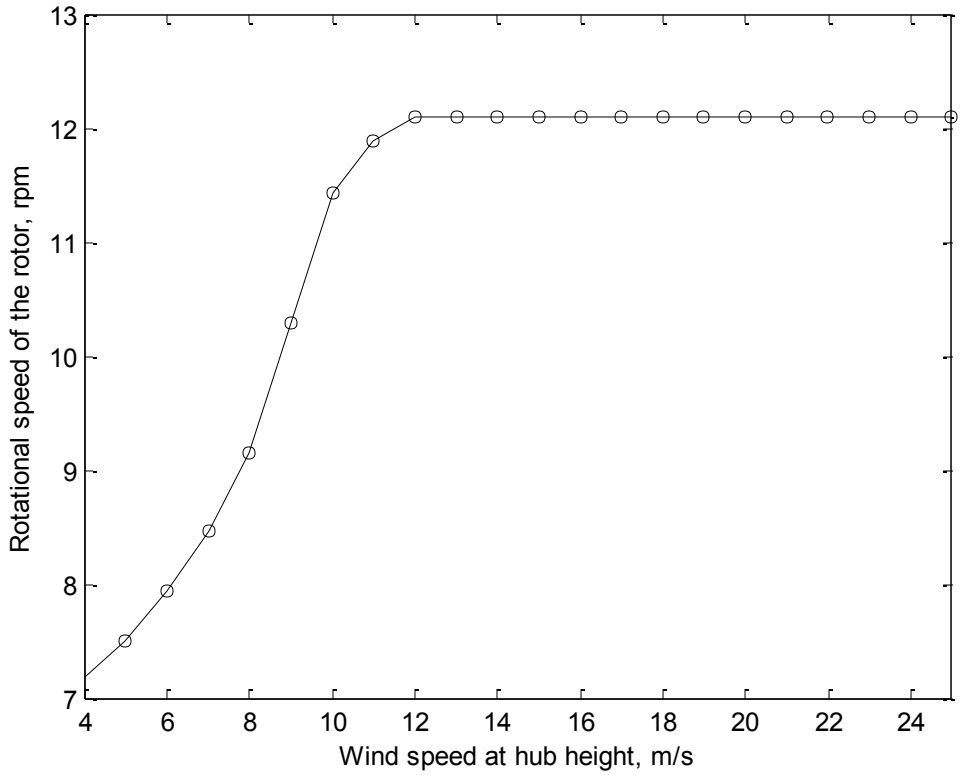

Figure 2.1 Rotational speed of the rotor versus wind speed at hub height (Jonkman, 2007).

As can be seen from above figure, at a wind speed of 7 m/s, the wind turbine has a rotational speed $\Omega = 8.469\,rpm$, which denotes the nominal operating condition.

The hub height h_t has to be minimized in order to reduce the bending moment acting on the tower. However, the vertical distance between the wave height and blade tips at their lowest point should be large enough to allow good air flow past the turbine. As a result of this trade-off, h_t = 90 m. The specifications of the modeled offshore wind turbine are summarized in Table 2.1. Although most specifications are identical to those of the NREL 5MW baseline wind turbine (Jonkman, 2007), some simplifications were made in the rotor design. The rotor tilt and the turbine blade pre-bend were ignored, which simplify the analysis of dynamic response.

Table 2.1 Properties chosen for the modeled offshore wind turbine

Rated power	5 MW
Rotor orientation	Upwind
Rotor radius	R = 63 m
Hub height	$h_t = 90$ m
Cut In, Cut out wind speed	4 m/s, 25 m/s
Rotational speed of the rotor	$\Omega = 12.1$ rpm
Rotor mass	$m_R = 110\ 000$ kg
Nacelle mass	$m_N = 240\ 000$ kg
Tower mass	$m_t = 1\ 066$ ton

Several assumptions were invoked in developing the model. Taken together, these assumptions restrict the model applicability to certain off shore wind turbines operating under conditions of steady wind speed, wind direction, and ocean wave conditions. Specific assumptions are listed in Table 2.2 below and are followed by a discussion of each one.

Table 2.2 Assumptions invoked in model development

Assumption	Affected Components
Perfectly rigid and bottom-mounted	Submerged portion of wind turbine tower
Fixed pitch angle	Wind turbine blades
Blades are considered perfectly rigid	Wind turbine blades
Fluid-structure interaction is modeled as externally applied forces	Wind turbine tower and blades

The first assumption addresses the submerged part of wind turbine tower. It is considered bottom-mounted and perfectly rigid. This allows for use of Morison's equation (Morison et al., 1950) to find wave loading on structure.

Another assumption relates to the control mechanism. In current work, no control mechanisms are considered to regulate power production. Pitch angle of the blades does not change due to corresponding change in wind speed. However, in modern wind turbine systems, both stall delay and pitch mechanisms are invoked to regulate the blade's position. Moreover, the wind is modeled to blow in one direction, normal to the tower centerline, so the yaw angle is equal zero. As a result, the gyroscopic forces originating when rotating rotor is yawed into the wind are not included in analysis.

Lastly, another assumption is related to modeling fluid-structure interaction between wind, wave and tower and their effect on wind turbine drive train components. The dynamics of the blades and possible effects of these dynamics on air flow past the blades and on forces generated in the drive train were not included. Instead, a method similar to that used by Van der Tempel (2006) and Savenije and Peeringa (2009) was applied. Aerodynamic forces originating from the rotating rotor were calculated separately and were applied as boundary conditions in a detailed computational model of other components. Unsteadiness in aerodynamic forces due to changing proximity of the blades with the sea, however, were incorporated.

The wave action and wind action on the tower were modeled as additional externally applied drag forces. Nacelle structural components, such as main shaft, gearbox and generator, were represented as distributed or point loads. The algorithm to calculate aerodynamic and structural forces is discussed later in this chapter along with a description of how these were utilized in a finite element model to simulate dynamical forces at the drive train.

Modeling of wind turbine components

Wind turbine site selection

The nearby South Carolina coast was chosen as the basis for a 5MW off shore wind turbine for the model. The most suitable area for placing an offshore wind turbine farm was determined by considering four variables: wind speed, water depth, distance to the shoreline, and distance to navigable waterways (Jeffery et al., 2006).

Wind speed and wind power density are the main criteria in site selection process. Wind is classified with respect to the wind power density. For instance, class 4 represents a wind power density of about 500 W/m^2 and relates to wind speed of 7 m/s at 50 m height above the ground (Jeffery et al., 2006). To date, the most appropriate solution for a large offshore wind turbine is power class 4 and above. South Carolina has a good potential for offshore wind resources with averaged wind speed $\geq 7\ \mathrm{m/s}$ at 50 m elevation above the mean sea level. This is shown on Figure 2.2.

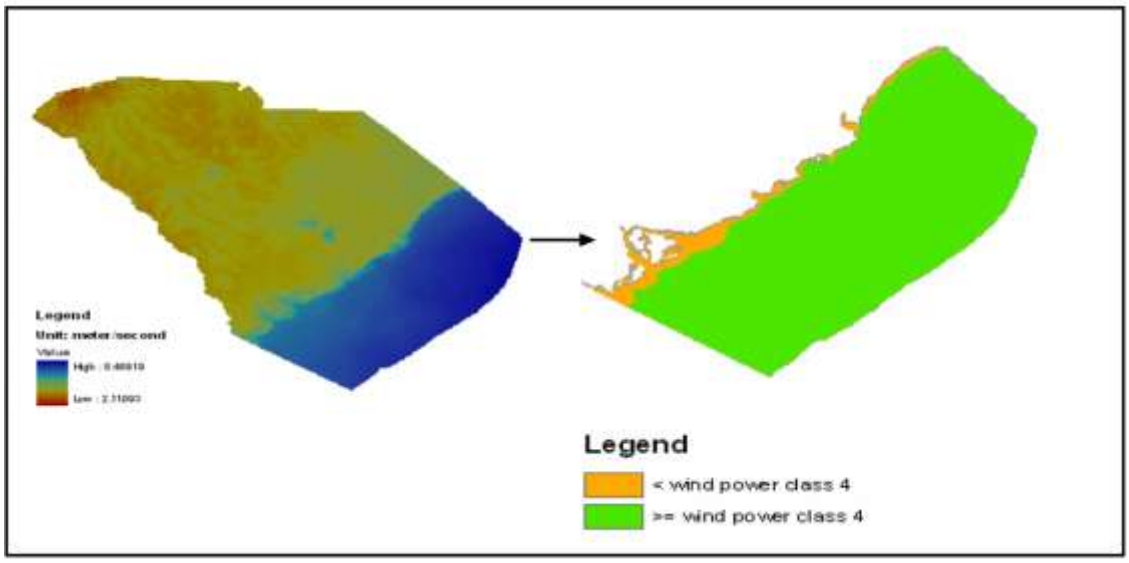

Figure 2.2 South Carolina wind speed at 50 m elevation above the ground (Jeffery et al., 2006).

Another important factor when placing a wind turbine offshore is water depth. For the developed offshore wind turbine with a sea bottom-mounted foundation, the maximum water depth is about 30 m (Jeffery et al., 2006). The Geophysical Data Center of National Oceanic and Atmospheric Administration (NOAA) created a Coastal Relief Gridded Database that presents bathymetric data of United States seacoast. For the South Carolina region, bathymetry data is given on Figure 2.3. It clearly shows the region with suitable water depth along the South Carolina coast for placing an off-shore wind turbine.

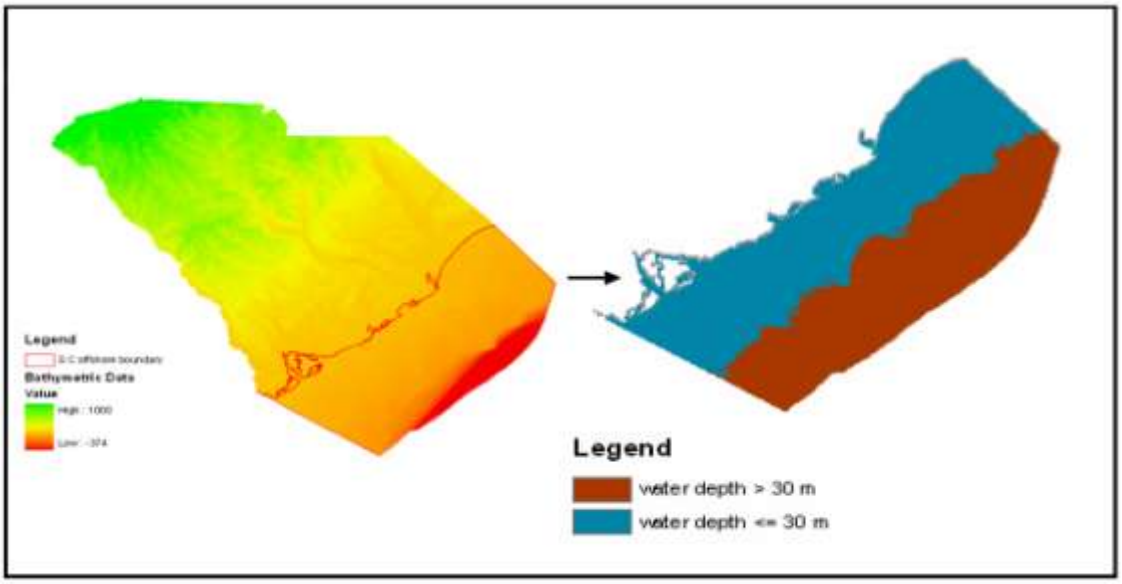

Figure 2.3 South Carolina bathymetries in meters (Jeffery et al., 2006).

Another important factor is the distance to shoreline. Wind turbine noise and visual impact limitations require the wind farm to be installed at sufficient distance from the coast. In the USA, the location of the wind farm should be a minimum distance of three nautical miles from the shoreline (Jeffery et al., 2006). In Figure 2.4, the distance to the shoreline for South Carolina coast is presented according to the NOAA Coastal Services Center.

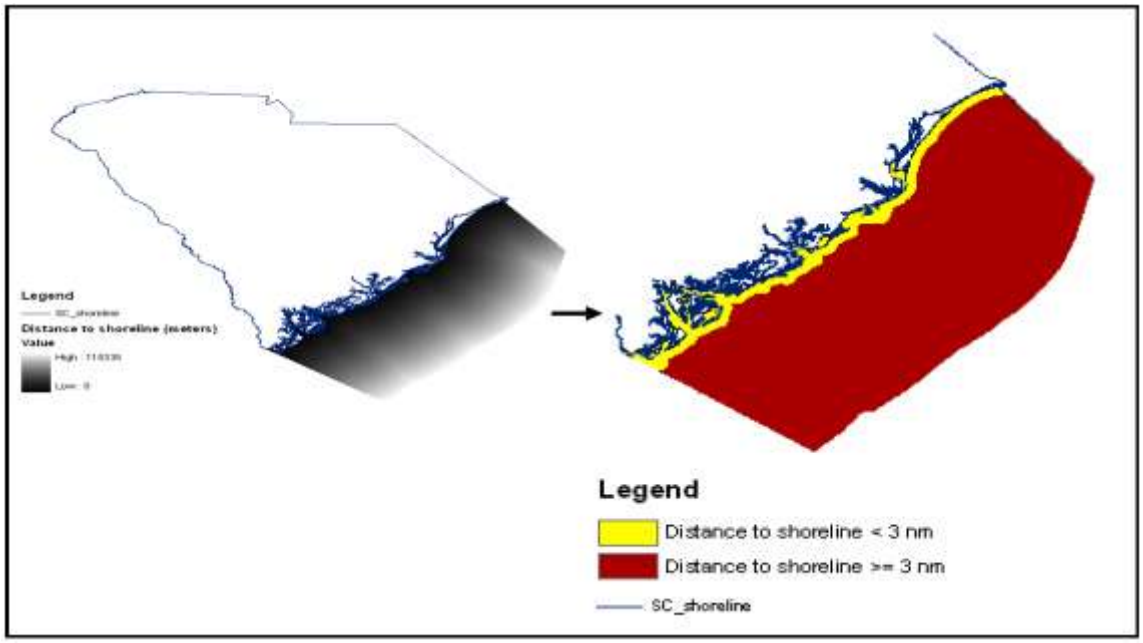

Figure 2.4 South Carolina distance to the shoreline (Jeffery et al., 2006).

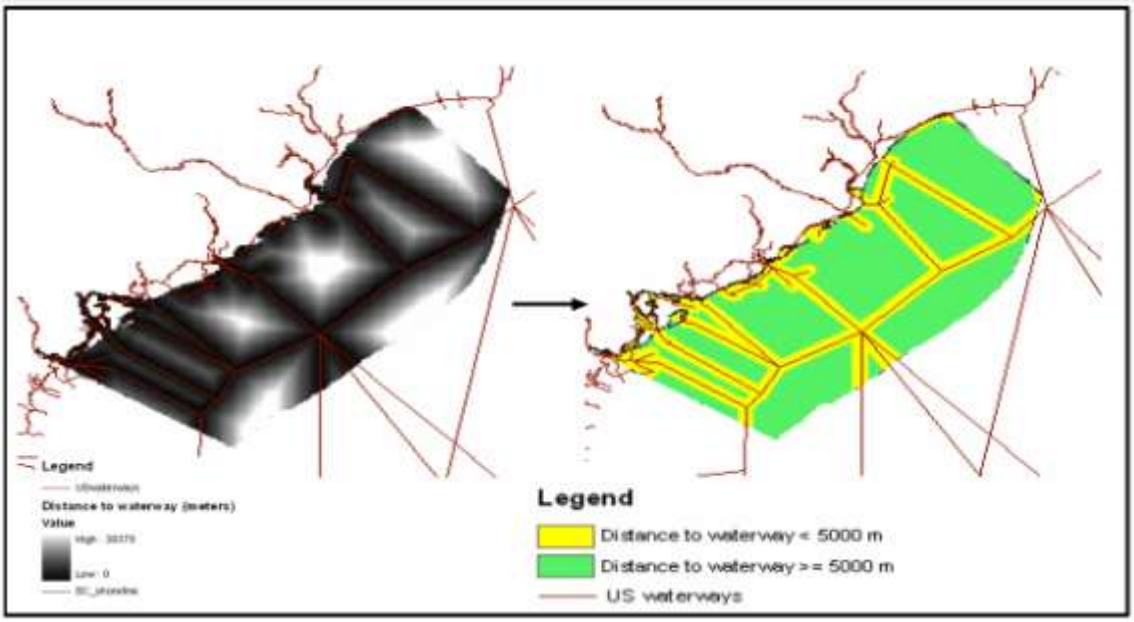

Figure 2.5 South Carolina distance to major motorways (Jeffery et al., 2006).

Finally, the distance to a navigable waterway plays an important role in site selection. Due to the safety requirements in the USA, a wind turbine farm should be installed at least 5 km

away from a waterway (Jeffery et al., 2006). Based on data from Navigation Data Center for South Carolina, the major navigable waterways are shown in Figure 2.5.

Based on information mentioned above, the suitable area near South Carolina seacoast was determined and is given by Figure 2.6.

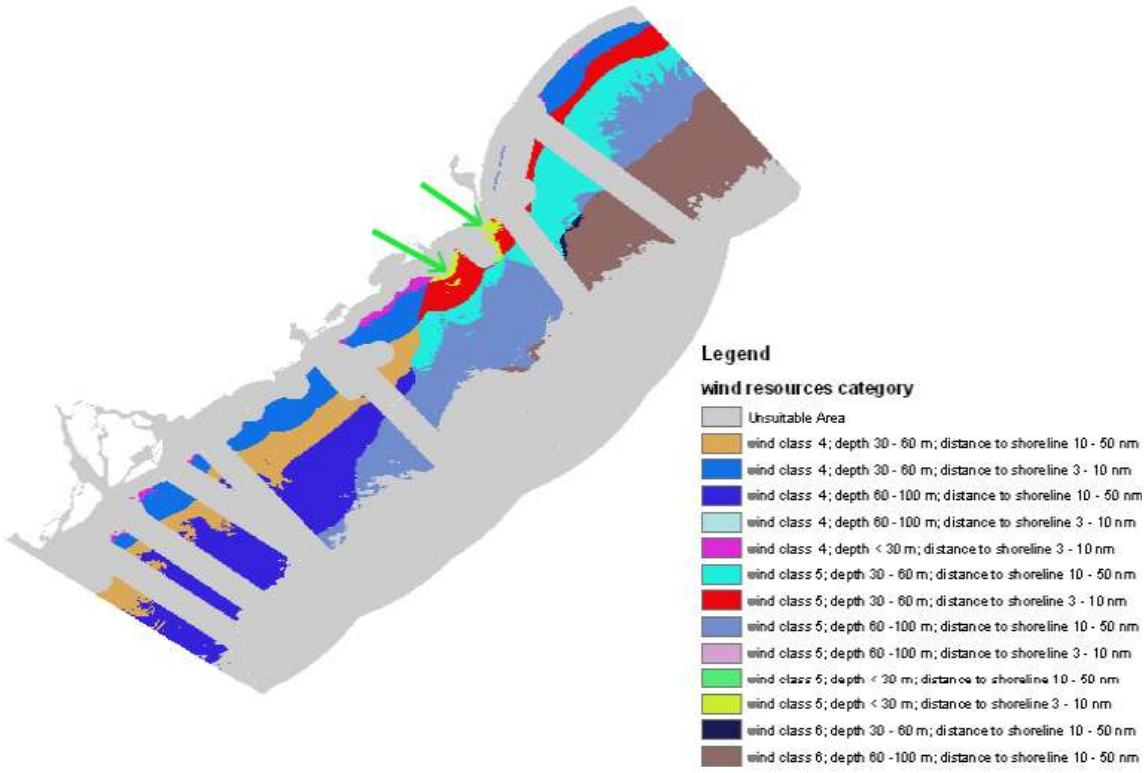

Figure 2.6 Suitable area for placing offshore wind farm (Jeffery et al., 2006).

From the figure, the most appropriate area has an average wind speed of about 8 m/s, i.e. Class 5, and water depth less than 30 m. This region is colored in light green and highlighted with an arrow for clarity.

Wave and wind data have been collected from National Data Buoy Center Platform 41004. These results are presented in Figures 2.7 – 2.9

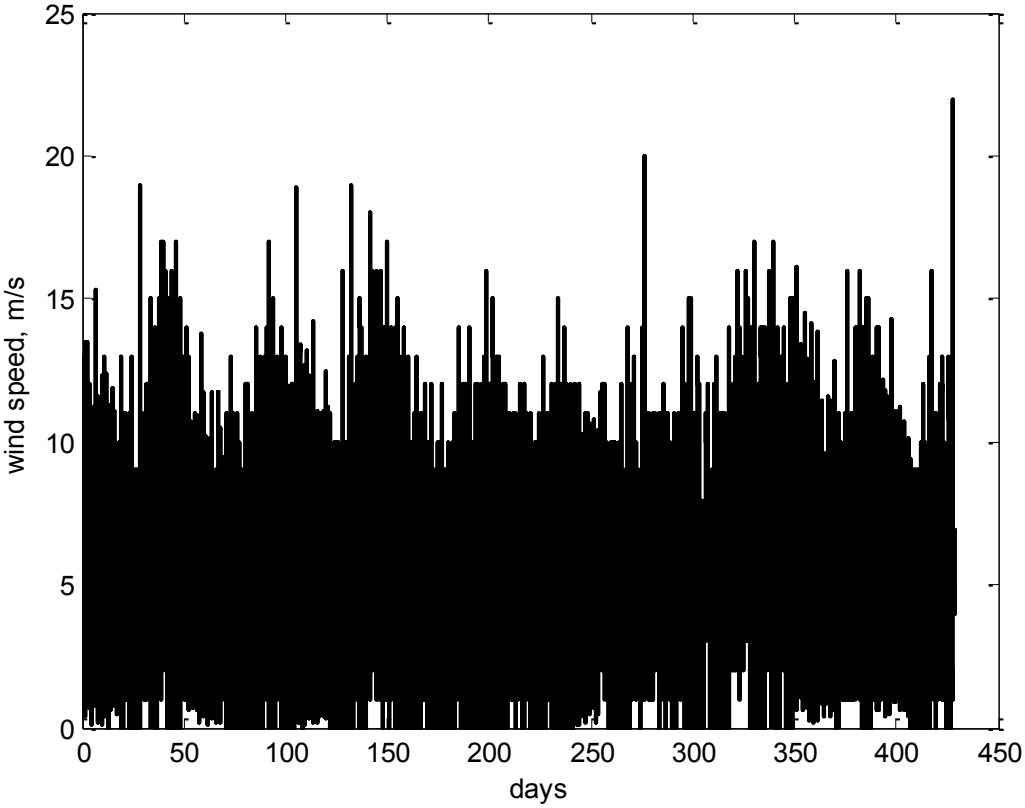

Figure 2.7 Wind speed time history at 10 m height above the surface (National Data Buoy Center Platform 41004)

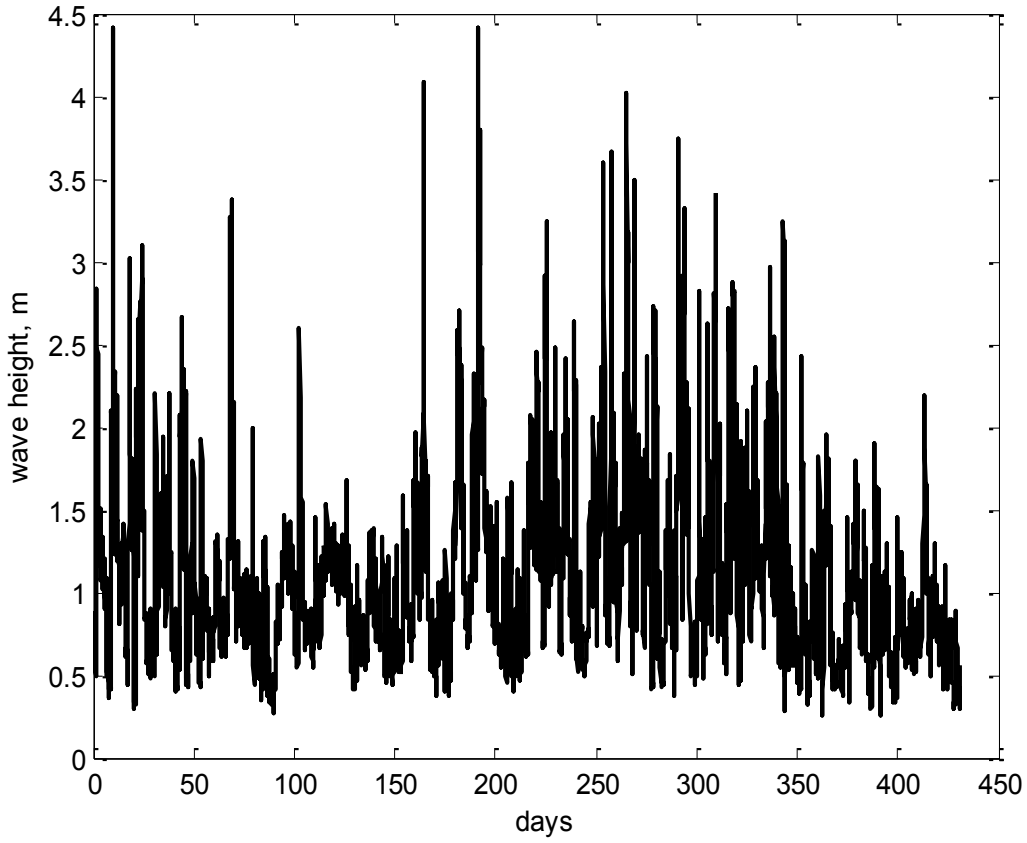

Figure 2.8 Ocean wave height time histories (National Data Buoy Center Platform 41004).

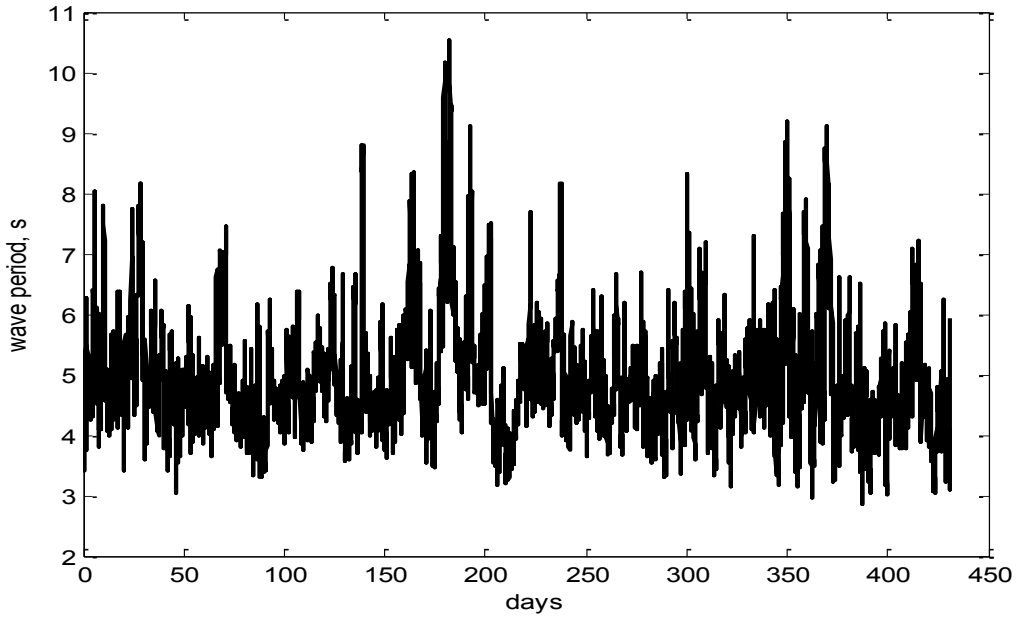

Figure 2.9 Ocean wave period time histories (National Data Buoy Center Platform 41004)

From the above time histories of given parameters, the average values of these parameters were calculated for one-year duration using the following equations.

The average wind speed was calculated with weight for its power content (Sathyajith, 2006) based on cubic dependency in Equation 1.2. The average value is given by Equation 2.1.

$$U_m = \left(\frac{1}{n} \sum_{i=1}^{n} U_i^3 \right)^{1/3} \tag{2.1}$$

In Equation 2.1, n is the number of wind data readings. In this study, n also denotes the total number of hours during which wind speed was measured, and U_i is a measured value of wind speed for each hour.

Wave height appears as the square power in Morison's equation (Morison et al., 1950), and wave length (i.e., distance between successive wave troughs) depends on the square of wave period.. Thus, the average values of these parameters were calculated by Equations 2.2 and 2.3.

$$H_{sm} = \left(\frac{1}{n} \sum_{i=1}^{n} H_{si}^2 \right)^{1/2} \tag{2.2}$$

$$T_{sm} = \left(\frac{1}{n} \sum_{i=1}^{n} T_{si}^2 \right)^{1/2} \tag{2.3}$$

Blade characteristic

In current work, blade characteristics were taken from publicly available airfoils characteristics for the NREL 5 MW baseline wind turbine (Jonkman, 2007). Blade consists of 5 airfoils developed by Delft University (DU) of Technology in Netherlands, and the NACA-64 airfoil. Each blade consists of 17 blade elements that are used to calculate total aerodynamic forces. Use of different airfoils for different position of blade elements explained by higher value of total lift force produced, comparing to that when single airfoil is used. Aerodynamic properties of these airfoil sections are gathered in Table 2.3.

Table 2.3 Characteristics of wind turbine blade elements (Jonkman, 2007)

Section #	Radial position,(m)	Twist angle,(deg)	Chord length,(m)	Airfoil used
1	2.8667	13.308	3.542	Cylinder1
2	5.6000	13.308	3.854	Cylinder1
3	8.3333	13.308	4.167	Cylinder2
4	11.7500	13.308	4.557	DU40
5	15.8500	11.480	4.652	DU35
6	19.9500	10.162	4.458	DU35
7	24.0500	9.011	4.249	DU30
8	28.1500	7.795	4.007	DU25
9	32.2500	6.544	3.748	DU25
10	36.3500	5.361	3.502	DU21
11	40.4500	4.188	3.256	DU21

12	44.55	3.125	3.01	NACA64
13	48.65	2.319	2.764	NACA64
14	52.75	1.526	2.518	NACA64
15	56.1667	0.863	2.313	NACA64
16	58.9	0.370	2.086	NACA64
17	61.6333	0.106	1.419	NACA64

The second column of the Table 2.3 denotes the distance along the blade-pitch axis from the center of the hub to the element cross section. Lift and drag coefficients for eight airfoil profiles were corrected from 2D airfoil data in order to account for the three-dimensional rotational behavior of the blades. For this purpose, an empirical model was used (Corrigan and Schillings, 1994). Corrected coefficients are illustrated in Figures 2.10 – 2.15.

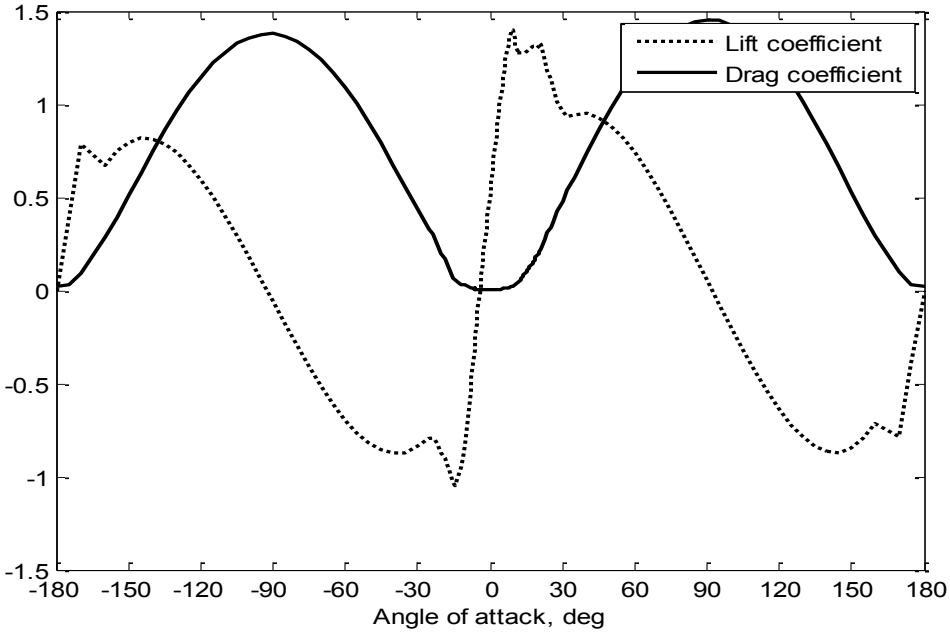

Figure 2.10 Corrected lift and drag coefficients of DU21 airfoil

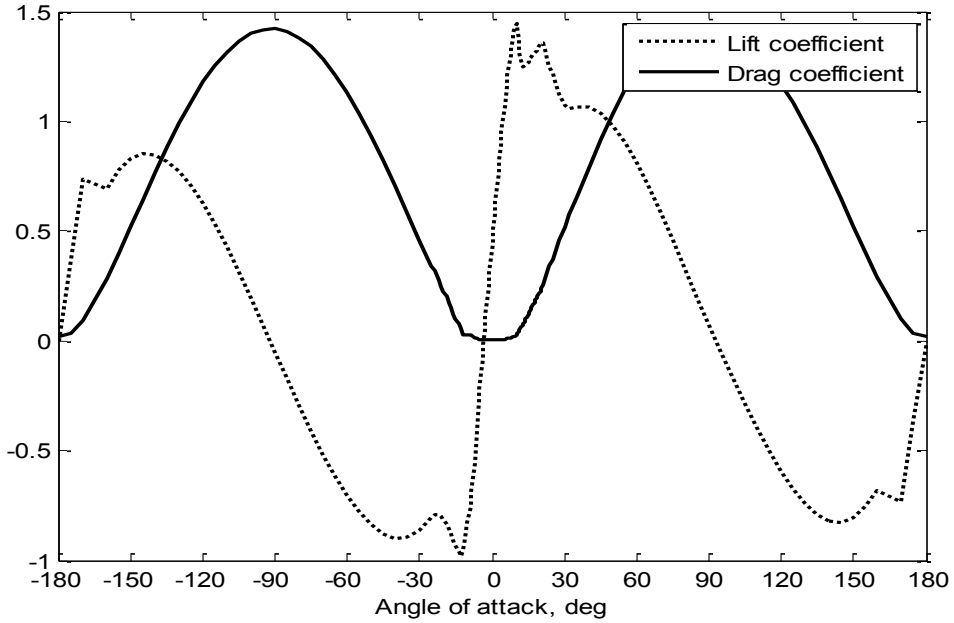

Figure 2.11 Corrected lift and drag coefficients of DU25 airfoil

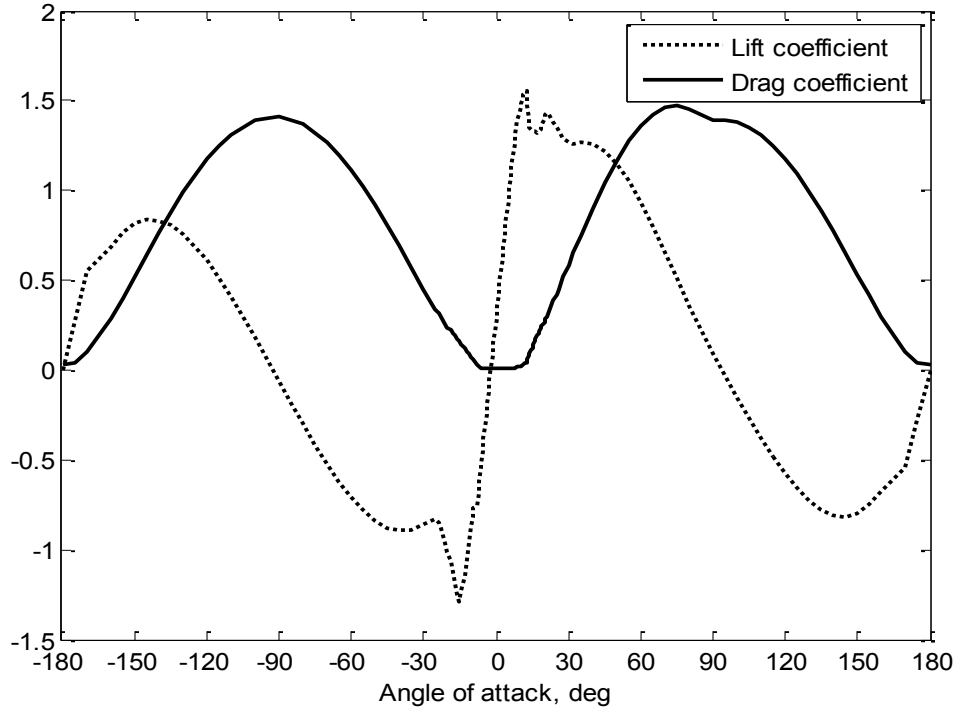

Figure 2.12 Corrected lift and drag coefficients of DU30 airfoil

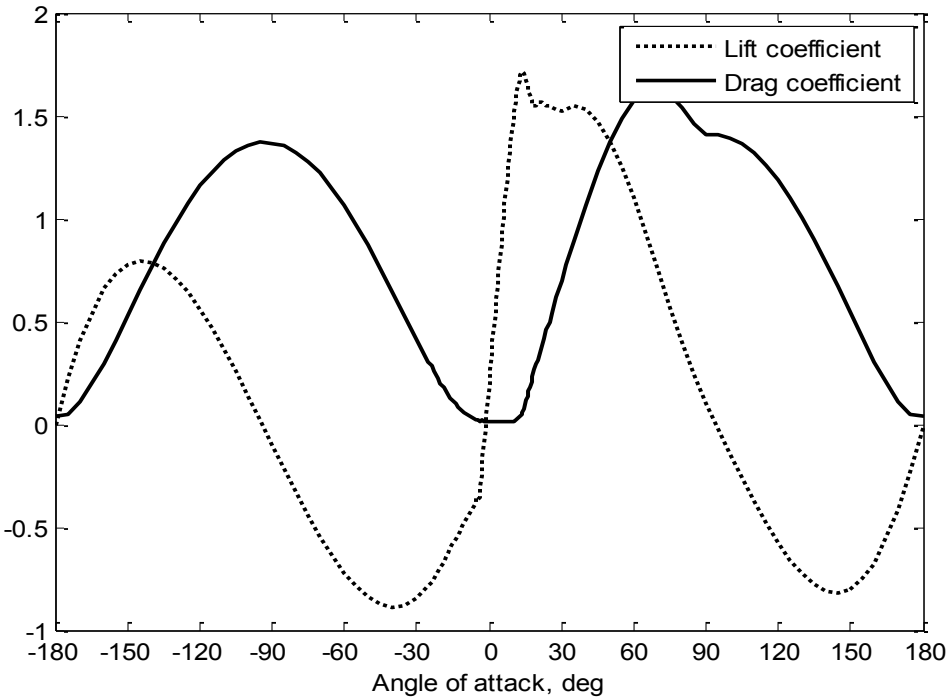

Figure 2.13 Corrected lift and drag coefficients of DU35 airfoil

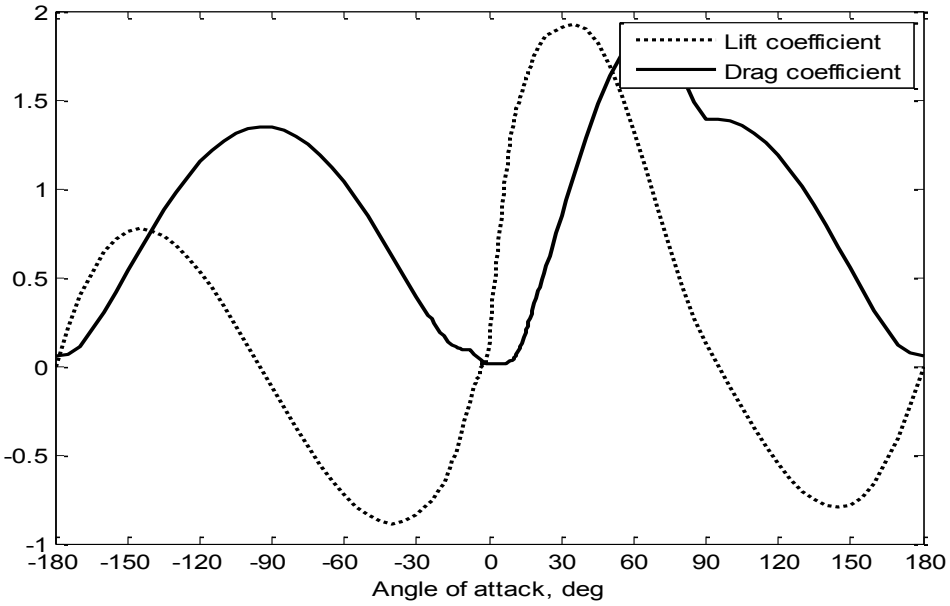

Figure 2.14 Corrected lift and drag coefficients of DU40 airfoil

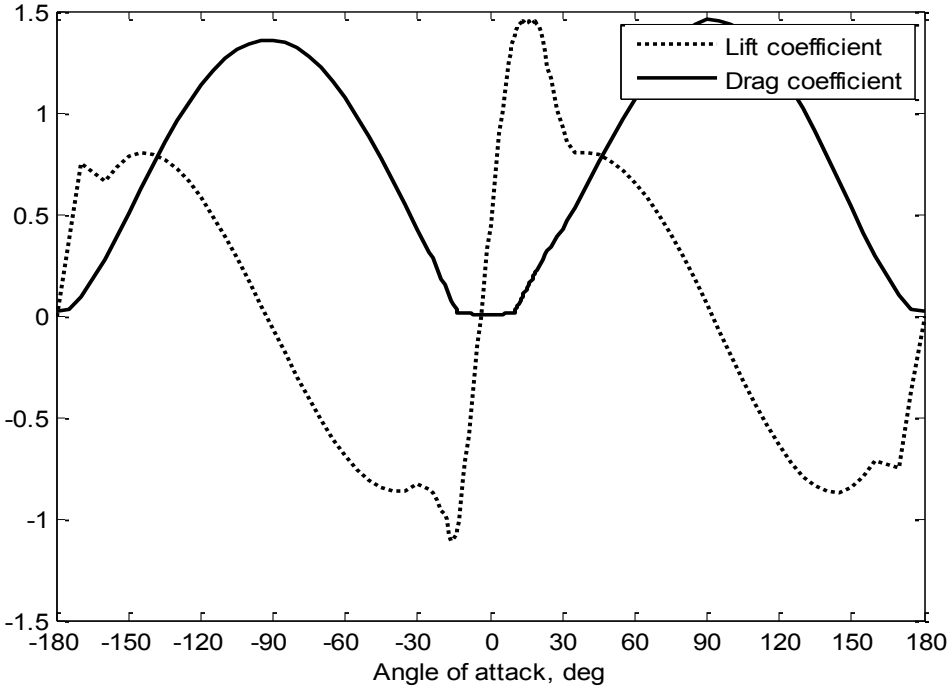

Figure 2.15 Corrected lift and drag coefficients of NACA64 airfoil

For an entire blade, the blade mass m_b was specified to be 17740 kg, similar to that used by Jonkman (2007). Also, it was assumed that there was no manufacturing difference in the mass of each of the three blades attached to the hub. The center of mass for each blade r_{CM}, is located a distance of 20.475 with respect to blade root along the span wise direction. This value is identical to that defined in NREL wind turbine (Jonkman, 2007).

Hub, nacelle and main bearing configuration

Like in the NREL 5MW baseline wind turbine, the hub mass m_h was specified as 56780 kg and the nacelle mass $m_N = 240000$ kg. The hub was located at a height of 90 m above mean sea level (MSL) and 5 m upwind of the tower centerline. The position of the main bearing and material properties of the bed plate, to which main bearing is mounted, are given in Table 2.4.

Table 2.4 A position of main bearing and material properties of bed plate (Jonkman, 2007).

Distance along shaft from ,main bearing to tower centerline	$l_{bx} = 3$ m
Vertical distance from the tower top to the main bearing, m	$l_{bz} = 1$ m
Young's modulus of the bed plate, Pa	2.1e11
Poison ration of the bed plate	0.33
Mass density of the bed plate, kg/m^3	7850

The bearing system consists of a main bearing, a so-called fixed bearing, and a floating bearing. A fixed bearing carries the radial and axial loads from the rotor while the floating bearing only handles a portion of the radial load. To date, the most beneficial solution has been proposed by Ionescu and Pontius (2009). It is an improved combination of double-row tapered roller bearings (TDI) and cylindrical roller bearings (CRB), instead of spherical roller bearings (SRB) for fixed and floating position, respectively. However, in the current project the actual shape of the bearing was not considered. Only the main bearing, which was considered rigidly mounted to the bedplate, was modeled due to the fact that it carries all axial force and most of the radial force acting on the bearing system.

The generator and gearbox are not modeled directly in this work as described previously. To represent these components, counter-torque from generator was prescribed instead such that a torque balance was present with the torque produced by the rotor. Additionally, to capture the

gravitational loads from gearbox and generator, distributed loads acting on the bedplate were applied.

Tower design

Reliable tower design for offshore conditions is very important due to the additional hydrodynamic loads originating from waves. In light of the previous comparison of different support structures in Chapter 1, the mono-pile foundation was chosen for the current project. For the offshore environment described earlier, this type of foundation will be the most beneficial economically and from structural point of view (Fichaux and Wilkes, 2009).

For the tower design, this study primarily uses data from RisØ DTU National Laboratory Generic 5 MW Offshore Wind Turbine (Krogh, 2004). Compared to the NREL tower (Jonkman, 2007), the RisØ tower (Krogh, 2004) is developed particularly for an offshore environment, while NREL tower (Jonkman, 2007) is based on onshore conditions. Having the same base diameter, the RisØ (Krogh, 2004) tower has a thicker wall and is more rigid as a result. For the current design, the overall height of the tower is 90 m above the mean sea level (MSL). The tower is extended to the sea floor, to which it is considered rigidly mounted. The base diameter D is specified to be 6 m, with wall thickness equal to 0.08 m. It is assumed that the radius and thickness of the tower are linearly tapered from the MSL to the top. As a result, the tower's top diameter was set to be 3.5 m. with thickness of 0.014 m. Effective mechanical steel properties of the tower were taken from RisØ project (Krogh, 2004) and are summarized in Table 2.5.

Table 2.5 Mechanical steel properties of the tower (Krogh, 2004)

Young's modulus of the steel, Pa	2.1e11
Poisson ratio	0.33
Mass density of the steel, kg/m^3	8750

Young's modulus was taken to be 210 GPa and steel density was set to be equal to 8500 kg/m^3. The value of density differs from that used in RisØ (Krogh, 2004). The typical value of 7850 kg/m^3 was increased in order to account for bolts, paint, welds and flanges that are not included in the tower thickness. The resulting overall tower mass is 1 066 ton.

Applied loads

Another important part in the design process is the description of wind turbine loading. The structural components of an offshore wind turbine are subjected to a variety of loads. It is not possible to define beforehand which of the loads are dominant. However, for analysis simplicity and clarity these loads can be divided into three groups: aerodynamic, mechanical and hydrodynamic. This is presented in Figure 2.16 and also in Table 1.1 of Chapter 1. Additionally, to show forces in the drive train that should be calculated, a free-body diagram of the off shore wind turbine is shown in Figure 2.17. In the main bearing base, applicable forces are reaction forces R_{bx} and R_{bz}, in axial and vertical direction respectively. These forces act through the bedplate within the nacelle onto which bearings and the tower are attached. Externally applied forces are aerodynamic forces from the rotor in axial direction F_N; wind drag forces on tower F_w ; ocean wave forces F_M and gravitational forces F_{bz} ,F_{top}, F_g and F_{tower} due to the weight of rotor, nacelle, generator and tower, respectively .

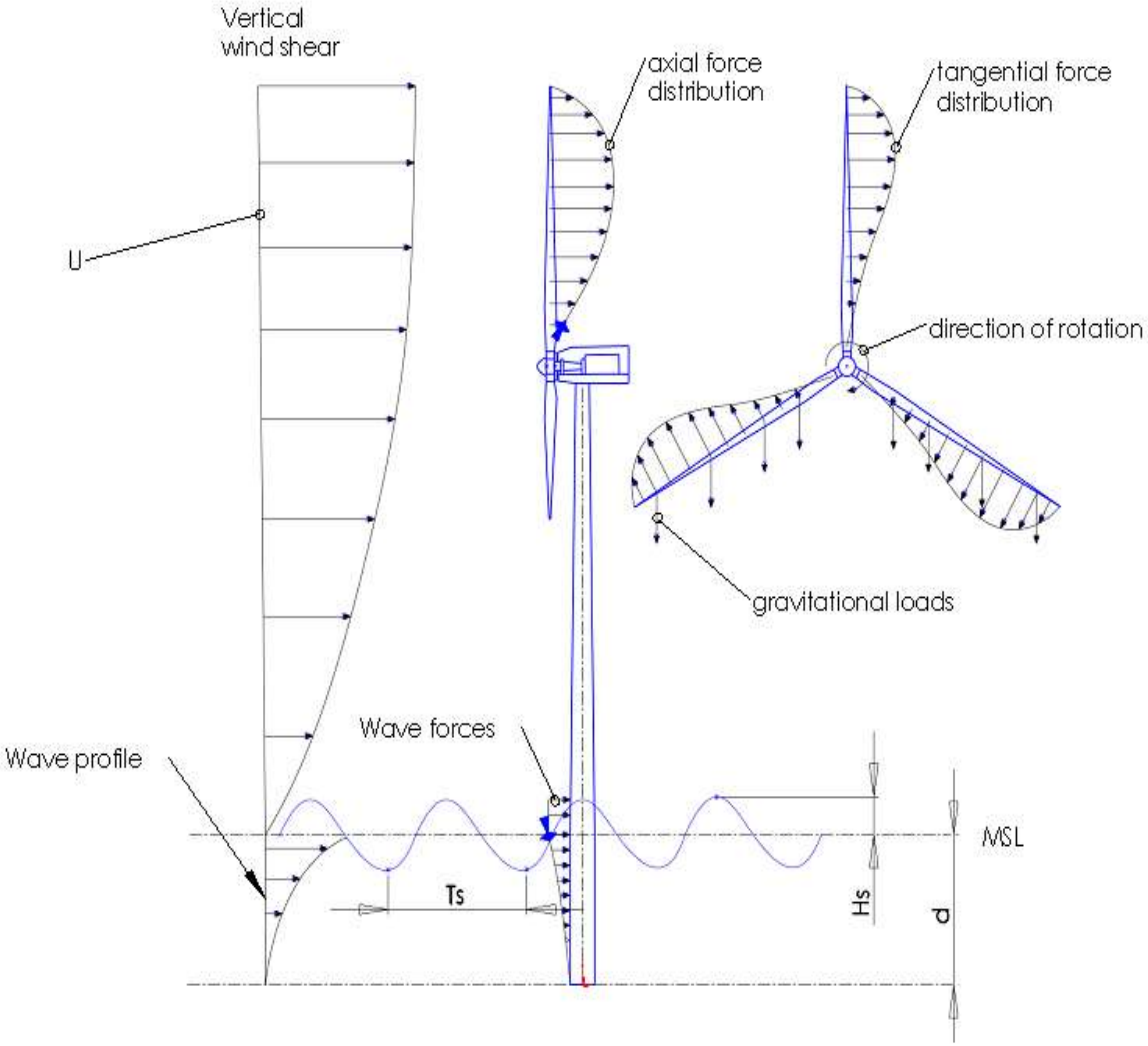

Figure 2.16 Loads on wind turbine

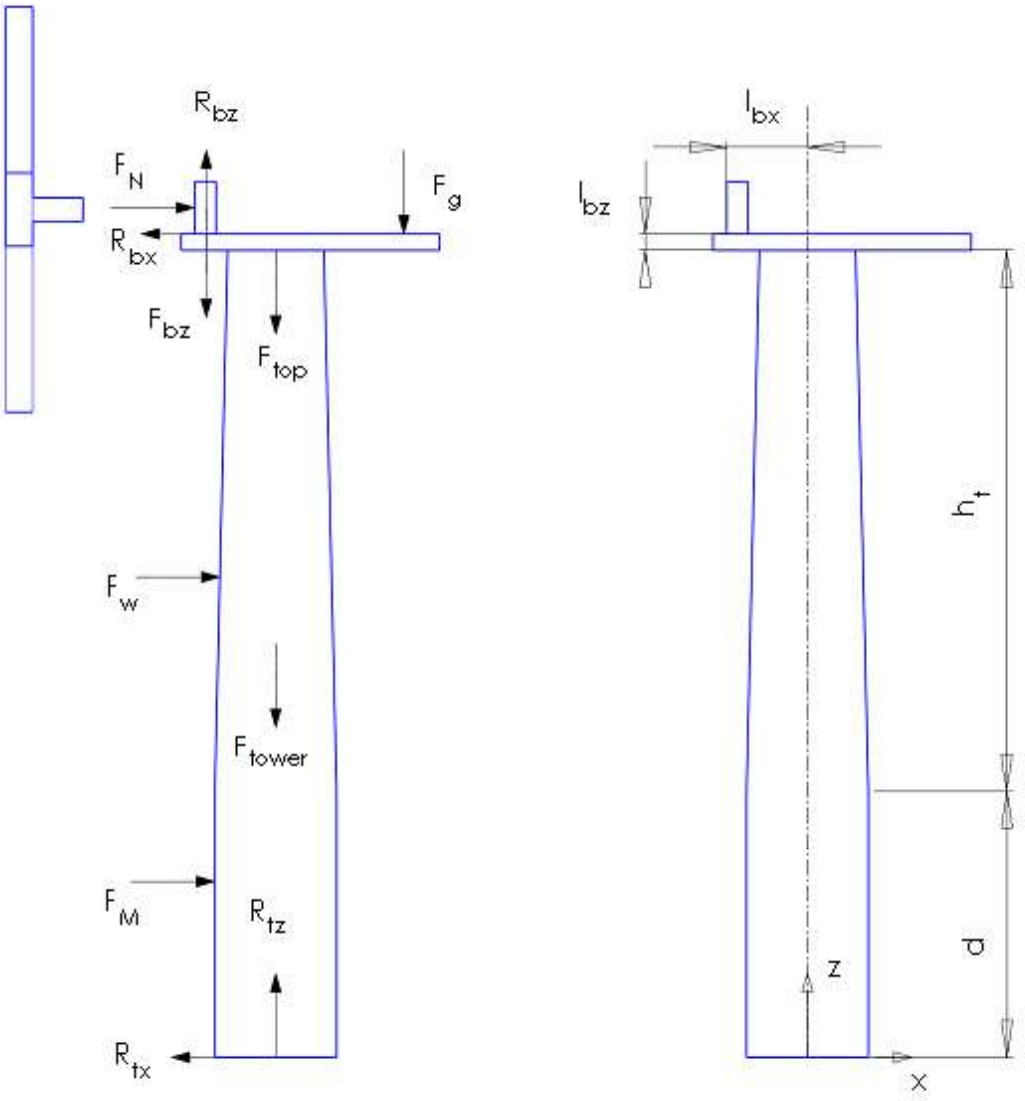

Figure 2.17 Free-body diagram of wind turbine

Aerodynamic loads are derived from the force of the wind and affect wind turbine system in two ways. The most important is the effect on the wind turbine rotor. Axial and tangential forces on the rotor blades originating from the wind are translated to the other components and, hence, determine their loading. In comparison to this load, the loading effect from downstream components is less important. The aerodynamic forces arise when the oncoming airflow is slowed

down by the rotor. The normal component is called thrust and results from the pressure difference over the rotor when flow passes the blade. On the other hand, the tangential component produces torque in the direction of rotation. As mentioned in Chapter 1, BEM theory together with axial momentum theory was applied to define aerodynamic forces acting on the rotor.

The first step of the algorithm based on BEM is to initialize a and a', which are the axial and tangential induction factors, respectively. Normally, a and a' are initially equal to zero. Next, the flow angle φ is computed by Equation 2.4.

$$\tan\varphi = \frac{(1-a)U}{(1+a')\Omega r} \tag{2.4}$$

The local angle of attack along the turbine blade is calculated by Equation 2.5.

$$\alpha = \varphi - \theta \tag{2.5}$$

Using the airfoil data, corrected lift and drag coefficients for a given α are obtained. The normal and tangential coefficients are then computed by Equations 2.6 and 2.7, respectively.

$$C_n = C_L\cos\varphi + C_D\sin\varphi \tag{2.6}$$

$$C_t = C_L\sin\varphi - C_D\cos\varphi \tag{2.7}$$

To check the error in the initial guesses of a and a', updated values of a and a' are calculated using Equations 2.8 and 2.9.

$$a = \frac{1}{\frac{4\cdot\sin^2\varphi F}{\sigma C_n}+1} \tag{2.8}$$

$$a' = \frac{1}{\frac{4\cdot\sin\varphi\cos\varphi F}{\sigma C_t}-1} \tag{2.9}$$

In Equation 2.9, F is the Prandtl tip loss factor that corrects for the assumption of an infinite number of blades. This is computed using Equation 2.10.

$$F = \frac{2}{\pi}\cos^{-1}\left(e^{\frac{B}{2}\frac{R-r}{r\cdot\sin\varphi}}\right) \tag{2.10}$$

If a and a' change more than a desired tolerance, the process is repeated with new value of axial and tangential induction factors.

If the desired tolerance is achieved, which is 1e-6, the local normal and tangential forces are computed using Equations 2.11 and 2.12, respectively.

$$dF_n = dF_L\cos\varphi + dF_D\sin\varphi \tag{2.11}$$

$$dF_t = dF_L\sin\varphi - dF_D\cos\varphi \tag{2.12}$$

By integrating local loads along the span wise direction and taking into account the number of other blades attached to a rotor, the total loads and moments can be defined. However, one has to be careful when the axial induction factor becomes larger than 0.2, the so-called critical axial induction factor a_c, as axial momentum theory breaks down. To correlate the axial induction factor, Glauret (1935) proposed using the correction given by Equation 2.13 and described in Chapter 1.

$$a = \frac{1}{2}\left[2 + K(1-2a_c) - \sqrt{(K(1-2a_c)+2)^2 + 4(K\,a_c^2 - 1)}\right] \tag{2.13}$$

where,

$$K = \frac{4F\sin^2\varphi}{\sigma C_n} \tag{2.14}$$

Equation (2.13) should replace equation (2.8) in order to compute induced velocity correctly.

The algorithm above was implemented using the MATLAB simulation tool. The associated algorithm can be found in many books and articles and the actual code of this study is presented in the Appendix (Hau, 2006; Hansen, 2008; Emrah and Nadir, 2009).

Wind drag forces acting on the tower are also taken into account. These forces are a function of the wind velocity, wind direction relative to the turbine blade, and areas and shapes of the structural elements. Det Norske Veritas (1978) recommends Equation 2.15 to compute induced wind forces on the wind turbine tower.

$$F_w = \frac{\rho}{2} U^2(t,z) C A \sin\chi \tag{2.15}$$

In Equation 2.15, $U(t,z)$ is the wind velocity, which is a function of time, elevation and gust factor. It is given by Equation 2.16 where U_{ref} usually denotes wind velocity at 10 m height above water surface. Additionally, no wind gusts were considered for current analysis, so $\alpha' = 1$.

.

$$U(t,z) = \alpha' U_{ref} \left(\frac{z}{z_{ref}} \right)^{\alpha_{shear}} \tag{2.16}$$

Additionally, the drag coefficient C along the height of the tower, which strongly depends on Reynolds number, is assumed to be constant. The value of drag coefficient of 0.5 was taken from table (Myers, 1969), based on the mean value of outer diameter of the tower and the mean wind speed along tower height. In an actual wind turbine, the drag coefficient will be influenced bythe interaction between the rotor and tower. Besides, such interference affects a wind turbine rotor as well. For the rotor position in the current project, this influence is at a minimum because the rotor is mounted in the traditional upwind configuration.

Unlike aerodynamic loads and their difficulties in calculation, mechanical loads are relatively simple to calculate. In large offshore wind turbines, these types of loads are associated with the weight of structural components and as result are steady for all tome period.

Gyroscopic forces can be significant additional forces. However, these forces arise when the turbine direction is changed and were not considered.

Finally, the hydrodynamic forces originating from the wave action was considered. Total wave forces, which include drag and inertia components, can be represented by Morison's equation (Morison et al., 1950).

$$dF_M = \frac{1}{2} C_D \rho D u |u| + C_M \rho \frac{\pi}{4} D^2 \frac{\partial u}{\partial t} \tag{2.18}$$

A fixed-bottom type of wind turbine tower with a constant submerged diameter make Morison's equation (Morison et al., 1950) the most suitable representation of wave action on structural components for current wind turbine model. Coefficients C_D and C_M in Equation 2.18 may vary over the height of the pile due to the variation in Reynolds number. Determining the value of these coefficients is not an easy task for engineers. To date, several approaches exist to make it possible (Stewart, 2008). However, for current analysis these coefficients were taken constant as suggested in literature (Ecen, 2003; Dean and Dalrymple, 2006). Velocity and acceleration of water particle induced by ocean wave are periodic functions as defined by Equations 1.8 – 1.12. Their horizontal components may be positive or negative direction along X-axis (Zhang et al., 2006). Therefore, force F_M calculated by Equation (2.18) also may be positive or negative.

To determine the total force on the vertical wind turbine tower, Equation (2.18) should be integrated over the submerged length of the pile and velocity and acceleration term should be

extended using linear wave theory, as described in Chapter 1. The result of such manipulation is given by Equation 2.19.

$$F_M = C_D D\, n\, E \cos\left(k\,x - f\,t\right)\left|\cos\left(k\,x - f\,t\right)\right| + C_M \pi D E \frac{D}{H_s} \tanh\left(kd\right)\sin\left(k\,x - f\,t\right) \tag{2.19}$$

In Equation 2.19, the wave energy per unit surface area is

$$E = \frac{1}{8}\rho g H_s \tag{2.20}$$

and the ratio of group velocity to speed of the wave is

$$n = \frac{1}{2}\left(1 + \frac{2k\,d}{\sinh(2k\,d)}\right) \tag{2.21}$$

In the Equation 2.19, the location of the pile x , can be taken to be zero for convenience.

In order to calculate unknown parameters such as wave number and wave frequency, the following technique was used (Hsu, 1984). From the available offshore site data described previously, wave height and wave period were extracted. Shallow water wave length, when $\tanh(k \cdot d) = 1$, was computed first by Equation 2.22.

$$L_0 = \frac{g T_s^2}{2\pi} \tag{2.22}$$

Then, the ratio of water depth to shallow water wave length d/L_0 was computed, and using Wiegel's table (Wiegel, 1964), the ratio of water depth to wave length d/L was calculated. According to the determined wave length, wave frequency was calculated.

Computational method

For the finite element model of the wind turbine tower, the multiphysics modeling and simulation software COMSOL (Version 4.1, COMSOL, Inc., Burlington, MA, USA) was used. The computational domain and the corresponding force boundary conditions are shown in Figure 2.18.

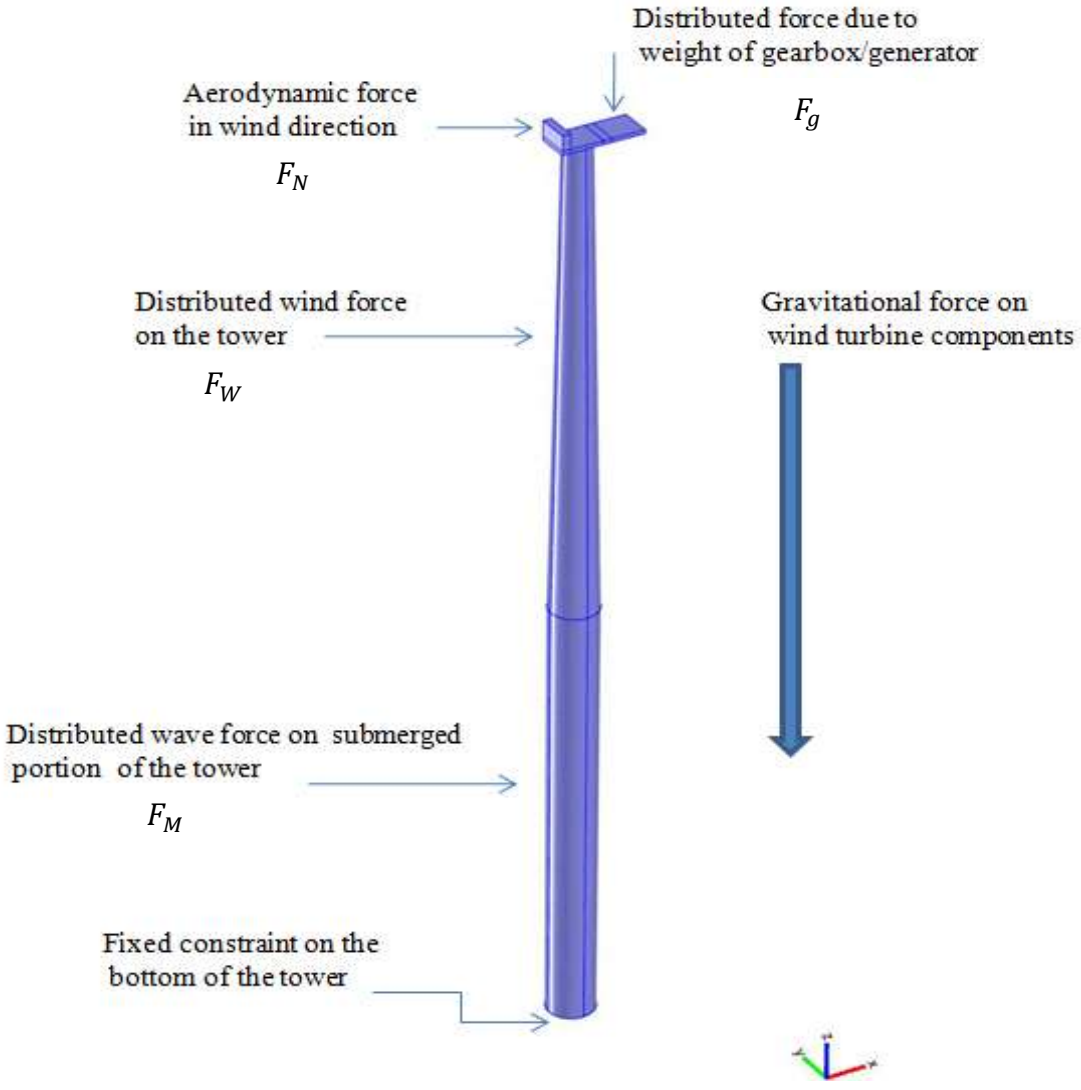

Figure 2.18 Computational domain and force boundary conditions.

In Figure 2.18, the positive x-direction was assigned to be the wind direction. The y-axis was normal to the wind direction and tower centerline, and the z-axis was along the tower

centerline. To represent structural components more accurately and with a more economical mesh, the computational domain was divided into two sub-domains. One includes only the wind turbine tower and the other includes the bed plate together with the main bearing, which are shown in Figure 1.3. To account for a fixed tower bottom, a fixed constraint was defined that restricted movement in all direction on the bottom surface of the tower. To represent excluded structural components such as the gearbox and generator, distributed forces due to the weights of these components were applied on the bed plate boundary. Also, gravitational forces were applied to all structural elements as volumetric forces. To model the wind and wave actions on the wind turbine structural components, additional external forces were applied as boundary conditions. On the face surface of the main bearing, the periodic aerodynamic thrust force was applied, based on results obtained from the MATLAB simulation tool for an isolated rotor. Wind drag force on the tower was defined as a steady force varying with tower height and was applied along tower height above the ocean surface at MSL. Finally, the wave action on the submerged portion of the tower was applied based on Morison's equation (Morison et al., 1950) which is given by Equation 2.18.

As described so far, the computational model contains two domains. The domain including the tower has a very thin geometry in one direction. Large differences in the respective scales of the wall thickness and height of the tower may cause the mesh generator to fail in creating the mesh. Also, since the COMSOL free meshing by default creates elements that are as isotropic as possible (non-flat), a large number of elements will be created in a thin layer.

The way of getting an economical mesh for the current problem is to create a surface mesh on a boundary and then sweep it from a source boundary to a destination boundary. For current model, the source boundary was bottom surface of the tower and destination boundary was tower top surface. Sweeping has the advantage of controlling the number of element layers and their distribution. Another advantage is that the number of mesh elements often is decreased.

The domain that includes the bed plate and main bearing was meshed using a free tetrahedral mesh. The final mesh is shown in Figure 2.19.

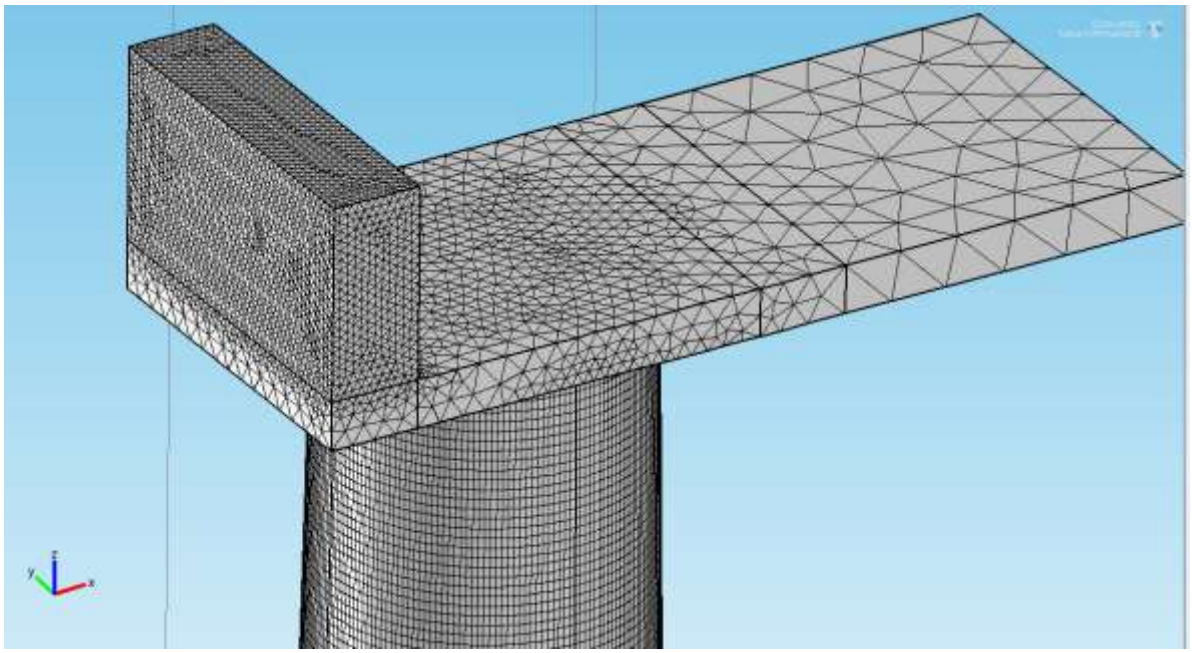

Figure 2.19 Mesh for wind turbine physical model

To find the solution of time-dependent problem, also called the dynamic or unsteady problem, the generalized-α method (Chung and Hulbert, 1993) was used for wind turbine response. This is the default transient solver in COMSOL for most unsteady physical phenomena. It has properties similar to a second-order backward differentiation method (BDF), but is more accurate due to its ability to control the degree of damping of high frequencies, by use of a parameter called alpha in the literature. The implementation of the generalized alpha in COMSOL detects which variables are first-order in time and which variables is second-order in time and applies the correct formulas to the variables.

Verification of time step size and mesh size.

Time step and mesh element sizes were evaluated to ensure that assigned values provided results that had acceptable precision. Important dynamic behavior of the system is not represented if a large time step or coarse mesh are used. Also, an overly fine mesh or very small time step can require excessive computational power or time expenditures. Additionally, another important consideration was the simulated elapsed time. The basis for results of this work was steady periodic behavior of the system. Return maps were constructed to assess when steady periodic behavior occurred. This method illustrates the dynamic behavior of any dependent variable by plotting its value at a current time step versus its value at a previous one. A single closed loop denotes simple periodic behavior while numerous closed loops indicate more complex periodic behavior. Loops that do not close denote chaotic behavior.

The mesh of the finite element model should be sufficiently fine to allow accurate resolution of generated forces. The main goal of this work was to assess forces generated in the base of the main bearing where it is mounted to the bed plate. Hence, the mesh was verified by calculating the forces R_{bx} and R_{bz}. Forces in the Y direction were excluded because of an absence of net lateral forces. Three different meshes were assessed. These are specified in Table 2.6 and were referred to as coarse, normal and fine.

Table 2.6 Different meshes used in assessing sensitivity of R_{bx} and R_{bz} to mesh size.

Mesh	Minimum element size, (m)	Maximum element size, (m)	Average element quality
Coarse	0.1	1	0.53
Normal	0.01	0.1	0.75
Fine	0.005	0.05	0.88

Each mesh generated is characterized by the minimum and maximum mesh element size and by average mesh element quality. The last one varies between 0 and 1, where 0 denotes a very poor mesh element quality and 1 denotes a very good quality of mesh element.

Reactions forces in the main bearing base in the axial direction R_{bx} are calculated with the different meshes of Table 2.6 are shown in Figure 2.20.

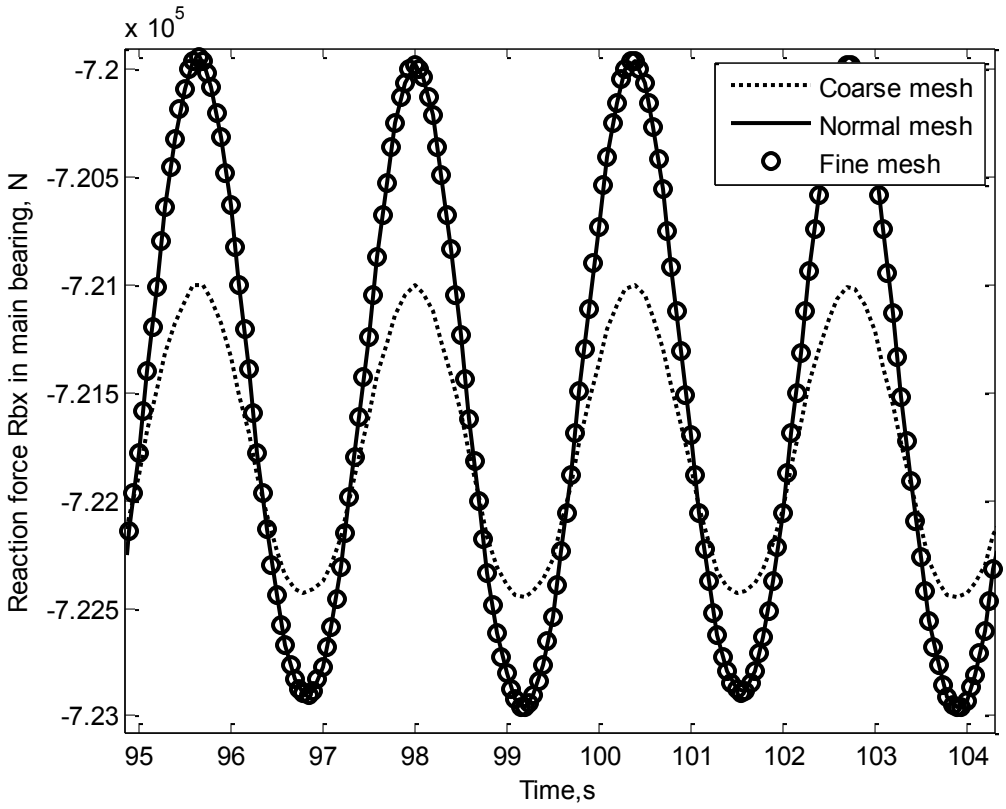

Figure 2.20 Force in main bearing base, R_{bx}, under operational conditions of U=12 m/s, Hs=1 m, Ts=5 s, for different meshes.

One can easily conclude from Figure 2.20 that curves for R_{bx} using a normal and fine mesh almost coincide, i.e., the error between results for these two meshes is approximately 1% or less.

Reaction forces R_{bz} in vertical direction using different meshes are shown in Figure 2.21

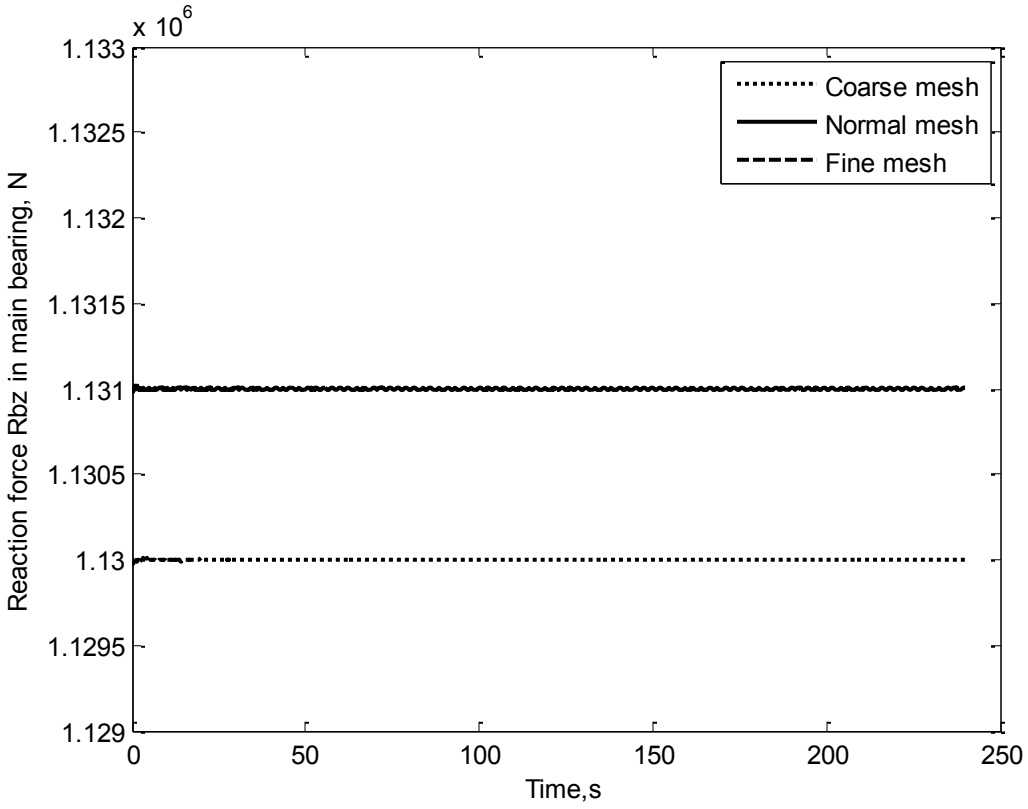

Figure 2.21 Force in main bearing base R_{bz} under operational conditions of U=12m/s, Hs=1m, Ts=5s, for different meshes.

As can be seen in Figure 2.21, R_{bz} is a straight line. This can be easily explained by the steady gravitational forces due to the rotor mass with very small mass acceleration/ deceleration in this direction, comparing to gravitational forces. Additionally, as for R_{bx} , the error between results for R_{bz} using normal and fine meshes is approximately 1% or less.

The time step size was also verified by calculating the same forces R_{bx} and R_{bz} in main bearing. Three different time step sizes were investigated. Results are shown in Figure 2.22 and 2.23.

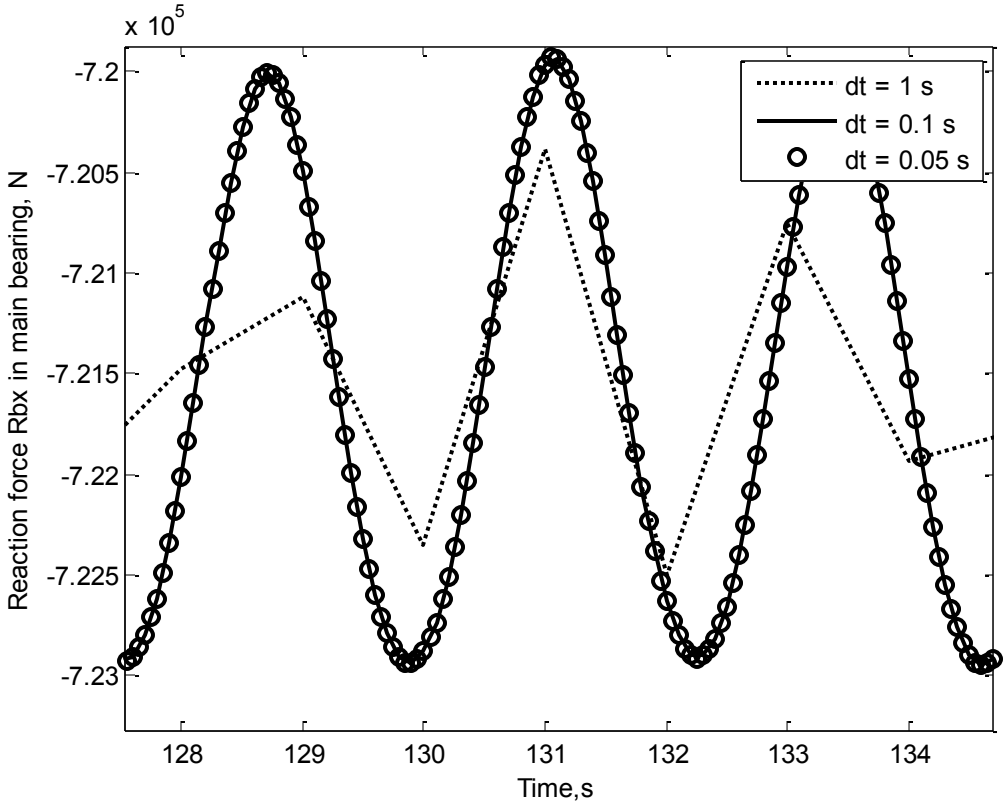

Figure 2.22 Force in main bearing base, R_{bx}, under operational conditions of U=12 m/s, Hs=1 m, Ts=5 s, for different time step sizes.

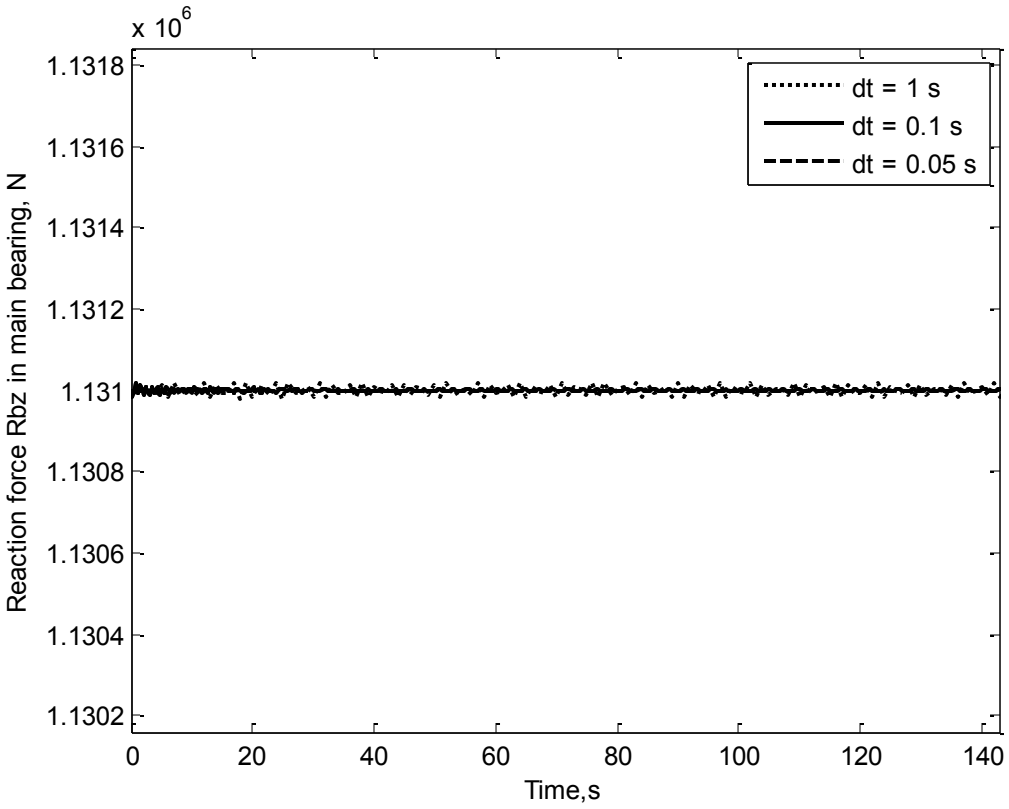

Figure 2.23 Force in main bearing base R_{bz} under operational conditions of U=12m/s, Hs=1m, Ts=5s, for different time step sizes.

To show the small influence from

One can easily conclude that curves for R_{bx} and R_{bz} using a 0.1s and 0.01s time step sizes almost coincide, i.e., the error between results for these two meshes is approximately 1% or less.

As a result of the verification analysis, normal mesh with 0.1s time step size were chosen for the developed finite element model. To show that steady periodic behavior was reached, in Figure 2.24, the return map for axial force R_{bx} was plotted for the last 10 cycles. The closed loop, which can be easily seen, denotes steady periodic behavior.

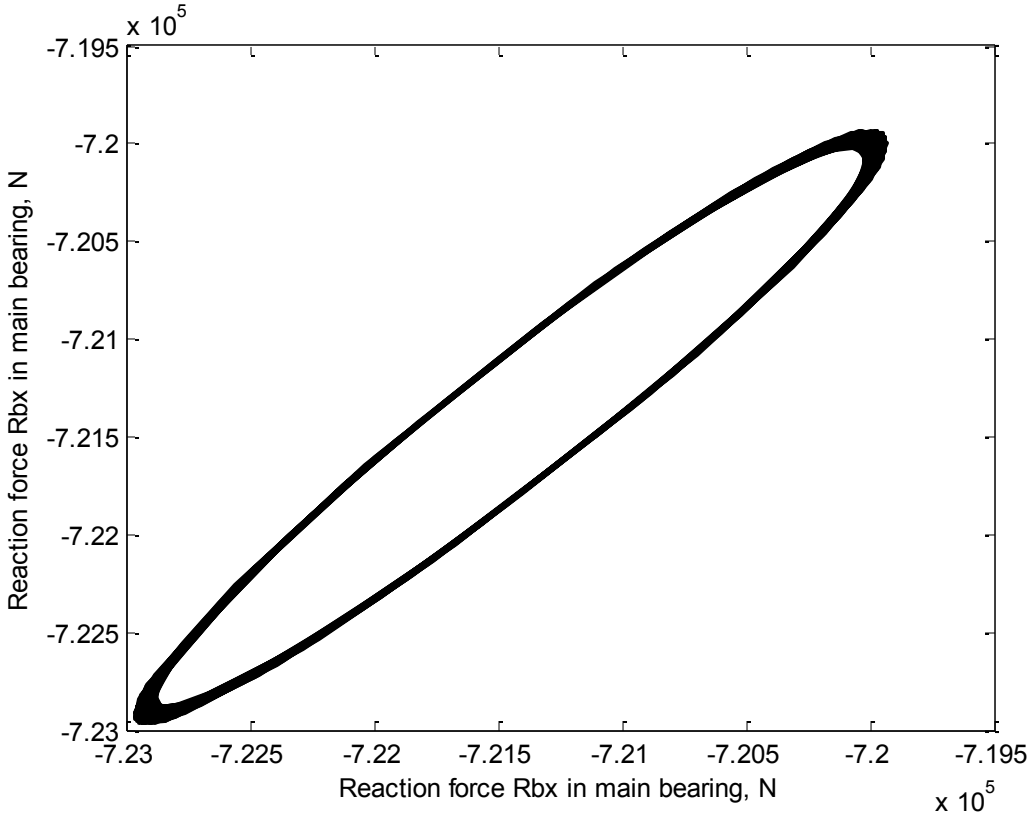

Figure 2.24 Return map for last 10 cycles of the force in main bearing base, R_{bx}, under operational conditions of U=12 m/s, Hs=1 m, Ts=5 s with normal mesh and time step size of 0.1 s

Validation of simulation tool

As mentioned previously, aerodynamic forces originating from the rotating rotor were calculated separately and were applied as boundary conditions in a detailed computational model of other components. To calculate these forces, the MATLAB simulation tool was used. Based on the algorithm described in Chapter 2, a numerical code was developed which is given in the Appendix .

To validate the model, publicly available data from NREL 5MW baseline wind turbine was used (Jonkman, 2007). Rotational speed of the rotor and aerodynamic properties of wind turbine blades were identical to those used by Jonkman (2007) to ensure comparability of obtained results. However, a smaller wind speed range was considered to compare two models than that used by Jonkman (2007). The region beyond rated wind speed, which is approximately between 4 m/s and 11 m/s, was considered to compare developed numerical code. The reason for this is that above rated wind speed, rotor power is held constant by regulating to a fixed rotational speed with active blade-pitch control in the NREL project (Jonkman, 2007). However, this effect could not be modeled in the current work because no control mechanisms are considered. As a result, above the rated behavior of rotor torque, rotor power and especially rotor thrust could not be modeled correctly. Based on such restrictions, results from steady-state simulation are presented in Figure 2.25, Figure 2.26 and Figure 2.27.

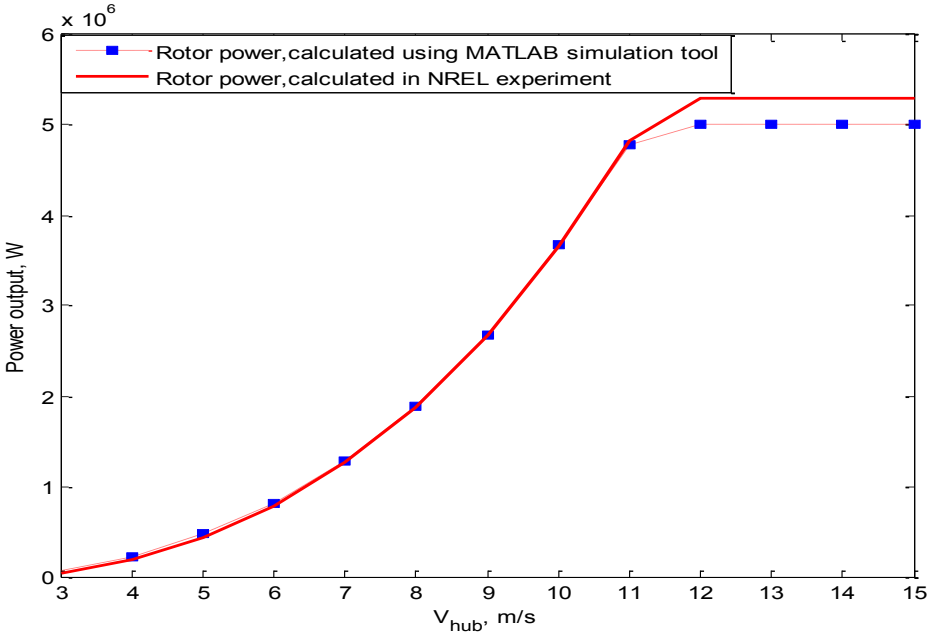

Figure 2.25 Rotor power as a function of wind speed calculated by MATLAB simulation tool and in the NREL project.

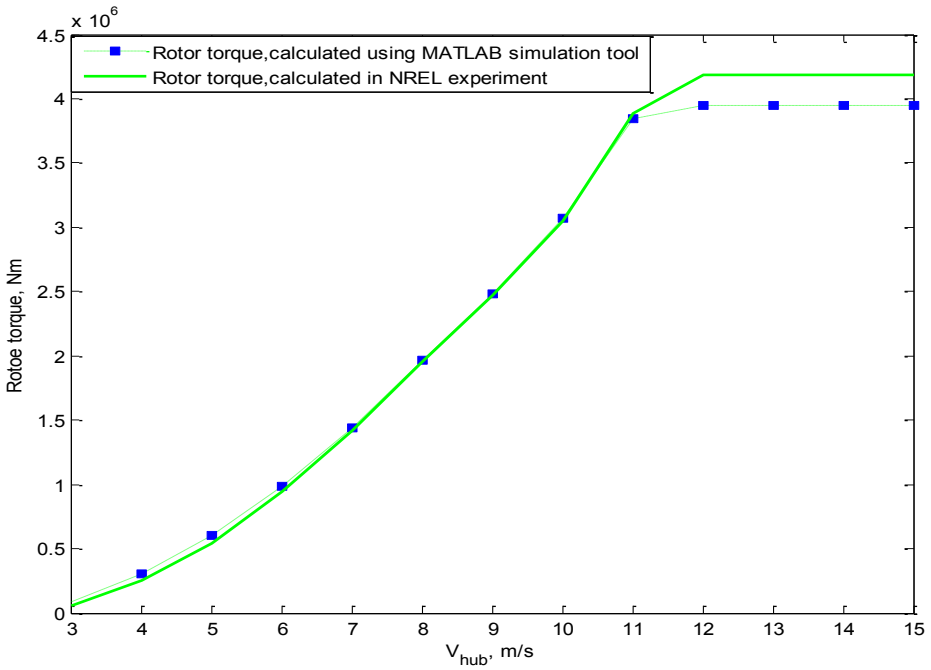

Figure 2.26 Rotor torque as a function of wind speed calculated by MATLAB simulation tool and in the NREL project.

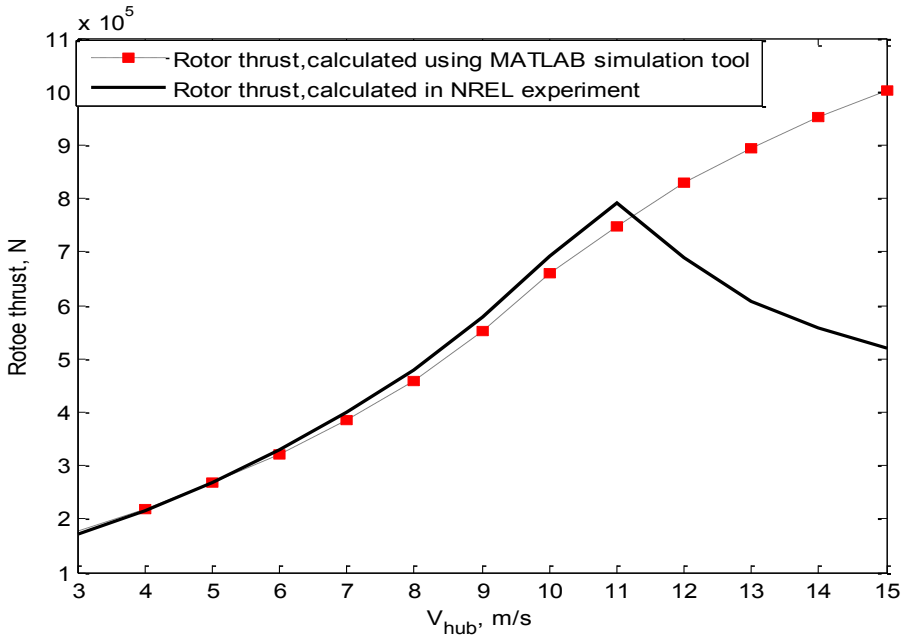

Figure 2.27 Rotor thrust as a function of wind speed calculated by MATLAB simulation tool and in the NREL project.

Above figures clearly show that developed numerical code is in a good agreement with NREL data for wind speed ranged between cut-in, i.e. 4m/s, and 11 m/s, which is rated wind speed. Also, as was mentioned previously, above the rated the thrust force is keep increasing, which is naturally should be unless any control mechanism used. The power output and rotor torque, calculated by use of MATLAB simulation tool, above the 11 m/s keep constant value, which was set manually, otherwise, they will increase as well.

Validation of calculated forces

Additionally to simulation code validation, described so far, validation of reaction forces in the main bearing R_{bx} and R_{bz} has to be performed. To check the feasibility of obtained reaction forces, steady state simulation was run and force equilibrium was checked. In Table 2.7 externally applied thrust force F_N and reaction force in the main bearing in axial direction R_{bx} are shown.

Table 2.7 Force balance in the main bearing between externally applied thrust force F_N and reaction force in axial direction R_{bx}

Aerodynamic thrust force F_N	Reaction force in the main bearing in axial direction R_{bx}
2.8258e2, kN	2.8258e2, kN

One can easily conclude from Table that externally applied thrust force F_N is equal to reaction force in the main bearing in axial direction R_{bx}. Which means that in x-direction, the force balance is kept.

To check force balance in vertical direction, which is along the tower centerline, the reaction force in the main bearing in vertical direction R_{bz} was compared to gravitational force

due to weight of the rotor. Results are given in Table, which shows that in vertical direction the force balance is kept as well.

CHAPTER THREE

RESULTS AND DISCUSSION

The main objective of this study was to model the dynamic forces that are present on drive train components for an off-shore wind turbine. Based on project objective and prospective of future research, results obtained from finite element model for drive train components are presented in time domain. To investigate the influence of a wind speed, ocean wave height and ocean wave period on reaction forces in the main bearing system, results also presented in frequency domain. To convert time domain response to frequency domain response discrete Fourier transform (DFT) was used (Briggs and Henson, 1995). Investigating parameters were divided into three groups and presented in Table 3.1

Table 3.1 Investigating parameters of the wind and ocean.

Parameters / Load case	Wind speed, U, m/s	Rotational speed Ω, rpm	Wave height H_s, m	Wave period T_s, s
Group I:Effect of wind speed, U.	4	7.183	1	5
	7	9.67	1	5
	12	12.1	1	5
Group II: Effect of wave height, H_s	7	9.67	0	5
	7	9.67	1	5
	7	9.67	4	5
Group III: Effect of wave	7	9.67	1	2
	7	9.67	1	5

period, T_S	7	9.67	1	10

To establish a baseline against which comparisons will be made, results for wind turbines operating under nominal conditions is analyzed first. These nominal conditions, described in Chapter 2, include a wind speed of 7 m/s, ocean wave height of 1 m and ocean wave period of 5 s. To understand the behavior of externally applied force, thrust force F_N and ocean wave force F_M are shown in Figure 3.1 through Figure 3.4 in time and frequency domain.

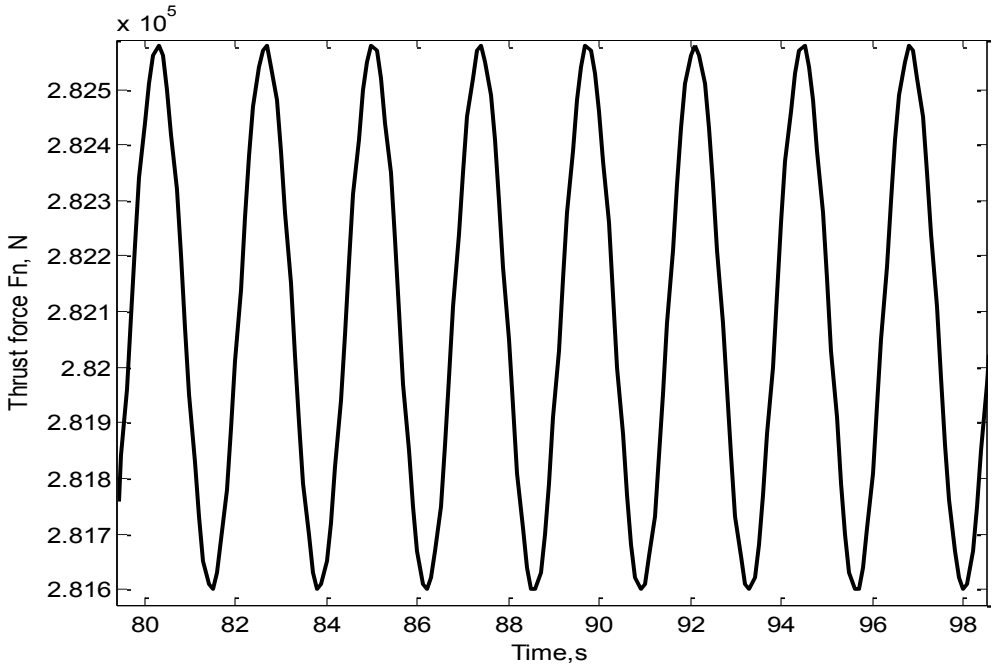

Figure 3.1 Thrust force, F_N, for wind speed of U=7 m/s in time domain

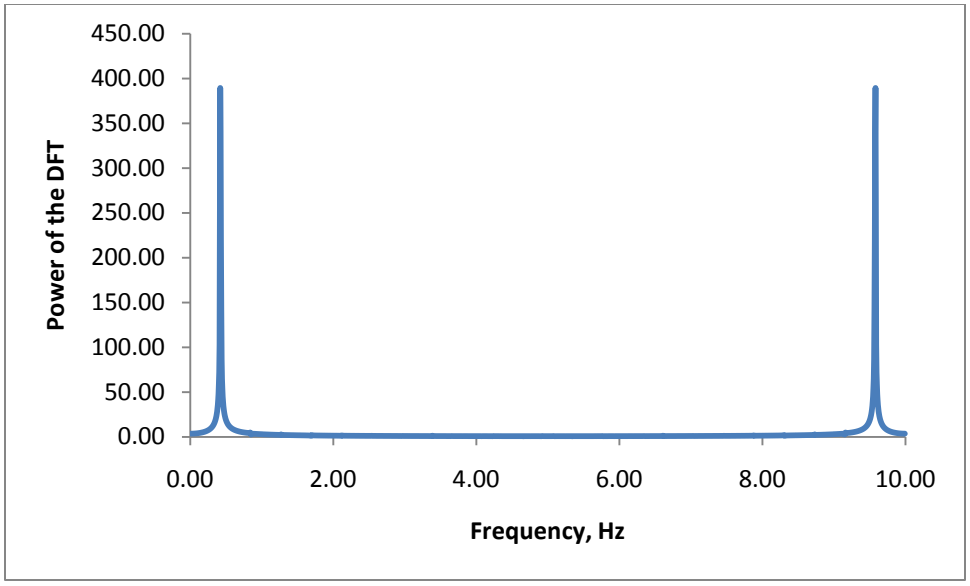

Figure 3.2 Thrust force, F_N, for wind speed of U=7 m/s in frequency domain with f_s = 10 Hz

Figure 3.1 clearly shows that the amplitude of the thrust force F_N is approximately an order of 1e3 while the mean value is an order of 1e5.

In Figure 3.2 the first half of the frequency range (from 0 to the Nyquist frequency f_s /2) is sufficient to identify the component frequencies in the data, since the second half is just a reflection of the first half. Therefore, in further discussions only the first half of the frequency range will be considered. From Figure 3.2, the frequency of thrust force of wind speed of 7 m/s can easily be seen and it is approximately 0.4 Hz.

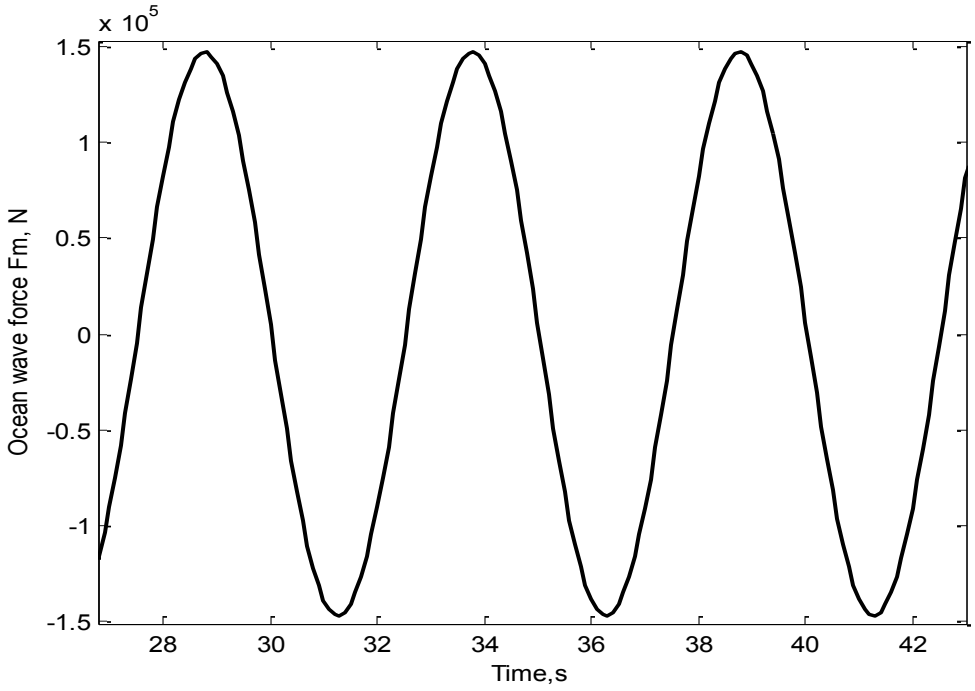

Figure 3.3 Ocean wave force, F_M, for H_s = 1 m and T_s = 5 s, in time domain.

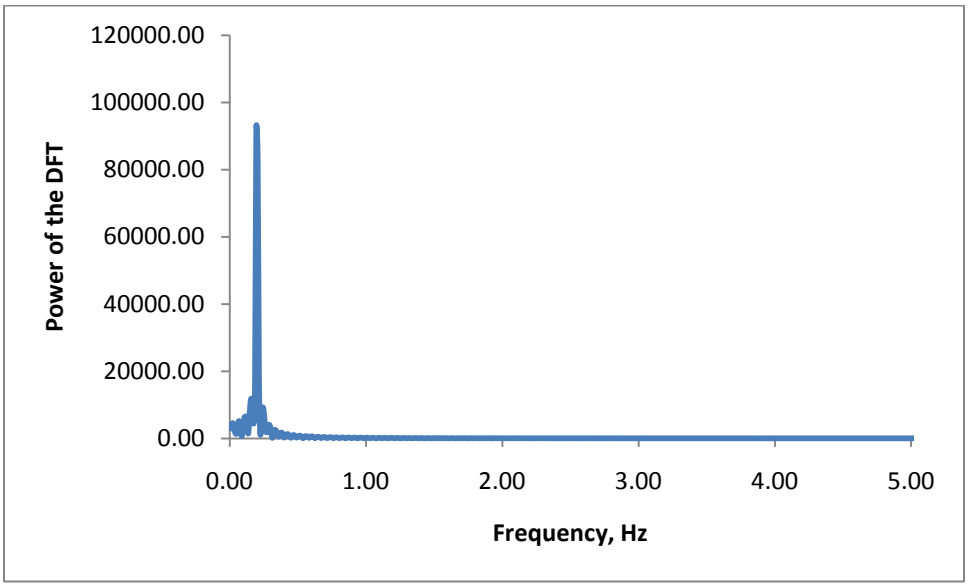

Figure 3.4 Ocean wave force, F_M, for H_s = 1 m and T_s = 5 s, in frequency domain

In Figure 3.3 the ocean wave force F_M is not sinusoidal function, based on Equation 2.19, but periodic, with period equal to ocean wave period. Figure 3.4 shows that for H_s = 1 m and T_s = 5 s the ocean wave force occurs at frequency of approximately 0.2 Hz.

Additionally, to time domain simulation, the eigenfrequency analysis was performed to calculate the lowest natural frequency of physical model, described in Chapter 2 and shown in Figure 2.18. Based on this analysis the lowest natural frequency was 1.1 Hz, which corresponds to the fore-aft oscillation of the tower. The lowest natural frequency lies above the frequencies of thrust force and ocean wave force excitation, discussed so far.

In Figure 3.5 and Figure 3.6 the reaction force R_{bx} in the main bearing in axial direction is presented in time domain.

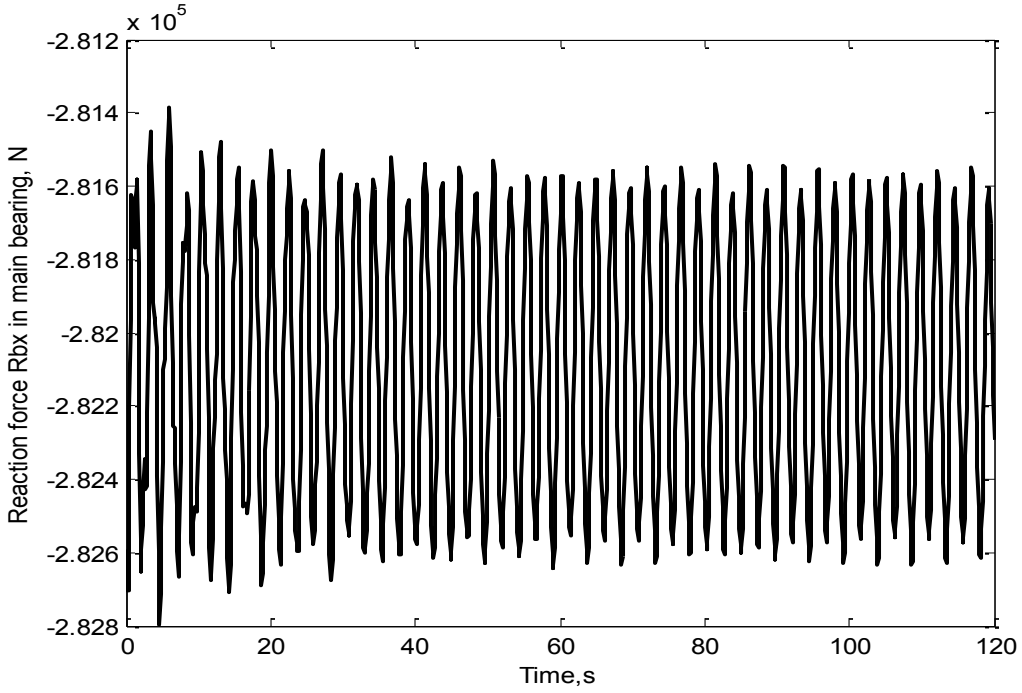

Figure 3.5 Force in the main bearing base, R_{bx} in axial direction, under operational conditions of U=7 m/s, H_s = 1 m, T_s= 5 s, in time domain.

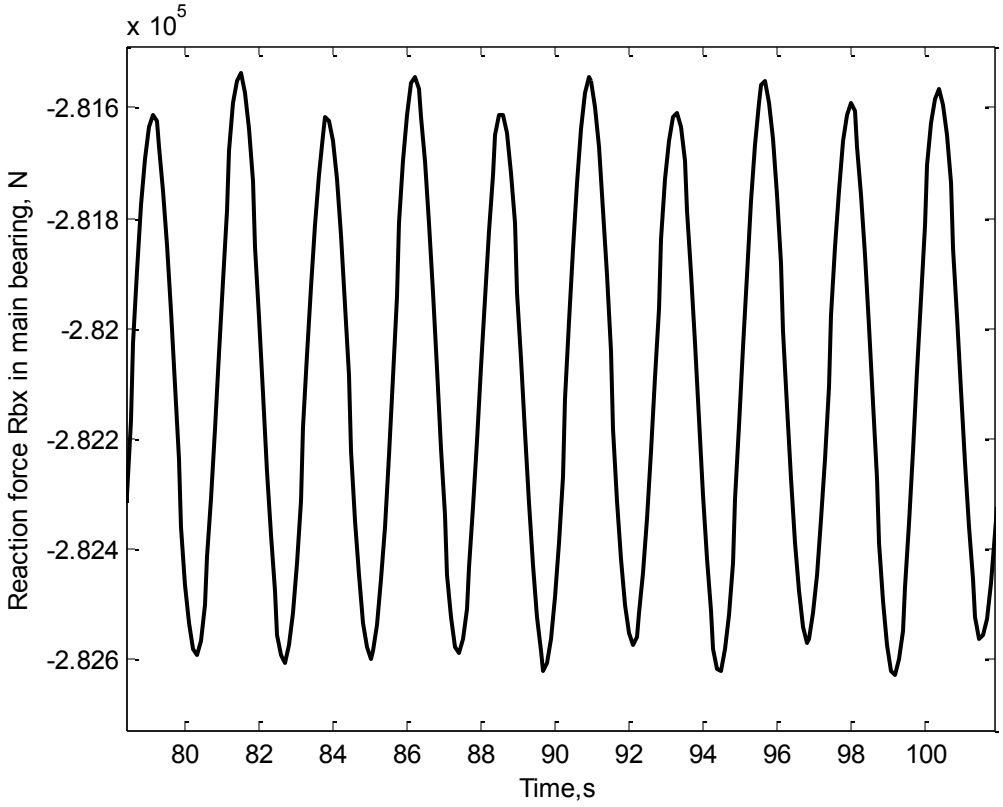

Figure 3.6 Force in the main bearing base, R_{bx} in axial direction, under operational conditions of U=7 m/s, H_s = 1 m, T_s= 5 s in time domain.

Figures 3.5 and 3.6 show that the amplitude and mean value of the reaction force R_{bx} in the main bearing are determined by the thrust force F_N generated on the rotor. Tower for-aft oscillation, due to the combined ocean wave and wind drag force, brings very small change in amplitude. To show it, the reaction force in the main bearing R_{bx} in axial direction is shown in Figure 3.7 in frequency domain.

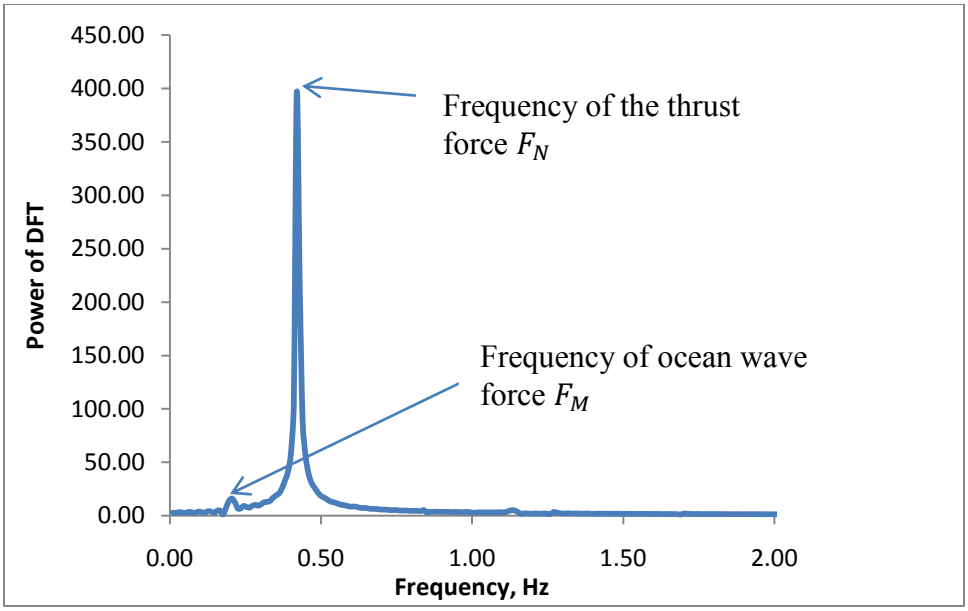

Figure 3.7 Force in the main bearing base, R_{bx} in axial direction, under operational conditions of U=7 m/s, H_s = 1 m, T_s= 5 s in frequency domain.

As can be seen from Figure 3.7, the dominant is the thrust force frequency,while the power of ocean wave force is very small.

The temporal response of Figure 3.5 was used to construct a return map for the force R_{bx} in the main bearing. The result is given in Figure 3.8. A closed loop for the last 10 cycles indicated that steady periodic behavior is reached.

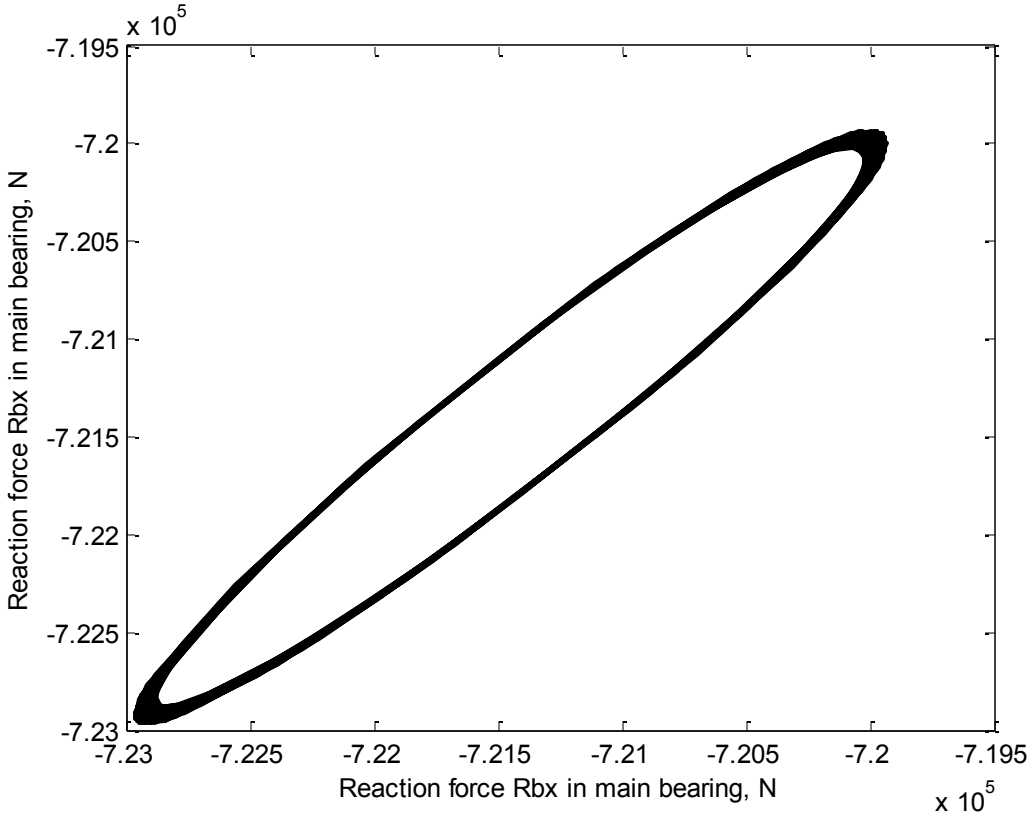

Figure 3.8 Return map for last 10 cycles of the force in the main bearing base, R_{bx}, under operational conditions of U= 7 m/s, H_s = 1 m, T_s= 5 s..

In the vertical direction, which is along the tower centerline, the reaction force R_{bz} are due mostly to constant gravitational forces as indicated in Figure 3.9. These are forces due to the weight of the rotor and the main bearing. Additionally, the acceleration of the main bearing in the axial direction (i.e., direction of wind) due to the combined ocean wave and wind action can cause temporal variations in R_{bz} due to tower deflection. However, the magnitude of these temporal forces is very small that is shown in Figure 3.10

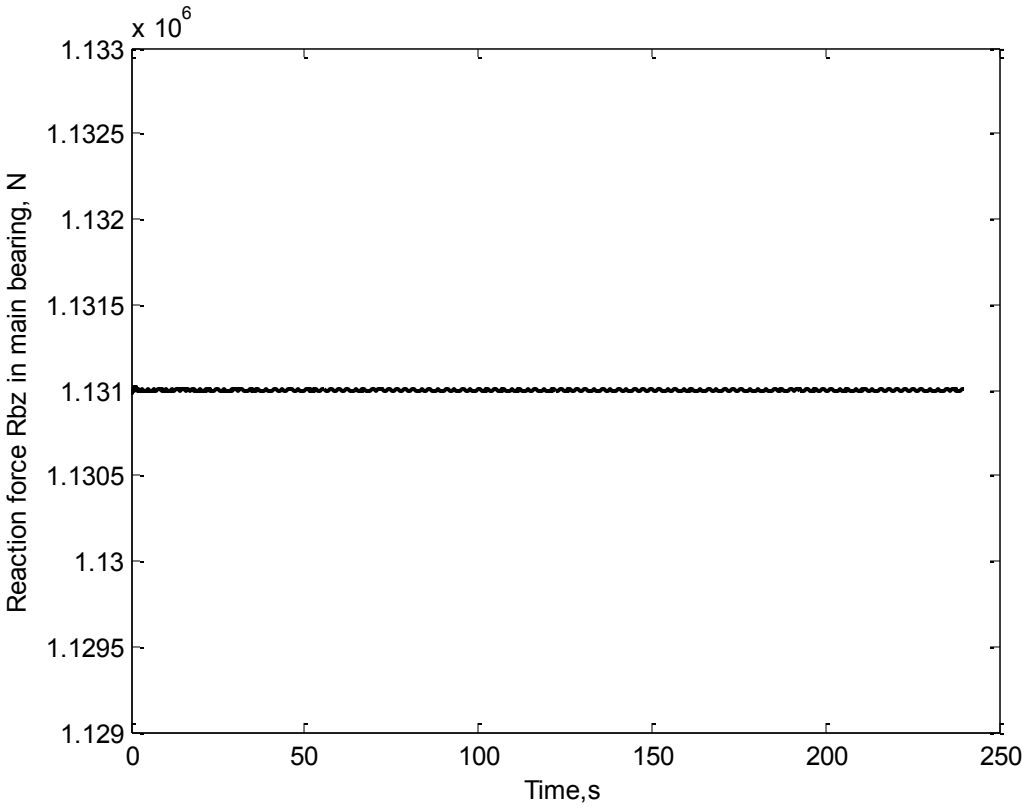

Figure 3.9 Force in the main bearing base R_{bz} , under operational conditions of U=7 m/s, H_s = 1 m, T_s= 5 s.

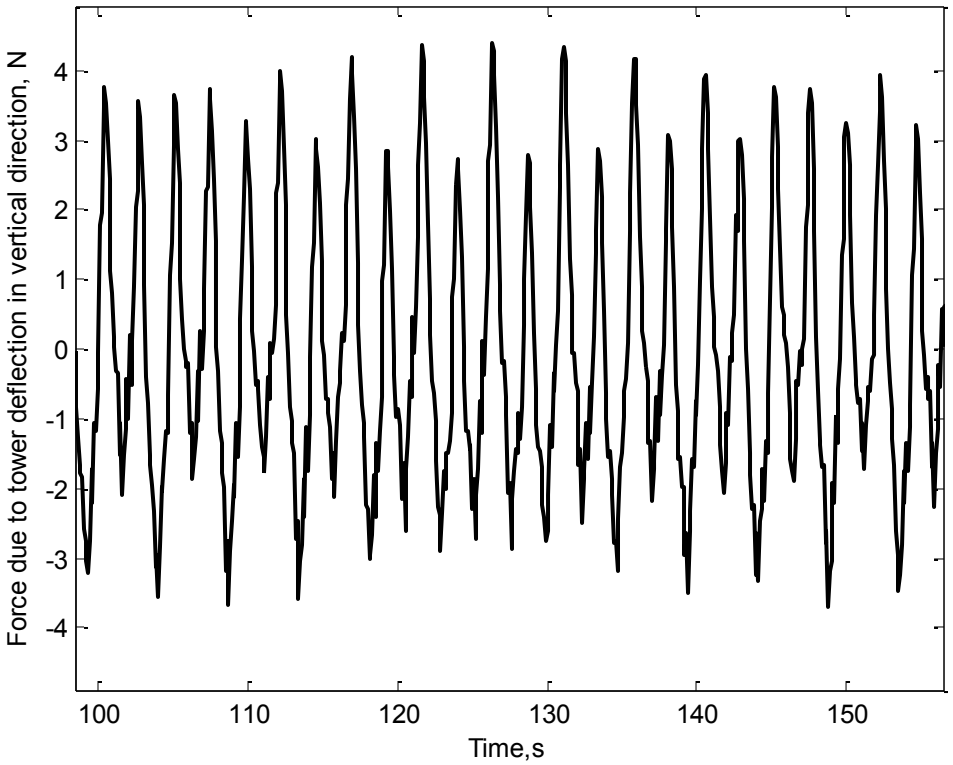

Figure 3.10 Force due to tower deflection in vertical direction under operational conditions of U=7 m/s, H_s = 1 m, T_s= 5 s in time domain

To investigate the frequency of the force presented in Figure 3.10, in Figure 3.11 this force is shown in frequency domain.

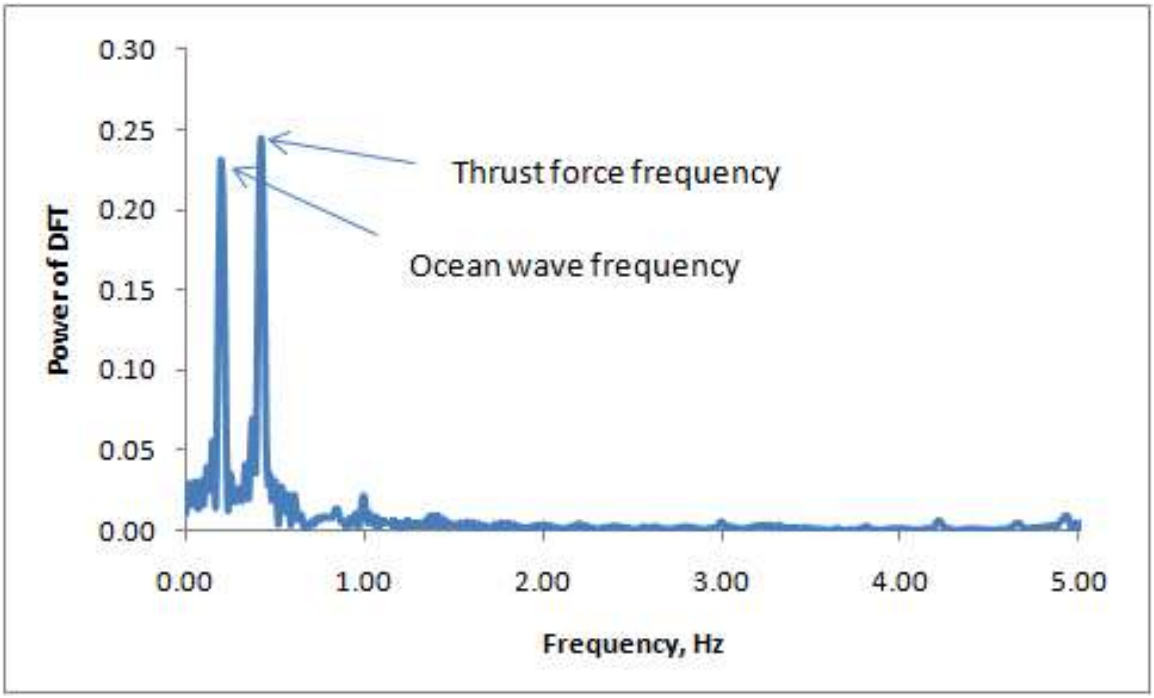

Figure 3.11 Force due to tower deflection in vertical direction under operational conditions of U=7 m/s, H_s = 1 m, T_s= 5 s in frequency domain.

As can be seen from Figure 3.11, for U=7 m/s, H_s = 1 m, T_s= 5 the ocean wave frequency and frequency of the thrust force, given in Figure 3.2 and 3.4, affect the force due to tower deflection in vertical direction almost equally.

To investigate the influence of wind speed on axial forces in the drive train, two additional simulations were run for wind speeds of 4 m/s and 12 m/s. Figure 3.12 and 3.13 shows how the thrust force changed with wind speed and Figure 3.14 shows the change of thrust force frequency.

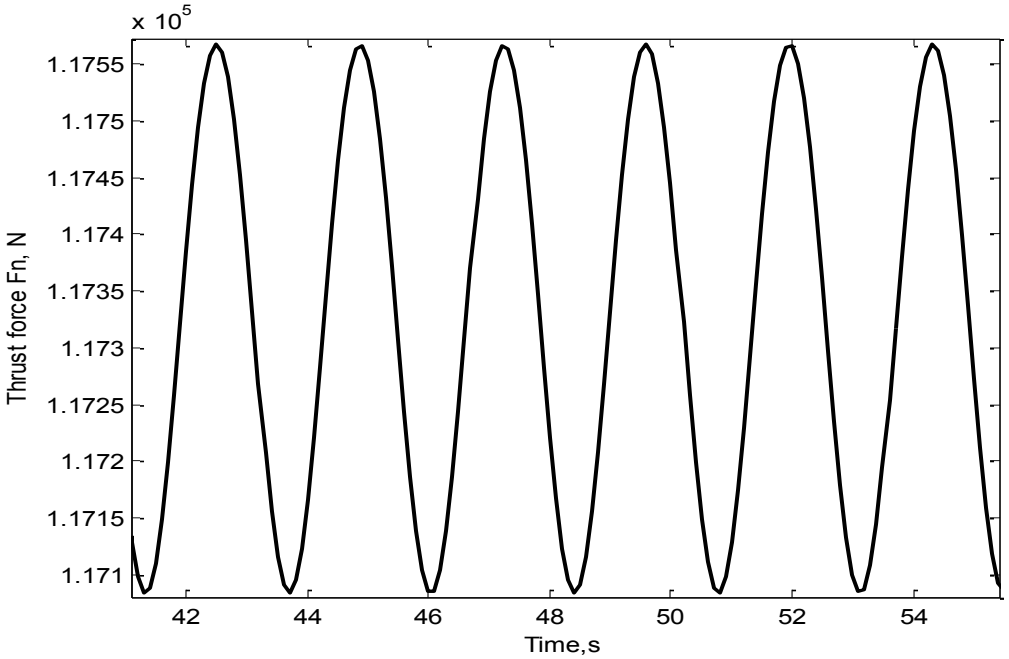

Figure 3.12 Thrust force, F_N, for wind speed of U=4 m/s in time domain

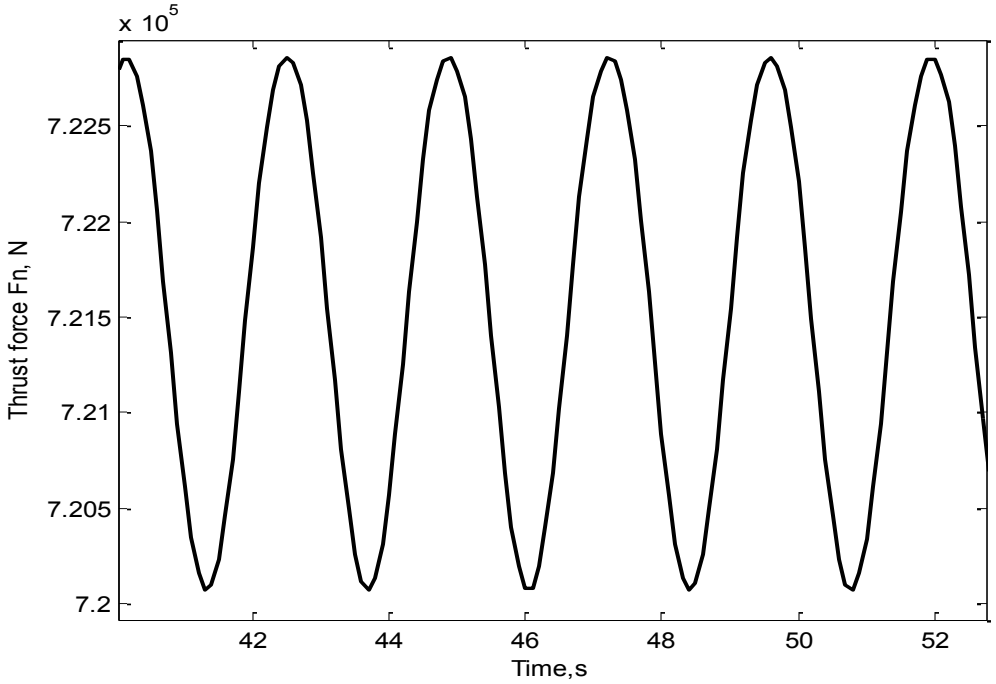

Figure 3.13 Thrust force, F_N, for wind speed of U=12 m/s in time domain

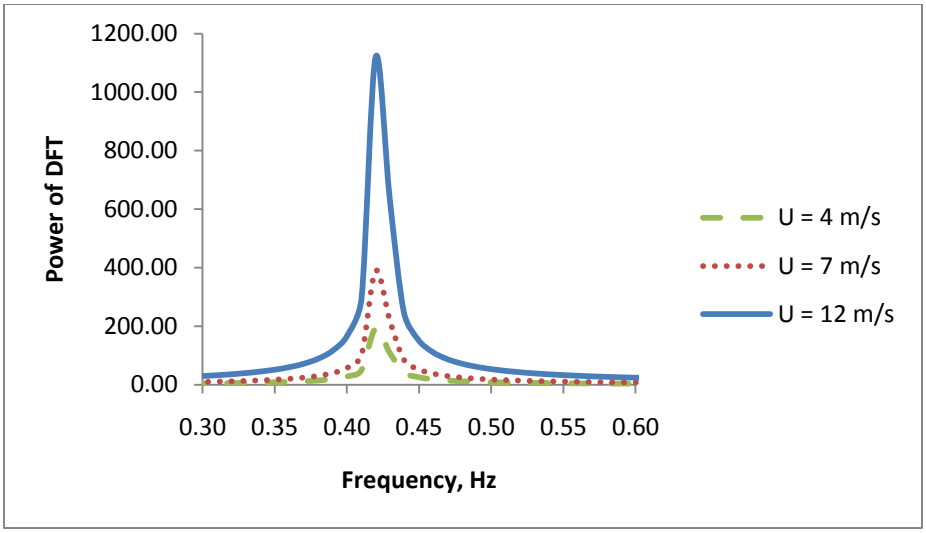

Figure 3.14 Thrust force, F_N, for different wind speed, in frequency domain domain

As can be seen from Figure 3.14, the frequency of thrust force do not change. Unlike the frequency, the magnitude of thrust force change with respect to change in wind speed, as shown in Figure 2.26 in Chapter 2.

Figure 3.15 – 3.16 show how the force in the main bearing in axial direction is affected by changes in wind speed and results are presented in frequency domain.

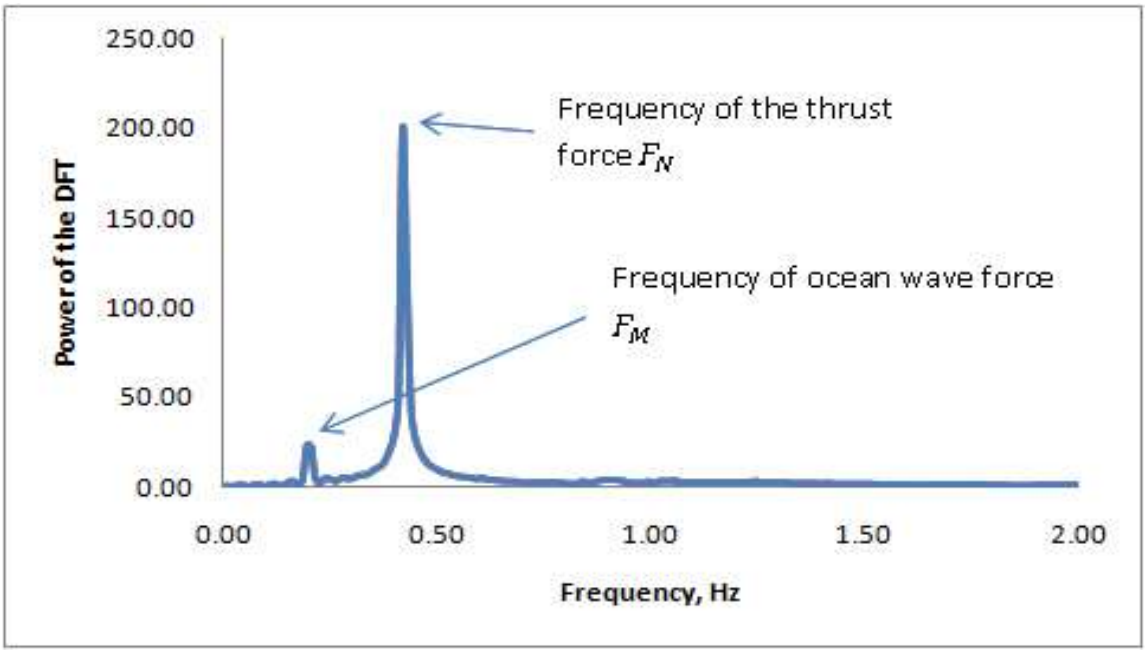

Figure 3.15 Force in the main bearing base, R_{bx} in axial direction, under operational conditions of U=4 m/s, H_s = 1 m, T_s= 5 s in frequency domain

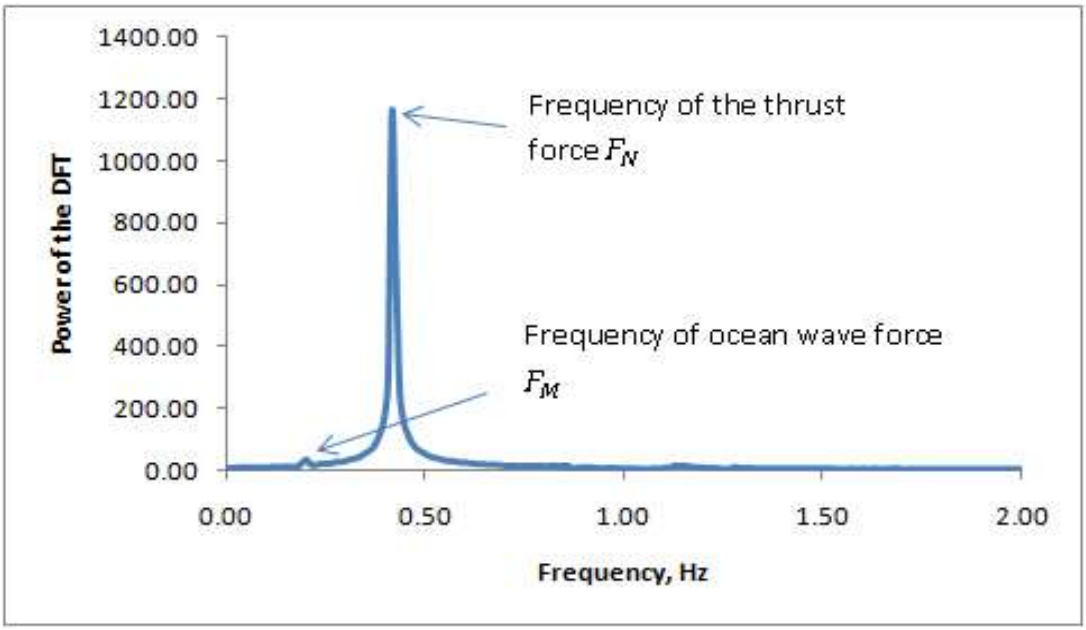

Figure 3.16 Force in the main bearing base, R_{bx} in axial direction, under operational conditions of U=12 m/s, H_s = 1 m, T_s= 5 s in frequency domain

Comparing Figures 3.7, 3.15 and 3.16 with Figure 3.14 for the thrust force of different wind speeds one may conclude that when wind speed increases, the mean value of reaction force R_{bx} in the main bearing increase as well. This is due to the higher mean value of thrust force which is determined by higher wind speed (Figure 3.1, 3.12 and 3.13). Additionally, Figures 3.7, 3.15 and 3.16 show that the higher wind speed is, the more it affect the reaction force R_{bx} in the main bearing comparing to ocean wave.

To make results more representative, reaction force in the main bearing R_{bx} is presented in nondimensional form, with respect to the total lift force F_L, produced on the rotor. In design process of thrust bearing the amplitude of reaction force n the main bearing in axial direction R_{bx} and its maximum value play the most important role. As a result, in Figure 3.17 through Figure 3.20, the non-dimensional value of amplitude A_{bx} and non-dimensional maximum force value N_{bx} are presented versus wind speed.

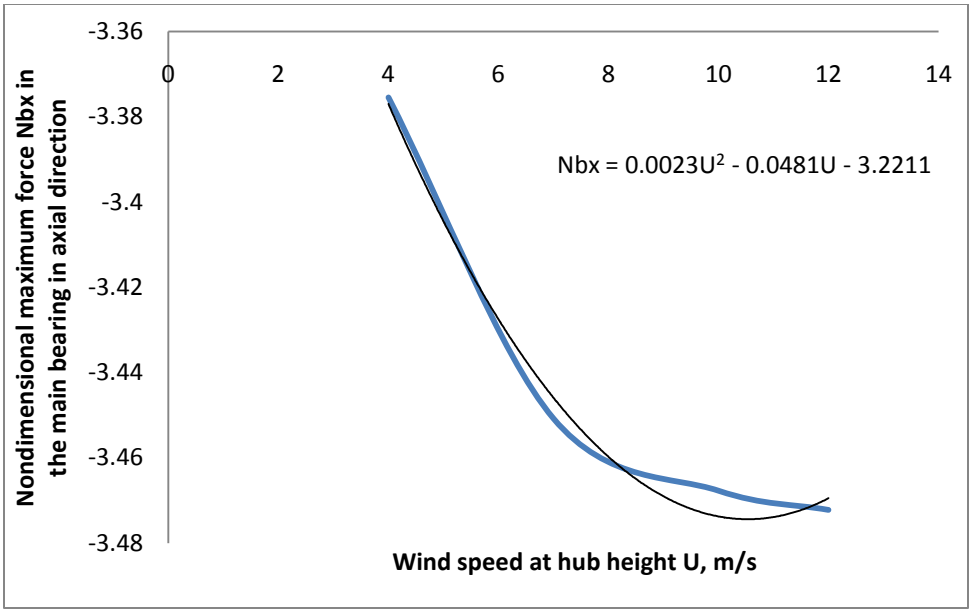

Figure 3.17 Non dimensional maximum force N_{bx} in the main bearing in axial direction for operational conditions of H_s = 1 m, T_s= 5 s.

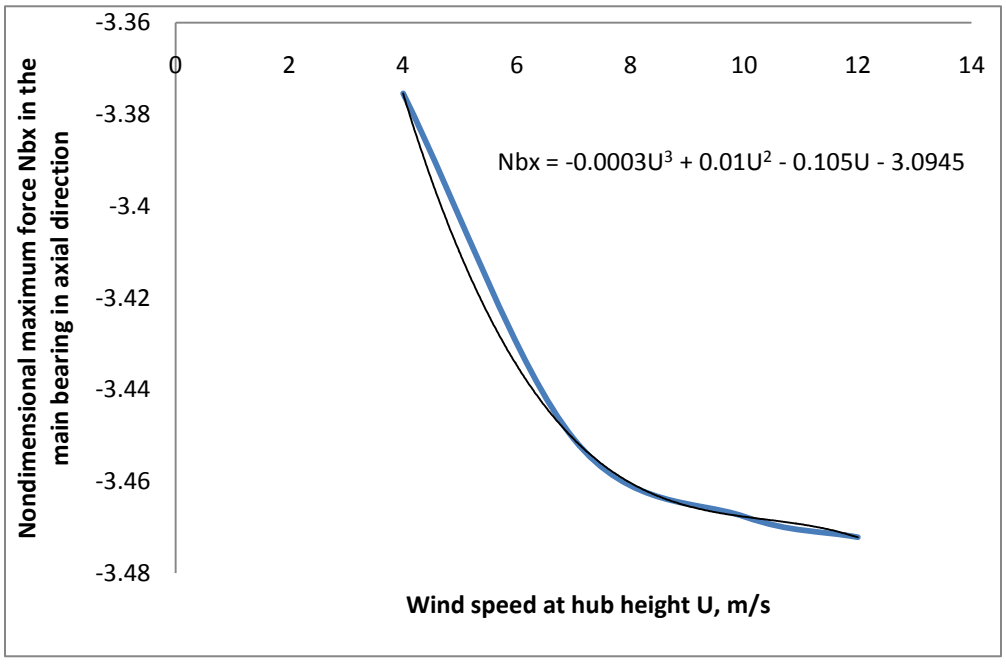

Figure 3.18 Non dimensional maximum force N_{bx} in the main bearing in axial direction for operational conditions of Hs = 1 m and Ts = 5 s.

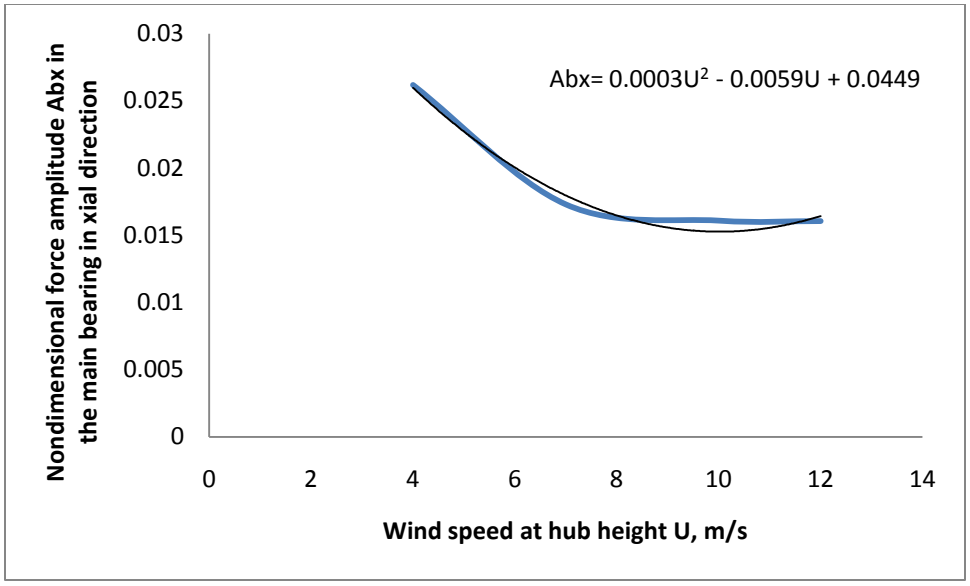

Figure 3.19 Non dimensional force amplitude A_{bx} in the main bearing in axial direction for operational conditions of Hs = 1 m and Ts = 5 s

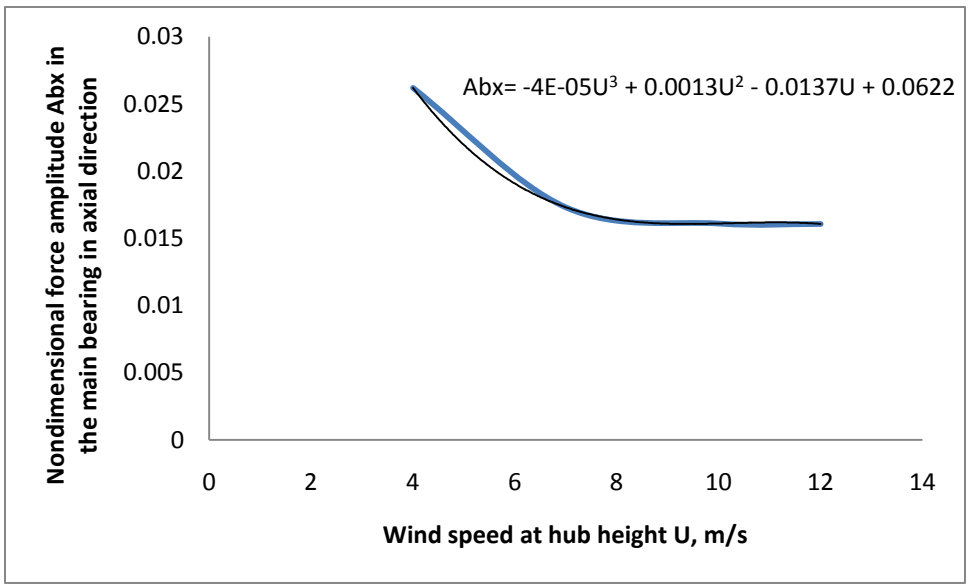

Figure 3.20 Non dimensional force amplitude A_{bx} in the main bearing in axial direction for operational conditions of H_s = 1 m, T_s= 5 s.

Figure 3.7 and Figure 3.9 show that curve for non dimensional force amplitude and maximum value fit better with third order polynomial. Additionally, above figure show that after

a wind speed of 7 m/s the ratio of force amplitude to the lift force is kept approximately constant. Unlike the amplitude, the ratio between the maximum value of the force in the main bearing and lift force is increasing rapidly beyond the wind speed of 7 m/s. Above this wind speed the growth rate increases. It confirms the fact, that wind turbine should be placed in region with average wind speed greater than 7 m/s (Jeffery et al., 2006) not only because more power can be extracted but also due to the less growth rate of forces in drive train components.

In vertical direction, reaction force in main bearing R_{bz} also determined mostly by thrust force. In Figure 3.21 and 3.22 results are shown in frequency domain.

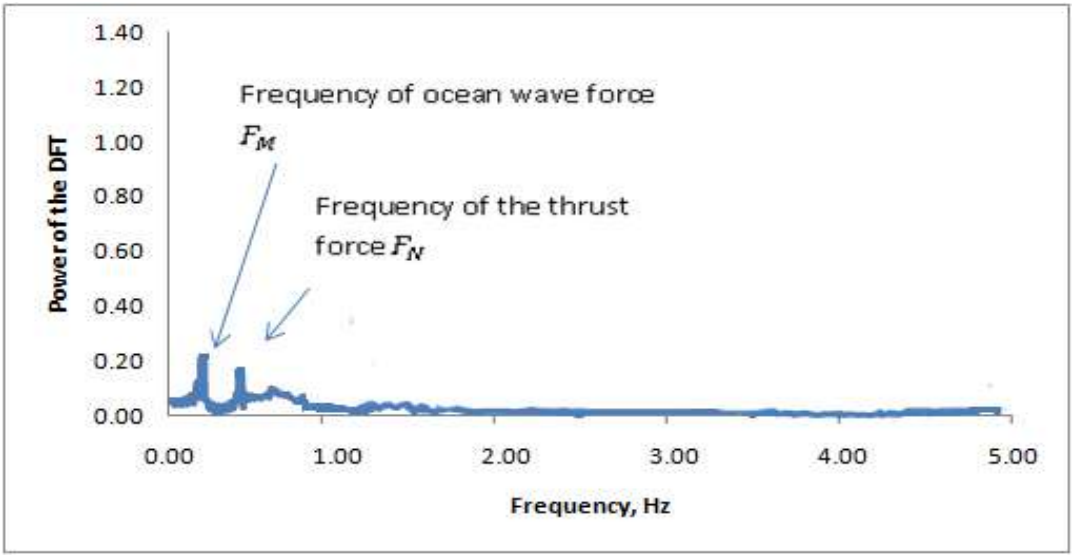

Figure 3.21 Force in the main bearing base, R_{bz} in vertical direction, under operational conditions of U= 4 m/s, H_s = 1 m, T_s= 5 s in frequency domain

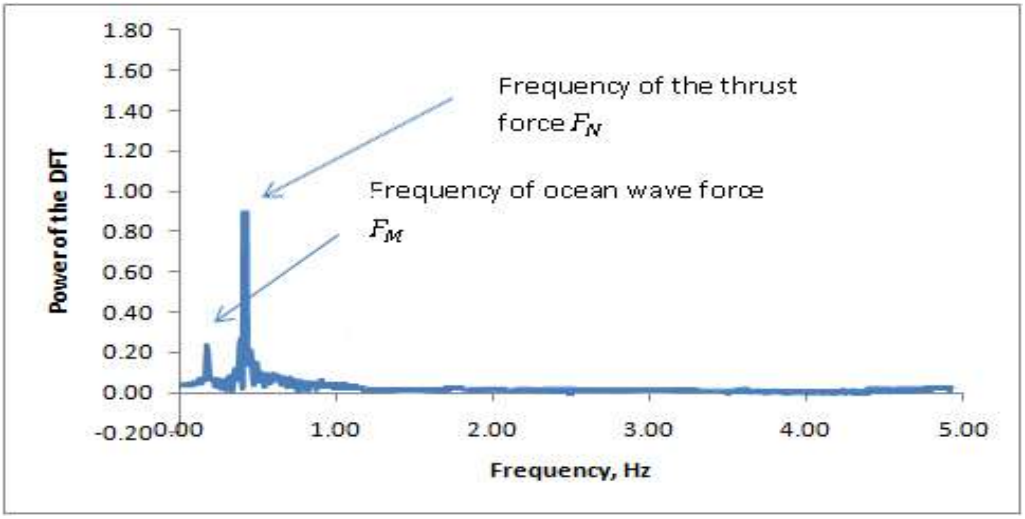

Figure 3.22 Force in the main bearing base, R_{bz} in vertical direction, under operational conditions of U=12 m/s, H_s = 1 m, T_s= 5 s in frequency domain

As can be seen from Figure 3.21 and 3.22 in vertical direction the frequency of thrust force is dominant for wind speed of 12 m/s, however for very low wind speeds of approximately 4 m/s the influence from ocean wave and thrust force become almost equal.

Results obtained for wind speed of 12 m/s are consistent with those obtained by Krogh (2004) for same operational conditions of H_s=1 m and T_s= 5 s. Maximum and mean value for reaction forces R_{bx} in the main bearing bases in axial direction obtained from current model and those, predicted by Krogh (2004) are presented in Table 3.2.

Table 3.2 Maximum and mean value of reaction force in the main bearing in axial direction calculated from Krogh (2004) study and from current work.

Investigated value	Results obtained by Krogh (2004)	Results calculated in current work
Maximum reaction force in the main bearing in axial direction	7.80e2, kN	7.23e2, kN
Mean value of the reaction force in the main bearing in axial direction	7.53e2, kN	7.21e2, kN

As can be seen from the table the maximum value predicted by Krogh (2004) is higher than calculated in current project. This is mainly because Krogh (2004) includes a blade dynamics in his analysis. The dynamics of the blades affect an air flow past the blades and, as a result, forces generated in the drive train. However, the mean value is very similar with error less than 5 %.

In addition to the above discussions, the following one addresses the influence of ocean wave height and period on drive train force. Based on Morison's equation (Morison et al., 1950), the amplitude of ocean wave forces increases when the ocean waves become larger. This is shown in Figure 3.23 and Figure 3.24. When the ocean wave height becomes zero, it is clear that wave force also zero.

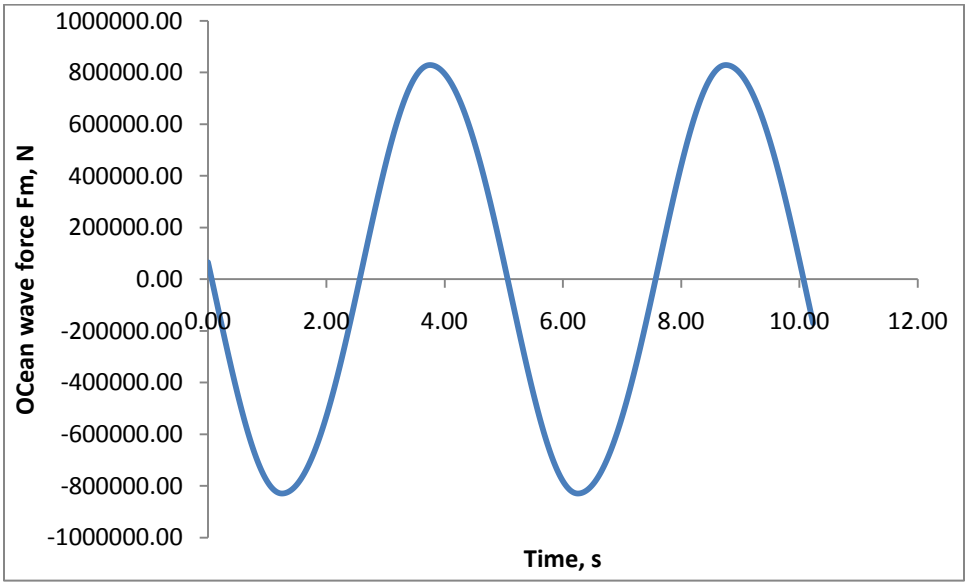

Figure 3.23 Ocean wave force, F_M, for H_s = 5 m and T_s = 5 s, in time domain.

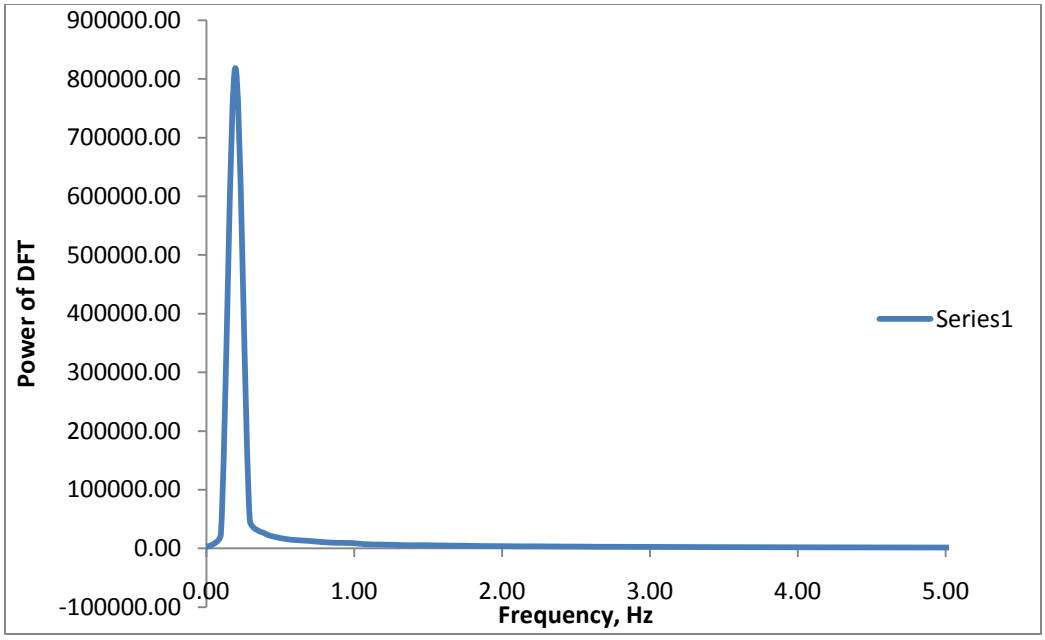

Figure 3.24 Ocean wave force, F_M, for H_s = 5 m and T_s = 5 s, in frequency domain.

However, the influence of rise in amplitude of ocean wave force on axial force R_{bx} excursion and mean value in the main bearing is less than influence from the thrust force. As a result, the mean value of axial forces in bearing base is not affected by change in ocean wave height. This is shown in Figure 3.25 and 3.26.

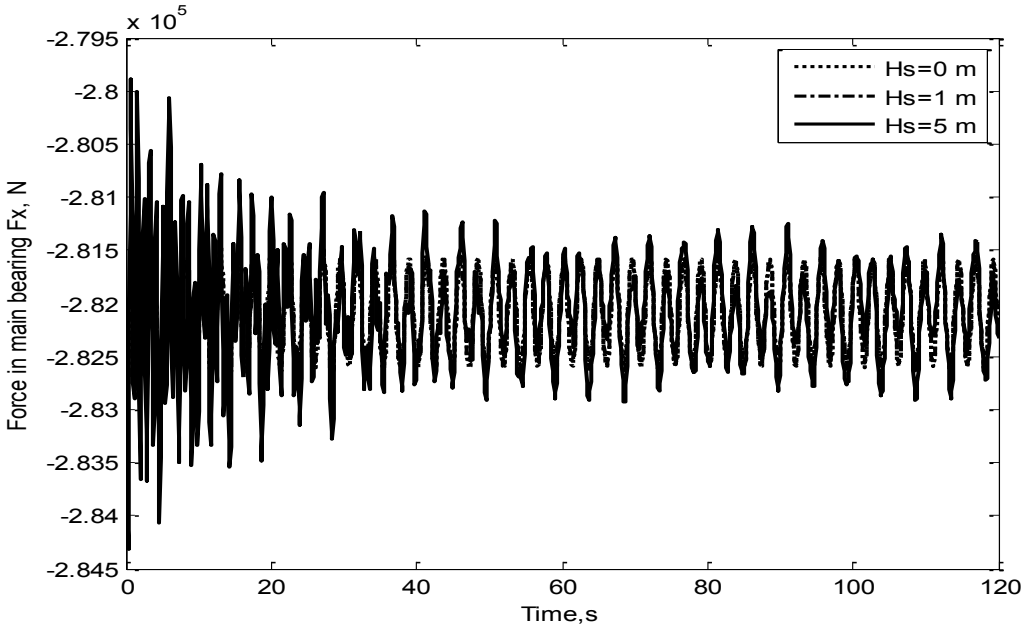

Figure 3.25 Force in the main bearing base R_{bx} for ocean wave heights of Hs= 0 m, Hs = 1 m and H_s = 5 m with U = 7 m/s, T_s =5 s.

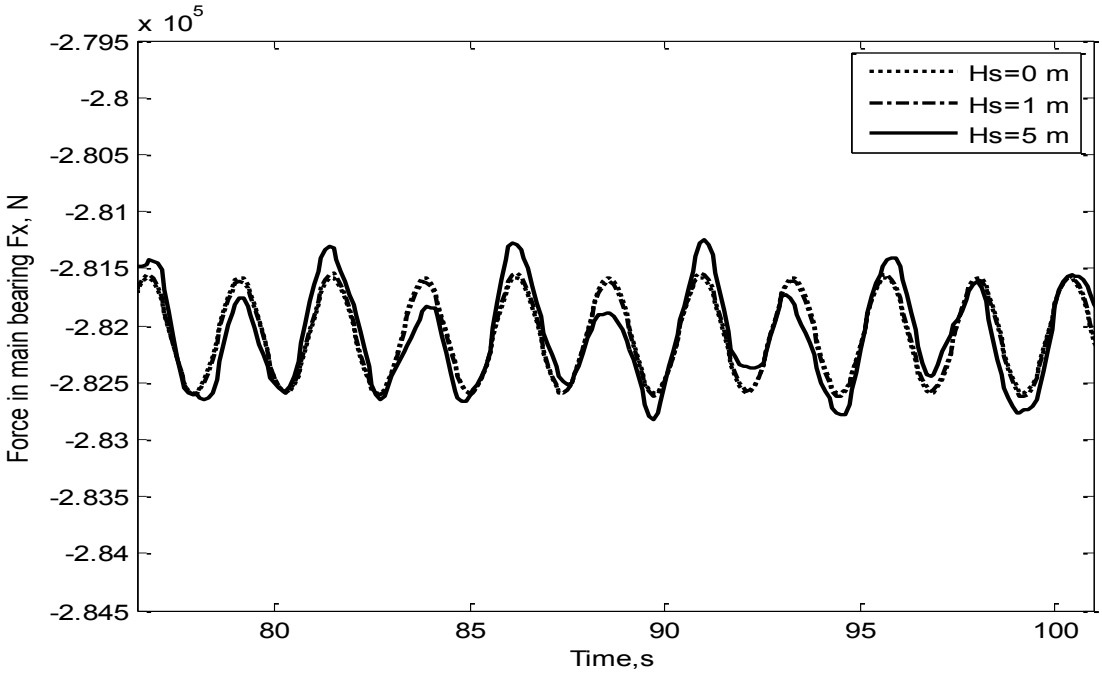

Figure 3.26 Force in the main bearing base R_{bx} for ocean wave heights of H_s= 0 m, H_s = 1 m and H_s = 5 m with U = 7 m/s, T_s =5 s.

The condition with H_s =0 m is similar to conditions for wind turbine mounted on land. Therefore, the fact that mean value do not change agrees with conclusion derived by Shim (2007) and Jonkman (2007). It confirms that mean values of loads in off-shore wind turbines is very similar to those that existed on the land. The curve for $H_s = 0$ m is almost coincide with $H_s = 1$ m in Figure 3.26. To show the difference between this curves and show which externally applied force affect force in the main bearing base R_{bx} mostly, results from Figure 3.25 is shown in frequency domain in Figure 3.27 and 3.28.

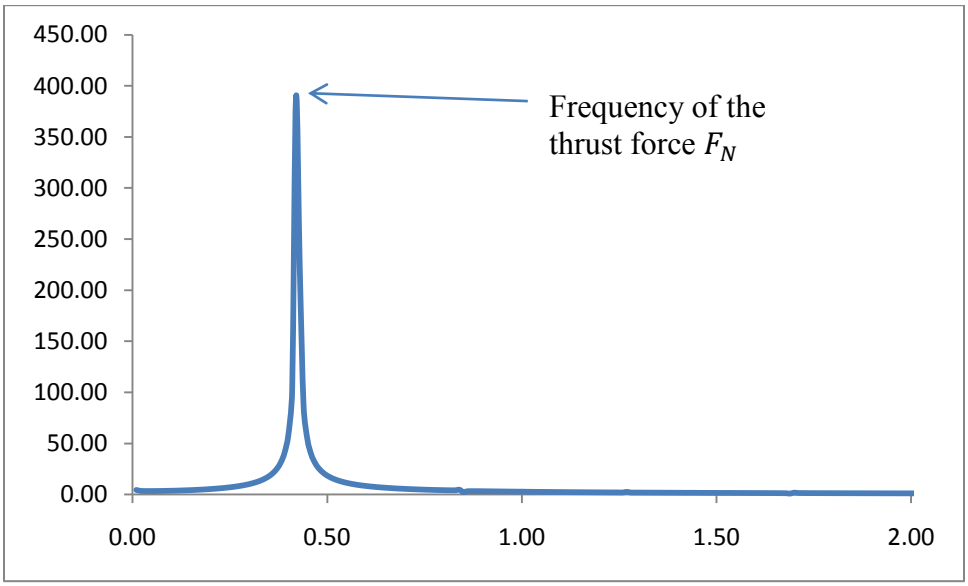

Figure 3.27 Force in the main bearing base, R_{bx} in axial direction, under operational conditions of U=7 m/s, H_s = 0 m, T_s= 5 s in frequency domain

Comparing Figure 3.27 to Figure 3.7, one my conclude that when H_s = 0 m the frequency associated with wave is equal zero. Only frequency of the thrust force is presented in this case.

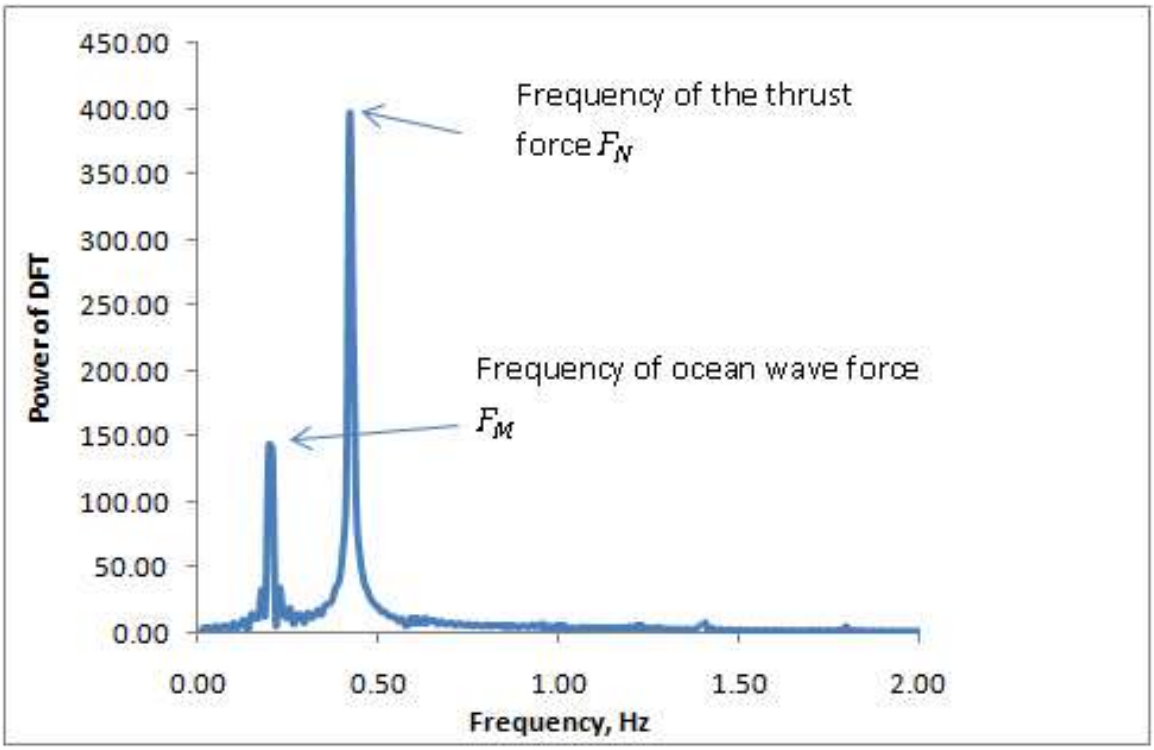

Figure 3.28 Force in the main bearing base, R_{bx} in axial direction, under operational conditions of U=7 m/s, H_s = 5 m, T_s= 5 s in frequency domain

Another parameter investigated in this study was an ocean wave period. Based on Equation 2.19, ocean wave period affects only the frequency of ocean wave. This is shown in Figure 3.29.

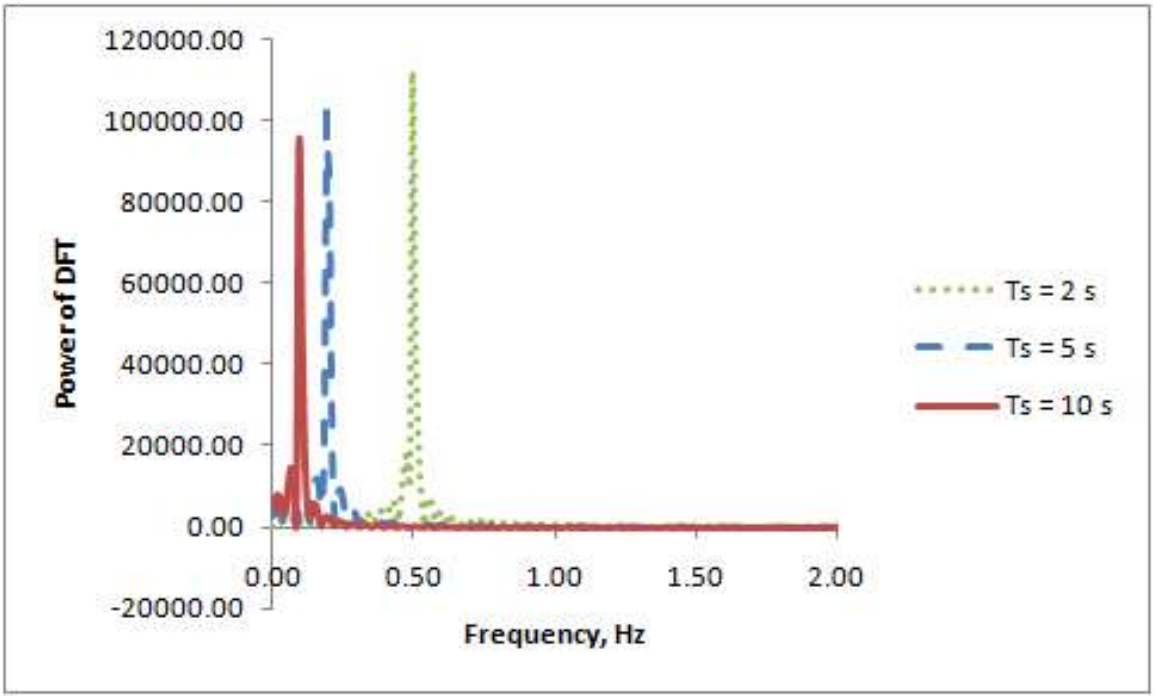

Figure 3.29 Ocean wave force, F_M, for ocean wave periods of T_s = 2 s, T_s = 5 s and T_s = 10 s with H_s =1 m, in frequency domain.

In Figure 3.30 and 3.31 reaction force in the main bearing R_{bx} is presented.

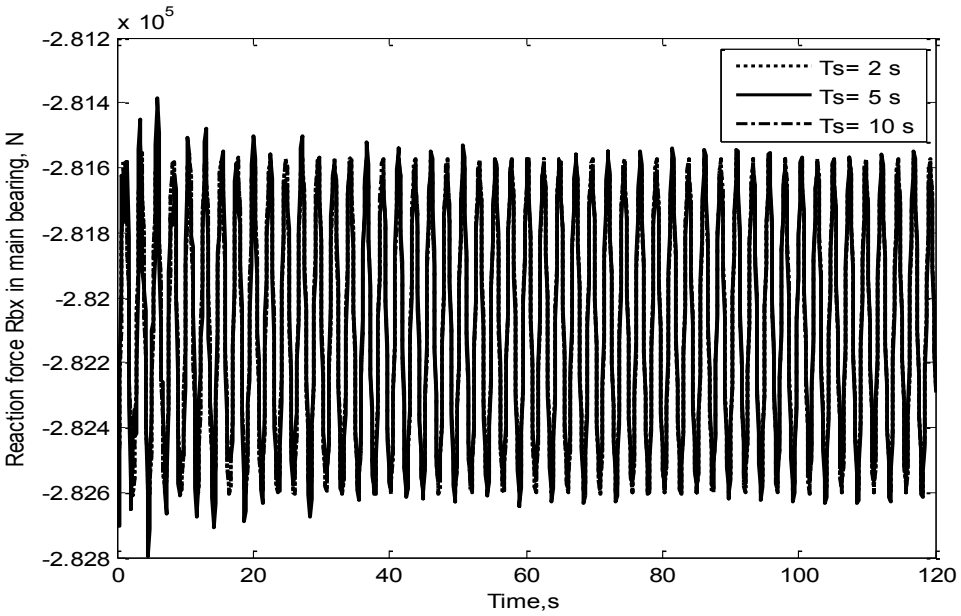

Figure 3.30 Force in the main bearing base R_{bx} for ocean wave periods of T_s = 2 s, T_s = 5 s and T_s = 10 s with H_s =1 m, U= 7 m/s.

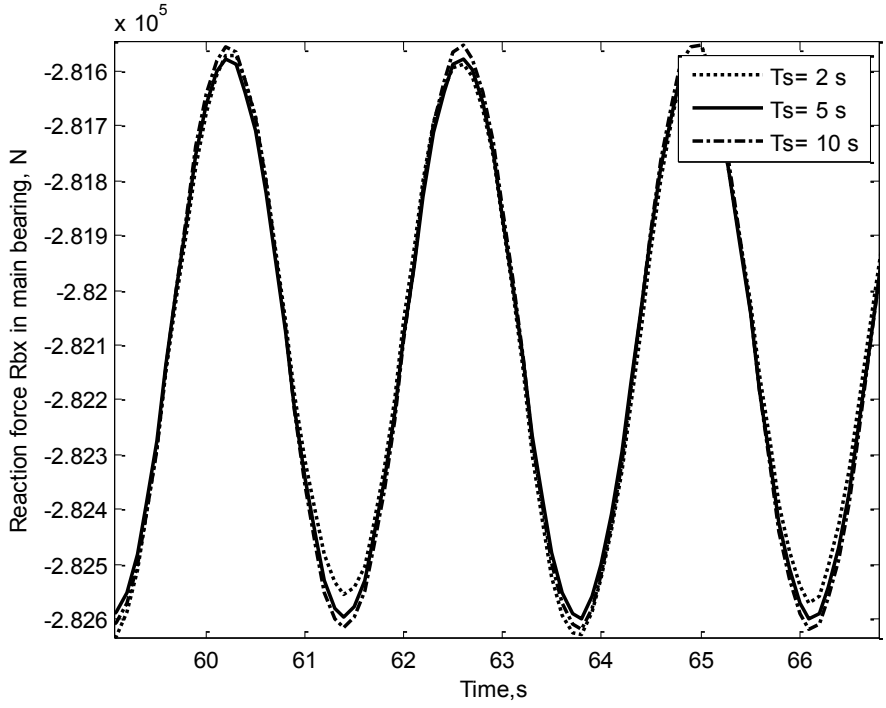

Figure 3.31 Force in the main bearing base R_{bx} for ocean wave periods of T_s = 2 s, T_s = 5 s and T_s = 10 s with H_s =1 m, U= 7 m/s.

To investigate force in the main bearing base R_{bx} more precisely, in Figure 3.32 and 3.33 this force is shown in frequency domain.

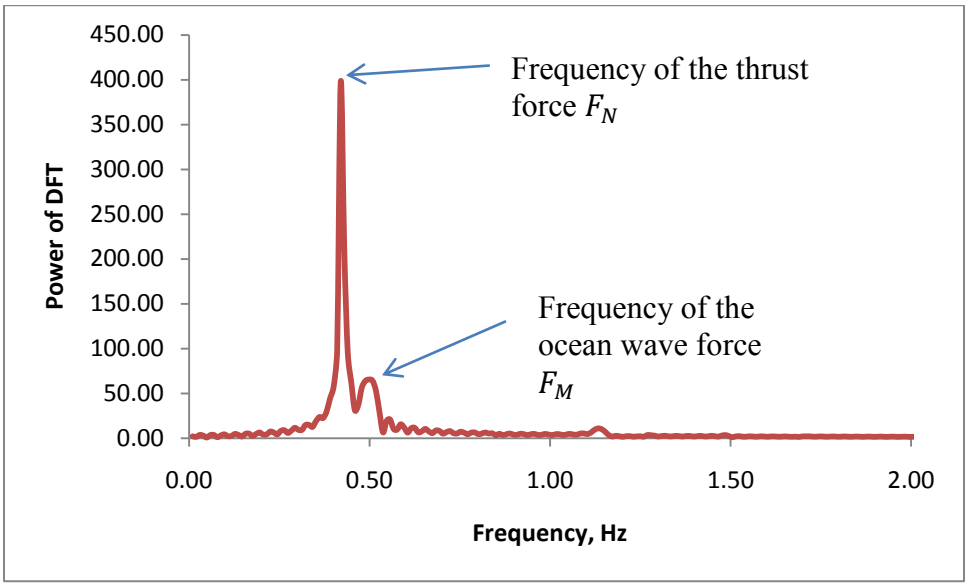

Figure 3.32 Force in the main bearing base, R_{bx} in axial direction, under operational conditions of U=7 m/s, H_s = 1 m, T_s= 2 s in frequency domain

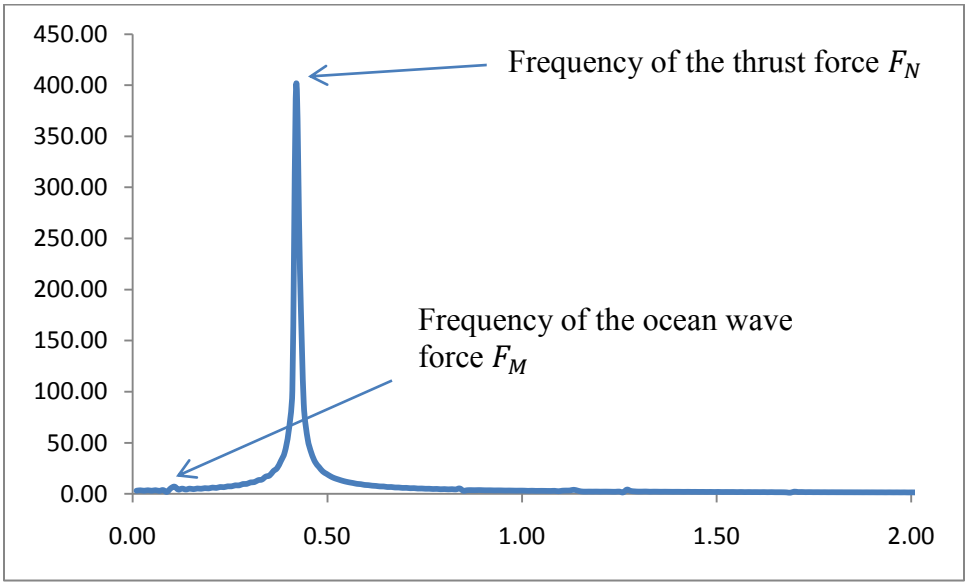

Figure 3.32 Force in the main bearing base, R_{bx} in axial direction, under operational conditions of U=7 m/s, H_s = 1 m, T_s= 2 s in frequency domain

As can be seen from above Figures 3.31 and 3.32, the effect from ocean wave period on reaction force in the main bearing R_{bx} in axial direction is still very small, comparing to thrust force. Therefore, the value of this force calculated for different ocean wave periods is very similar.

CHAPTER FOUR

CONCLUSIONS AND RECOMMENDATIONS

Conclusions

A model of 5MW off-shore wind turbine was constructed to model dynamic forces arising in drive train components. Aerodynamic forces originating from the rotating rotor were calculated separately using MATLAB. Developed code was based on blade element theory in which the turbine blade span is subdivided and aggregate forces on the hub are determined by summing up the lift and drag forces of each element. Calculated values of thrust force, rotor torque and rotor power were validated with those obtained by NREL (Jonkman, 2007). For wind speeds between cut-in and rated wind speed which is about 12 m/s, the value of thrust force obtained in current work are in a good agreement with that calculated by NREL code (Jonkman, 2007). Above this range, the value of thrust force is keep increasing because no control mechanisms are considered to regulate position of the blades.

The off-shore wind turbine was based on site conditions of the nearby South Carolina coast. To calculate dynamic forces in drive train components, finite element model of actual 5MW wind turbine based on NREL (Jonkman, 2007) and Ris∅ (Krogh, 2004) 5MW wind turbine prototypes was constructed. By use of COMSOL multi physics software mesh and finite model were developed. Ocean wave and wind drag forces were modeled as additional externally applied forces on tower. Mesh size and time step was chosen in a way to guarantee the feasibility of dynamic response in drive train components. Sensitivity analysis of forces in drive train to mesh size was performed for three different meshes. Based on this verification analysis, the normal mesh with maximum element size of 0.1 m and minimum element size of 0.01 m was chosen. This guaranteed a good mesh in very thin geometry which was given by tower wall

thickness. Time step size of 0.1 s was chosen based on sensitivity analysis of forces in drive train to time step size. This guaranteed that important dynamic behavior of the system was not omitted. To show dynamic response in drive train components, simulations were run in time domain series. Simulation time was 120 s, which guaranteed that steady periodic behavior of the system was reached. Return method was used to prove it. Closed loops obtained by this method for forces in drive train components denoted the steady periodic behavior of the system. To characterize this response, the mean and maximum values were compared to those obtained by Krogh (2004). Higher maximum value of forces in drive train components received by Krogh (2004) was explained by including blade dynamics in his analysis. However, the mean value of these forces was in a good agreement with Krogh's study (2004).

Additionally, influences of wind speed, ocean wave height, and ocean wave period on drive train dynamics were investigated. Based on obtained results, it was concluded that magnitude of axial force R_{bx} in the drive train components depend mostly on thrust force produced on the rotor by the three turbine blades. It was observed also that the mean value of this force for different sea-state conditions was very similar. This fact confirms the conclusion derived by Jonkman (2007) and Shim (2007) that means values of loads in an off-shore wind turbine are very similar to those that pertain to land-based wind turbines. Additionally, it was observed that vertical forces in drive train components R_{bz} only determined by weight of components and not affected by any change in wind speed, ocean wave height and ocean wave period.

Recommendations

This study has demonstrated the capability of computational model to capture dynamic behavior in drive train components. However, there have been some limitations to this study. Many of these limitations can potentially be overcome in future research.

For future study, constructed computational model of actual wind turbine can be used to estimate forces acting on drive train components. Developed numerical code can be used to calculate aerodynamic forces on the rotor, which are the main source of loading in drive train components. This information can be used to design reliable drive train elements and decrease risk of failure in these components. The computational model could also be used as a tool to investigate stress concentration in wind turbine tower and foundation.

In current study, wind turbine tower foundation was considered bottom-mounted and perfectly rigid. However, in actual wind turbine, tower foundation is buried to soft clay of a sea floor. This allows the movement of this portion of the tower that in turn produces a tower oscillation and as a result increases forces in drive train components. To account for this, soil-structure interaction between soft clay and buried portion of the tower should be modeled.

Another limitation of this study comes from fluid-structure interaction between wind, wave and wind turbine blades and tower. To account for dynamics of the blades and possible effects of these dynamics on air flow past the blades and on forces generated in the drive train, developed numerical code has to be modified.

Finally, to investigate whole range of wind speeds the stall delay and pitch mechanisms have to be invoked to regulate the blade's position.

APPENDIX

```
%% This program code was developed to calculate aerodynamic forces arise
%  on the rotor. Algorithm is based on blade element theory and momentum
%  theory.

clear all;
close all;
clc

%% Load aerofoils data

DU21 = readin('DU21_A17.dat');
DU25 = readin('DU25_A17.dat');
DU30 = readin('DU30_A17.dat');
DU35 = readin('DU35_A17.dat');
DU40 = readin('DU40_A17.dat');
NACA64 = readin('NACA64_A17.dat');

%% Input parameters

H_hub = 90; %Hub height, m
r = readin('radius.txt'); %Radial position of the nodes w.r.t rotor center, m
R = r(size(r,1),1); %Radius of the blade, m
c = readin('chord.txt'); %Chord lenght, m
twist = readin('twist_angle.txt'); %Twist angle, degree
omega_initial(3:25,1) = readin('omega initial.txt'); %Rotational sped of the
rotor, rpm
omega(1:25,1) = omega_initial(1:25,1)/60*2*pi; %Rotational sped of the rotor,
rad/s
B = 3; %Number of bades
rho = 1.125; % Air density, kg/m^3
a_c = 0.2; %Critical axial induction factor for Glauert correction

eps = 1e-6; %Tollerance
power = 5e6; %Power output

%%
for V_hub = 3:25
    u(V_hub,1) = V_hub;
    T_sum(V_hub,1) = 0;
    M_sum(V_hub,1) = 0;
    L_sum(V_hub,1) = 0;
    p_t(1,1) = 0;
    p_n(1,1) = 0;
      n(1,1) = 0;
      n(2:size(r,1)+1,1) = r(:,1);

    for i = 1:size(r,1)
        a_a(i,1) = 0; %Initial guess for axial induction factor
        a_t(i,1) = 0; %Initial guess for angular induction factor
        V_0(i,1) = V_hub*((H_hub + r(i,1))/H_hub)^(1/7); %Inflow wind speed
calculated as a shear exponent, m/s
        delta_a = 100;
        delta_t = 100;
        z = 1;
```

```
        while (abs(delta_a) > eps) || (abs(delta_t) > eps)
            phi(i,1) = atan((1 - a_a(i,1))*V_0(i,1)/((1 +
a_t(i,1))*omega(V_hub,1)*r(i,1)));

            alpha(i,1) = phi(i,1) - twist(i,1)*pi/180; %Local angle of attack,
degree
            alpha(i,1) = alpha(i,1)*180/pi;
            j = 1;
            if i < 3
                Cl(i,1) = 0; %Lift coefficient of Cylinder1
                Cd(i,1) = 0.5; %Drag coefficient of Cylinder1
            elseif i == 3
                Cl(i,1) = 0; %Lift coefficient of Cylinder2
                Cd(i,1) = 0.35; %Drag coefficient of Cylinder2
            elseif i == 4
                while alpha(i) > DU40(j,1) %Find bounds for alpha, from table
                    lower = j;
                    j = j + 1;
                    upper = j;
                end
                if DU40(lower,2) < DU40(upper,2)
                    Cl(i,1) = DU40(lower,2) + (alpha(i,1) -
DU40(lower,1))*(DU40(upper,2) - DU40(lower,2))/(DU40(upper,1) - DU40(lower,1));
%Interpolated lift coefficient of DU40
                else
                    Cl(i,1) = DU40(upper,2) + (DU40(upper,1) -
alpha(i,1))*(DU40(lower,2) - DU40(upper,2))/(DU40(upper,1) - DU40(lower,1));
                end
                if DU40(lower,3) > DU40(upper,3)
                    Cd(i,1) = DU40(upper,3) + (DU40(upper,1) -
alpha(i,1))*(DU40(lower,3) - DU40(upper,3))/(DU40(upper,1) - DU40(lower,1));
%Interpolated lift coefficient of DU40
                else
                    Cd(i,1) = DU40(lower,3) + (alpha(i,1) -
DU40(lower,1))*(DU40(upper,3) - DU40(lower,3))/(DU40(upper,1) - DU40(lower,1));
                end
            elseif (i > 4) && (i < 7)
                while alpha(i,1) > DU35(j,1) %Find bounds for alpha, from table
                    lower = j;
                    j = j + 1;
                    upper = j;
                end
                if DU35(lower,2) < DU35(upper,2)
                    Cl(i,1) = DU35(lower,2) + (alpha(i,1) -
DU35(lower,1))*(DU35(upper,2) - DU35(lower,2))/(DU35(upper,1) - DU35(lower,1));
%Interpolated lift coefficient of DU35
                else
                    Cl(i,1) = DU35(upper,2) + (DU35(upper,1) -
alpha(i,1))*(DU35(lower,2) - DU35(upper,2))/(DU35(upper,1) - DU35(lower,1));
                end
                if DU35(lower,3) > DU35(upper,3)
                    Cd(i,1) = DU35(upper,3) + (DU35(upper,1) -
alpha(i,1))*(DU35(lower,3) - DU35(upper,3))/(DU35(upper,1) - DU35(lower,1));
%Interpolated lift coefficient of DU35
                else
                    Cd(i,1) = DU35(lower,3) + (alpha(i,1) -
DU35(lower,1))*(DU35(upper,3) - DU35(lower,3))/(DU35(upper,1) - DU35(lower,1));
                end
```

```
            elseif i == 7
                while alpha(i,1) > DU30(j,1) %Find bounds for alpha, from table
                    lower = j;
                    j = j + 1;
                    upper = j;
                end
                if DU30(lower,2) < DU30(upper,2)
                    Cl(i,1) = DU30(lower,2) + (alpha(i,1) -
DU30(lower,1))*(DU30(upper,2) - DU30(lower,2))/(DU30(upper,1) - DU30(lower,1));
%Interpolated lift coefficient of DU30
                else
                    Cl(i,1) = DU30(upper,2) + (DU30(upper,1) -
alpha(i,1))*(DU30(lower,2) - DU30(upper,2))/(DU30(upper,1) - DU30(lower,1));
                end
                if DU30(lower,3) > DU30(upper,3)
                    Cd(i,1) = DU30(upper,3) + (DU30(upper,1) -
alpha(i,1))*(DU30(lower,3) - DU30(upper,3))/(DU30(upper,1) - DU30(lower,1));
%Interpolated lift coefficient of DU30
                else
                    Cd(i,1) = DU30(lower,3) + (alpha(i,1) -
DU30(lower,1))*(DU30(upper,3) - DU30(lower,3))/(DU30(upper,1) - DU30(lower,1));
                end
            elseif (i > 7) && (i < 10)
                while alpha(i,1) > DU25(j,1) %Find bounds for alpha, from table
                    lower = j;
                    j = j + 1;
                    upper = j;
                end
                if DU25(lower,2) < DU25(upper,2)
                    Cl(i,1) = DU25(lower,2) + (alpha(i,1) -
DU25(lower,1))*(DU25(upper,2) - DU25(lower,2))/(DU25(upper,1) - DU25(lower,1));
%Interpolated lift coefficient of DU25
                else
                    Cl(i,1) = DU25(upper,2) + (DU25(upper,1) -
alpha(i,1))*(DU25(lower,2) - DU25(upper,2))/(DU25(upper,1) - DU25(lower,1));
                end
                if DU30(lower,3) > DU30(upper,3)
                    Cd(i,1) = DU25(upper,3) + (DU25(upper,1) -
alpha(i,1))*(DU25(lower,3) - DU25(upper,3))/(DU25(upper,1) - DU25(lower,1));
%Interpolated lift coefficient of DU25
                else
                    Cd(i,1) = DU25(lower,3) + (alpha(i,1) -
DU25(lower,1))*(DU25(upper,3) - DU25(lower,3))/(DU25(upper,1) - DU25(lower,1));
                end
            elseif (i > 9) && (i < 12)
                while alpha(i,1) > DU21(j,1) %Find bounds for alpha, from table
                    lower = j;
                    j = j + 1;
                    upper = j;
                end
                if DU21(lower,2) < DU21(upper,2)
                    Cl(i,1) = DU21(lower,2) + (alpha(i,1) -
DU21(lower,1))*(DU21(upper,2) - DU21(lower,2))/(DU21(upper,1) - DU21(lower,1));
%Interpolated lift coefficient of DU21
                else
                    Cl(i,1) = DU21(upper,2) + (DU21(upper,1) -
alpha(i,1))*(DU21(lower,2) - DU21(upper,2))/(DU21(upper,1) - DU21(lower,1));
                end
                if DU30(lower,3) > DU30(upper,3)
```

```
                    Cd(i,1) = DU21(upper,3) + (DU21(upper,1) -
alpha(i,1))*(DU21(lower,3) - DU21(upper,3))/(DU21(upper,1) - DU21(lower,1));
%Interpolated lift coefficient of DU21
                else
                    Cd(i,1) = DU21(lower,3) + (alpha(i,1) -
DU21(lower,1))*(DU21(upper,3) - DU21(lower,3))/(DU21(upper,1) - DU21(lower,1));
                end
            else
                while alpha(i,1) > NACA64(j,1) %Find bounds for alpha, from
table
                    lower = j;
                    j = j + 1;
                    upper = j;
                end
                if NACA64(lower,2) < NACA64(upper,2)
                    Cl(i,1) = NACA64(lower,2) + (alpha(i,1) -
NACA64(lower,1))*(NACA64(upper,2) - NACA64(lower,2))/(NACA64(upper,1) -
NACA64(lower,1)); %Interpolated lift coefficient of NACA64
                else
                    Cl(i,1) = NACA64(upper,2) + (NACA64(upper,1) -
alpha(i,1))*(NACA64(lower,2) - NACA64(upper,2))/(NACA64(upper,1) -
NACA64(lower,1));
                end
                if NACA64(lower,3) > NACA64(upper,3)
                    Cd(i,1) = NACA64(upper,3) + (NACA64(upper,1) -
alpha(i,1))*(NACA64(lower,3) - NACA64(upper,3))/(NACA64(upper,1) -
NACA64(lower,1)); %Interpolated lift coefficient of NACA64
                else
                    Cd(i,1) = NACA64(lower,3) + (alpha(i,1) -
NACA64(lower,1))*(NACA64(upper,3) - NACA64(lower,3))/(NACA64(upper,1) -
NACA64(lower,1));
                end
            end

            Cn(i,1) = Cl(i,1)*cos(phi(i,1)) + Cd(i,1)*sin(phi(i,1)); %Normal
coefficient
            Ct(i,1) = Cl(i,1)*sin(phi(i,1)) - Cd(i,1)*cos(phi(i,1));
%Tangential coefficient

            sigma(i,1) = c(i,1)*B/(2*pi*r(i,1)); %Local solidity
            lambda = R*omega(V_hub,1)/V_hub; %Tip speed ration
            C_thrust(i,1) = sigma(i,1)*(1 -
a_a(i,1))^2*Cn(i,1)/sin(phi(i,1))^2; %Thrust coefficient
            r_hub = 1.5;
            f_tip(i,1) = B/2*(R - r(i,1))/(r(i,1)*sin(phi(i,1)));
            f_hub(i,1) = B/2*(r(i,1) - r_hub)/(r(i,1)*sin(phi(i,1)));
            F(i,1) = 2/pi*acos(exp(-f_tip(i,1)))*2/pi*acos(exp(-f_hub(i,1)));
%Prandtl tip loss factor

            a_t_new(i,1) =
(4*F(i,1)*sin(phi(i,1))*cos(phi(i,1))/(sigma(i,1)*Ct(i,1)) - 1)^(-1);

            if a_a(i,1) < a_c %Glauert correction
                a_a_new(i,1) = (4*F(i,1)*(sin(phi(i,1)))^2/(sigma(i,1)*Cn(i,1))
+ 1)^(-1);
            else
                K(i,1) = 4*F(i,1)*(sin(phi(i,1)))^2/(sigma(i,1)*Cn(i,1));
```

```
                a_a_new(i,1) = 0.5*(2 + K(i,1)*(1 - 2*a_c) - sqrt((K(i,1)*(1 -
2*a_c) + 2)^2 + 4*(K(i,1)*a_c^2 - 1)));
            end

            delta_a = a_a_new(i,1) - a_a(i,1);
            delta_t = a_t_new(i,1) - a_t(i,1);

            if (abs(delta_a) > eps)
                a_a(i,1) = a_a_new(i,1);
            end
            if (abs(delta_t) > eps)
                a_t(i,1) = a_t_new(i,1);
            end

        end

% Calculating normal and tangential forces on the rotor blade.

        p_t(i+1,1) = Ct(i,1)*0.5*rho*c(i,1)*(V_0(i,1)*(1 -
a_a(i,1))/sin(phi(i,1)))^2;
        p_n(i+1,1) = Cn(i,1)*0.5*rho*c(i,1)*(V_0(i,1)*(1 -
a_a(i,1))/sin(phi(i,1)))^2;
        A_t(i,1) = (p_t(i+1,1) - p_t(i,1))/(n(i+1,1) - n(i,1));
        C_t(i,1) = (p_t(i,1)*n(i+1,1) - p_t(i+1,1)*n(i,1))/(n(i+1,1) - n(i,1));

        A_n(i,1) = (p_n(i+1,1) - p_n(i,1))/(n(i+1,1) - n(i,1));
        C_n(i,1) = (p_n(i,1)*n(i+1,1) - p_n(i+1,1)*n(i,1))/(n(i+1,1) - n(i,1));

        T(i,1) = 1/2*A_n(i,1)*(n(i+1,1)^2 - n(i,1)^2) + C_n(i,1)*(n(i+1,1) -
n(i,1));
        M(i,1) = 1/3*A_t(i,1)*(n(i+1,1)^3 - n(i,1)^3) +
1/2*C_t(i,1)*(n(i+1,1)^2 - n(i,1)^2);
        L(i,1) = 0.5*rho*c(i,1)*Cl(i,1)*(V_0(i,1)*(1 -
a_a(i,1))/sin(phi(i,1)))^2;

        M_sum(V_hub,1) = M_sum(V_hub,1) + M(i,1);
        T_sum(V_hub,1) = T_sum(V_hub,1) + T(i,1);
        L_sum(V_hub,1) = L_sum(V_hub,1) + L(i,1);

    end
    M_sum(V_hub,1) = M_sum(V_hub,1)*B;
    T_sum(V_hub,1) = T_sum(V_hub,1)*B;
    L_sum(V_hub,1) = L_sum(V_hub,1)*B;
    if M_sum(V_hub,1)*omega(V_hub,1) > power
        M_sum(V_hub,1) = power/omega(V_hub,1);
    end
        Rotor_power(V_hub,1) = M_sum(V_hub,1)*omega(V_hub,1);
End
```

REFERENCES

Agarwal P. *Structural reliability of offshore wind turbines*. Ph.D. thesis, The University of Texas at Austin, August 2008.

Betz, A., *Introduction to the Theory of Flow Machines*. (D. G. Randall, Trans.) Oxford: Pergamon Press, 1966.

Briggs, W. and V.E. Henson. *The DFT: An Owner's Manual for the Discrete Fourier Transform*. Philadelphia: SIAM, 1995.

Corrigan, J.J. and Schillings, J.J. *Empirical Model for Stall Delay due to Rotation*. American Helicopter Society Aeromechanics Specialists conf., San Francisco, CA, Jan. 1994.

Chaviaropoulos, P.K. (CRES) and Hansen, M.O.L. (Risø). *Investigating three-dimensional and rotational effects on wind turbine blades by means of a quasi-3D Navier-Stokes solver*. Journal of Fluids Engineering, Vol.22, No.2, pp.330-336, 2000.

Chung J., Hulbert G.M., *A time integration algorithm for structural dynamics with improved numerical dissipation: The generalized-alpha method*, J. Appl. Mech. 60, pp371-375, 1993.

Dean R.G., Dalrymple R.A. *Water Wave Mechanics for Engineers & Scientists* (Advanced Series on Ocean Engineering - Volume 2), World Scientific Publishing Co. Pte. Ltd., 2006.

Det Norske Veritas, *Rules for the Design, Construction and Inspection of Fixed Offshore Structures,* Appendix A and Appendix B, May 1978.

Eecen, P. J., *Wind Waves: Forces Due to Waves on Offshore Wind Turbines*, ECN-C--03-097, the Netherlands: Energy Research Centre of the Netherlands, September 2003.

Eicher J.A. *Stress and deformation of offshore piles under structural and wave loading*. Ocean Engineering 30, pp369–385, 2003.

Emrah K., Nadir Y. *Aerodynamic performance and analysis of HAWT blades*. Proceedings of the ASME 2009 Fluids Engineering Division Summer Meeting, August 2-6, Vail, Colorado, USA, 2009.

Eric Hau. *Wind Turbines: Fundamentals, Technologies, Application, Economics.* (2nd Edition), Springer, 2006

European Wind Energy Association (EWEA). *The Wind – Facts*. Annual report by EWEA, 2009

Fichaux N. and Wilkes J. *Oceans of Opportunity - Harnessing Europe's largest domestic energy resource,* Report by EWEA, September 2009

Glauert H. *Airplane propellers*, in W. F. Durand (ed) *Aerodynamic Theory*, vol 4,Division L, Julius Springer, Berlin, pp169–360, 1935

Gudmestad O.T. *Measured and predicted deep water wave kinematics in regular and irregular seas*. Marine Structures 6: pp1–73, 1993.

Hansen, M.O.L. *Aerodynamics of Wind Turbines* (2nd Edition). Earthscan 2008.

Jeffery L. Beacham, John R. Jensen, and Zhongwu Wang. *A Feasibility Analysis of South Carolina Wind Resources for Electric Power Generation*, 2006.

Jonkman, J. *Dynamics Modeling and Loads Analysis of an Offshore Floating Wind Turbine*. NREL/TP-500-41958. Golden, CO: National Renewable Energy Laboratory, November 2007.

Ionescu L., Pontius T. *Main shaft support for wind turbine with a fixed and floating bearing configuration*, Timken, 2009

Krogh Thomas. *HAWC Load Simulation of Generic 5MW Offshore Wind Turbine Model.* RisØ National Laboratory, Denmark Technical University, Roskilde. June 2004

Lindenburg C. *Modeling of rotational augmentation based on engineering considerations and measurements*. European Wind Energy Conference, London, 22-25 November, 2004

Morison, J. R.; O'Brien, M. P.; Johnson, J. W.; Schaaf, S. A., *The force exerted by surface waves on piles*, Petroleum Transactions (American Institute of Mining Engineers) 189: 149–154, 1950.

Myers John J. *Handbook of Ocean and Underwater Engineering*, McGRAW-Hill, 1969

Sathyajith Mathew. *Wind Energy: Fundamentals, Resource Analysis and Economics*, Spinger, 2006

Savenije F.J. Peeringa J.M. *Aero-elastic simulation of offshore wind turbines in the frequency domain*. ECN-E–09-060. Netherlands: Energy Research Centre of the Netherlands, 2009

Shim Sangyun. *Coupled dynamic analysis of floating offshore wind farms*. M.Sc. thesis, Texas A&M University, December 2007

Simms D., Schreck S., Hand M., Fingersh L.J. *NREL Unsteady Aerodynamics Experiment in the NASA-Ames Wind Tunnel: A Comparison of Predictions to Measurements*, NREL/TP-500-29494, June 2001

Stewart R.H. *Introduction to Physical Oceanography*. Texas A&M University, September 2008

U.S. Department of Energy, Office of Energy Efficiency and Renewable Energy, Wind & Water Power Program. *A National Offshore Wind Strategy.* 2011

Van der Tempel, J. *Design of support structures for offshore wind turbines*. Ph.D. thesis, Delft University of Technology, 2006

Wilson, R. E.; Lissaman, P.B. S.: *Applied Aerodynamics of Wind Power Machines*, Oregon State University, 1974